

DEVELOPMENT OF A ROTORCRAFT TIME DOMAIN SYSTEM
IDENTIFICATION SOFTWARE

A THESIS SUBMITTED TO
THE GRADUATE SCHOOL OF NATURAL AND APPLIED SCIENCES
OF
MIDDLE EAST TECHNICAL UNIVERSITY

BY

ONGUN HAZAR ASLANDOĞAN

IN PARTIAL FULFILLMENT OF THE REQUIREMENTS
FOR
THE DEGREE OF MASTER OF SCIENCE
IN
AEROSPACE ENGINEERING

JANUARY 2023

Approval of the thesis:

**DEVELOPMENT OF A ROTORCRAFT TIME DOMAIN SYSTEM
IDENTIFICATION SOFTWARE**

submitted by **ONGUN HAZAR ASLANDOĞAN** in partial fulfillment of the requirements for the degree of **Master of Science in Aerospace Engineering Department, Middle East Technical University** by,

Prof. Dr. Halil Kalıpçılar
Dean, Graduate School of Natural and Applied Sciences _____

Prof. Dr. Serkan Özgen
Head of Department, Aerospace Engineering _____

Assoc. Prof. Dr. İlkey Yavrucuk
Supervisor, Aerospace Engineering, METU _____

Dr. Gönenç Gürsoy
Co-supervisor, Aerotim Engineering LLC _____

Examining Committee Members:

Prof. Dr. Ozan Tekinalp
Aerospace Engineering, METU _____

Assoc. Prof. Dr. İlkey Yavrucuk
Aerospace Engineering, METU _____

Assoc. Prof. Dr. Halil Ersin Söken
Aerospace Engineering, METU _____

Assist. Prof. Dr. Ali Türker Kutay
Aerospace Engineering, METU _____

Assist. Prof. Dr. Yakup Özkazanç
Electrical and Electronics Engineering, Hacettepe University _____

Date: 03.01.2023

I hereby declare that all information in this document has been obtained and presented in accordance with academic rules and ethical conduct. I also declare that, as required by these rules and conduct, I have fully cited and referenced all material and results that are not original to this work.

Name, Surname: Ogun Hazar Aslandođan

Signature :

ABSTRACT

DEVELOPMENT OF A ROTORCRAFT TIME DOMAIN SYSTEM IDENTIFICATION SOFTWARE

Aslandođan, Ogun Hazar

M.S., Department of Aerospace Engineering

Supervisor: Assoc. Prof. Dr. İlkey Yavrucuk

Co-Supervisor: Dr. Gönenç Gürsoy

January 2023, 124 pages

A system identification software to identify stability and control derivatives for rotorcraft in hover and forward flight conditions is developed in this thesis. To demonstrate the identification procedure, a high fidelity nonlinear model of the H135 helicopter is used. Frequency sweep, 3211 and 2311 type inputs are given to the nonlinear helicopter model to generate test data. The procedure is carried out by identifying a state space model structure in time domain using output error method with Levenberg-Marquardt algorithm. Initially, a model reduction routine is carried out to drop redundant derivatives in the state space linear model structure. By making use of state and control delays, higher order dynamics introduced to model response are identified with greater accuracy. The identified system is verified in frequency domain using frequency sweep maneuvers, whose time domain signals are converted to frequency domain via discrete Fourier transform.

Keywords: system identification, rotorcraft system identification, time domain sys-

tem identification, output-error method, model reduction, frequency domain verification

ÖZ

DÖNER KANATLI HAVA ARAÇLARI İÇİN ZAMAN UZAYINDA SİSTEM TANIMLAMA YAZILIMI GELİŞTİRİLMESİ

Aslandođan, Ogun Hazar

Yüksek Lisans, Havacılık ve Uzay Mühendisliđi Bölümü

Tez Yöneticisi: Doç. Dr. İlkey Yavrucuk

Ortak Tez Yöneticisi: Dr. Gönenç Gürsoy

Ocak 2023 , 124 sayfa

Bu tezde döner kanatlı bi hava aracının havada asılı kalma ve ileri uçuş durumlarındaki kararlılık ve kontrol aerodinamik türevlerinin tanımlanması için sistem tanımlama yazılımı geliştirilmiştir. Bu sistem tanımlama işlemini göstermek için H135 helikopterinin yüksek sadakat seviyesine sahip doğrusal olmayan bir modeli kullanılmıştır. Bu doğrusal olmayan helikopter modeline frekans taraması, 3211 ve 2311 tipi girdiler verilerek test verileri oluşturulmuştur. Bu prosedürde zaman uzayında çıktı hatası metodu ile Levenberg-Marquardt algoritması ile durum uzayı yapısında bir model tanımlanmıştır. Başlandıçta bu model yapısındaki ihtiyaç fazlası türevleri eksiltmek için bir model küçültme rutini uygulanmıştır. Model cevabındaki yüksek mertebe dinamiklerin daha yüksek doğrulukta tanımlanabilmesi için durum ve kontrollerde zaman gecikmeleri kullanılmıştır. Tanımlanan sistem, frekans taraması manevralarının ayrık Fourier dönüşümü ile frekans uzayından zaman uzayına dönüştürülmesi ile frekans uzayında doğrulanmıştır.

Anahtar Kelimeler: sistem tanımlama, döner kanatlı hava aracı sistem tanımlaması, zaman uzayında sistem tanımlaması, çıktı hatası metodu, model küçültme, frekans uzayında doğrulama

To people who find joy in engineering

ACKNOWLEDGMENTS

I would like to express my greatest gratitude to my supervisor Assoc. Prof. Dr. İlkey Yavrucuk for his guidance throughout my education in METU and career afterwards. He was the one who inspired me to study the subject of flight mechanics, and I am grateful that he introduced me to this incredibly exciting discipline, system identification. I would also like to acknowledge my co-supervisor, Dr. Gönenç Gürsoy. Having the opportunity to work with him was a pleasure that I feel grateful for. I am thankful for his guidance, time and belief in me. The things he taught me about problem solving and analytical thinking is what I treasure the most. My supervisors are such inspirations for me, and I feel so lucky that I had the chance to work with both of them.

I would also like to thank my thesis committee for their precious comments and feedbacks, which improved the quality of this work.

I would like to express my love and gratitude to my family for always believing in me, doubtlessly supporting my goals and dreams in life. They inspired me to study engineering and I am thankful that they created every opportunity for me.

I feel so lucky to have dear Ceyda Kavak by my side. Her endless support and belief in me always give me courage to move on. Also, I would like to thank her for always being there whenever I am in need.

I am grateful to be a part of Aerotim Engineering during this journey. I had unforgettable experiences by working with such talented and successful people. I am thankful for all the opportunities and resources they provided to me during my time there.

Lastly, I would like to thank TUBITAK 2211 National Graduate Scholarship Program for funding my master's degree studies.

TABLE OF CONTENTS

ABSTRACT	v
ÖZ	vii
ACKNOWLEDGMENTS	x
TABLE OF CONTENTS	xi
LIST OF TABLES	xiv
LIST OF FIGURES	xv
LIST OF ABBREVIATIONS	xxii
CHAPTERS	
1 INTRODUCTION	1
1.1 Background and Objectives	1
1.2 Literature Review	4
1.3 Outline of the Thesis	5
2 THEORY AND PROCEDURE	7
2.1 Input Design for Time Domain Identification	7
2.2 Mathematical Model	13
2.2.1 Modelling of Additional Dynamics	19
2.3 Output-Error Method	21
2.3.1 Maximum Likelihood Estimation Principle	22

2.3.2	Implementation of Maximum Likelihood Parameter Estimation on Mathematical Models	25
2.3.3	Gauss-Newton Algorithm	26
2.3.4	Levenberg-Marquardt Algorithm	30
2.4	Model Structure Determination	32
2.5	Validation of the Identified System	37
2.5.1	Transformation of Time Domain Signals to Frequency Domain	39
2.5.2	Windowing	42
2.5.3	Coherence Function	47
2.5.4	Validation Criteria	48
3	IMPLEMENTATION AND RESULTS	51
3.1	Identification with Hessian Based Model Reduction	52
3.1.1	Identification of Dynamics in Hover	54
3.1.1.1	Results for Longitudinal Cyclic Input	56
3.1.1.2	Results for Lateral Cyclic Input	63
3.1.1.3	Results for Collective Input	66
3.1.1.4	Results for Pedal Input	68
3.1.2	Identification of Dynamics in Forward Flight	70
3.1.2.1	Results for Longitudinal Cyclic Input	73
3.1.2.2	Results for Lateral Cyclic Input	76
3.1.2.3	Results for Collective Input	79
3.1.2.4	Results for Pedal Input	81
3.2	Results with an Initial Model Structure from Adaptive Learning	83

3.2.1	Identification of Dynamics in Hover	87
3.2.2	Identification of Dynamics in Forward Flight	93
4	CONCLUSIONS AND FUTURE STUDIES	99
4.1	Conclusions	99
4.2	Future Studies	100
	REFERENCES	101
A	ADDITIONAL IDENTIFICATION RESULTS	107
A.1	Additional Results in Hover	107
A.1.1	Results for Longitudinal Cyclic Input	107
A.1.2	Results for Lateral Cyclic Input	108
A.1.3	Results for Collective Input	109
A.1.4	Results for Pedal Input	110
A.2	Additional Results in Forward Flight	111
A.2.1	Results for Longitudinal Cyclic Input	111
A.2.2	Results for Lateral Cyclic Input	112
A.2.3	Results for Collective Input	113
A.2.4	Results for Pedal Input	114
B	PARAMETERS REMOVED FROM THE MODEL STRUCTURE	117
B.1	Removed Parameters in Hover	117
B.2	Removed Parameters in Forward Flight	119
C	IDENTIFIED PARAMETERS	121
C.1	Identified Parameters in Hover	121
C.2	Identified Parameters in Forward Flight	123

LIST OF TABLES

TABLES

Table 3.1	List of maneuvers at each trim condition	53
Table 3.2	Trimmed state values at hover	54
Table 3.3	Trimmed state values at 70 knots forward flight	70
Table B.1	List of parameters removed from the model structure in hover	117
Table B.1	List of parameters removed from the model structure in hover (Continued)	118
Table B.2	List of parameters removed from the model structure in forward flight	119
Table C.1	List of parameters identified in hover	121
Table C.1	List of parameters identified in hover (Continued)	122
Table C.2	List of parameters identified in forward flight	123
Table C.2	List of parameters identified in forward flight (Continued)	124

LIST OF FIGURES

FIGURES

Figure 2.1	Frequency domain comparison of different input types [18]	9
Figure 2.2	Feedback controller for longitudinal channel	11
Figure 2.3	Feedback controller for lateral channel	11
Figure 2.4	Feedback controller for heave channel	12
Figure 2.5	Feedback controller for yaw channel	12
Figure 2.6	3211 type input given to longitudinal cyclic channel of truth model and its response in hover	13
Figure 2.7	Body fixed reference frame (adapted from [42])	14
Figure 2.8	Frequency sweep type input given to longitudinal cyclic channel of truth model and its response in forward flight	40
Figure 2.9	Boxcar (rectangular) window in time domain [4]	43
Figure 2.10	Boxcar (rectangular) window in frequency domain [4]	44
Figure 2.11	Hanning window in time domain [4]	44
Figure 2.12	Hanning window in frequency domain [4]	45
Figure 2.13	Boundaries of maximum unnoticeable added dynamics (MUAD) [16] and allowable error envelopes (AEE) [27]	49
Figure 3.1	Variation of RMSE through model reduction in hover	55

Figure 3.2	Iteration history of parameters for identification in hover	56
Figure 3.3	Time domain identification results for longitudinal cyclic 2311 input in positive direction during hover	57
Figure 3.4	Bode plots of q/δ_{long} and p/δ_{long} pairs for frequency sweep in longitudinal cyclic in hover	58
Figure 3.5	Coherence and Errors of q/δ_{long} and p/δ_{long} pairs for frequency sweep in longitudinal cyclic in hover	58
Figure 3.6	Iteration history of parameters for identification in hover with additional dynamics	60
Figure 3.7	Time domain identification results for longitudinal cyclic 2311 input in positive direction during hover	61
Figure 3.8	Time domain identification results for longitudinal cyclic 3211 input in positive direction during hover	61
Figure 3.9	Frequency domain comparison of q/δ_{long} and p/δ_{long} input out- put pairs in longitudinal cyclic frequency sweep maneuver in hover . . .	62
Figure 3.10	q/δ_{long} and p/δ_{long} input output pairs and error bounds in longi- tudinal cyclic frequency sweep maneuver in hover	62
Figure 3.11	Lateral cyclic 2311 input in positive direction during hover . . .	63
Figure 3.12	Lateral cyclic 3211 input in positive direction during hover . . .	64
Figure 3.13	Frequency domain comparison of q/δ_{lat} and p/δ_{lat} input output pairs in lateral cyclic frequency sweep maneuver in hover	64
Figure 3.14	q/δ_{lat} and p/δ_{lat} input output pairs and error bounds in lateral cyclic frequency sweep maneuver in hover	65
Figure 3.15	Collective 2311 input in positive direction during hover	66
Figure 3.16	Collective 3211 input in positive direction during hover	66

Figure 3.17	Frequency domain comparison of r/δ_{coll} and a_z/δ_{coll} input output pairs in collective frequency sweep maneuver in hover	67
Figure 3.18	r/δ_{lat} and a_z/δ_{lat} input output pairs and error bounds in collective frequency sweep maneuver in hover	67
Figure 3.19	Pedal 2311 input in positive direction during hover	68
Figure 3.20	Pedal 3211 input in positive direction during hover	68
Figure 3.21	Frequency domain comparison of r/δ_{coll} and a_y/δ_{coll} input output pairs in pedal frequency sweep maneuver in hover	69
Figure 3.22	r/δ_{lat} and a_y/δ_{lat} input output pairs and error bounds in pedal frequency sweep maneuver in hover	69
Figure 3.23	Variation of RMSE through model reduction in 70 knots forward flight	71
Figure 3.24	Iteration history of parameters for identification in 70 knots forward flight	72
Figure 3.25	Iteration history of parameters for identification in 70 knots forward flight with additional dynamics	73
Figure 3.26	Longitudinal cyclic 2311 input in positive direction during 70 knots forward flight	74
Figure 3.27	Longitudinal cyclic 3211 input in positive direction during 70 knots forward flight	74
Figure 3.28	Bode plots of q/δ_{long} and p/δ_{long} pairs for frequency sweep in longitudinal cyclic in 70 knots forward flight	75
Figure 3.29	Coherence and Errors of q/δ_{long} and p/δ_{long} pairs for frequency sweep in longitudinal cyclic in 70 knots forward flight	76
Figure 3.30	Lateral cyclic 2311 input in positive direction during 70 knots forward flight	77

Figure 3.31	Lateral cyclic 3211 input in positive direction during 70 knots forward flight	77
Figure 3.32	Frequency domain comparison of q/δ_{lat} and p/δ_{lat} input output pairs in lateral cyclic frequency sweep maneuver 70 knots in forward flight	78
Figure 3.33	q/δ_{lat} and p/δ_{lat} input output pairs and error bounds in lateral cyclic frequency sweep maneuver in 70 knots forward flight	78
Figure 3.34	Collective 2311 input in positive direction during 70 knots forward flight	79
Figure 3.35	Collective 3211 input in positive direction during 70 knots forward flight	79
Figure 3.36	Frequency domain comparison of r/δ_{coll} and a_z/δ_{coll} input output pairs in collective frequency sweep maneuver in 70 knots forward flight	80
Figure 3.37	r/δ_{lat} and a_z/δ_{lat} input output pairs and error bounds in collective frequency sweep maneuver in 70 knots forward flight	80
Figure 3.38	Pedal 2311 input in positive direction during 70 knots forward flight	81
Figure 3.39	Pedal 3211 input in positive direction during 70 knots forward flight	81
Figure 3.40	Frequency domain comparison of r/δ_{coll} and a_y/δ_{coll} input output pairs in pedal frequency sweep maneuver in 70 knots forward flight	82
Figure 3.41	r/δ_{lat} and a_y/δ_{lat} input output pairs and error bounds in pedal frequency sweep maneuver in 70 knots forward flight	82
Figure 3.42	Example parameter convergence with adaptive learning (adapted from [13])	84
Figure 3.43	Example parameter reduction with adaptive learning [13]	85

Figure 3.44	Iteration histories in hover [13]	86
Figure 3.45	Time domain results of adaptive learning and maximum likelihood refinement in hover	87
Figure 3.46	Frequency domain comparison of adaptive learning and maximum likelihood refinement with truth model in longitudinal cyclic maneuver in hover	88
Figure 3.47	Coherence and errors of adaptive learning and maximum likelihood refinement with truth model in longitudinal cyclic maneuver in hover	89
Figure 3.48	Frequency domain comparison of adaptive learning and maximum likelihood refinement with truth model in lateral cyclic maneuver in hover	89
Figure 3.49	Coherence and errors of adaptive learning and maximum likelihood refinement with truth model in lateral cyclic maneuver in hover	90
Figure 3.50	Frequency domain comparison of adaptive learning and maximum likelihood refinement with truth model in collective maneuver in hover	90
Figure 3.51	Coherence and errors of adaptive learning and maximum likelihood refinement with truth model in collective maneuver in hover	91
Figure 3.52	Frequency domain comparison of adaptive learning and maximum likelihood refinement with truth model in pedal maneuver in hover	91
Figure 3.53	Coherence and errors of adaptive learning and maximum likelihood refinement with truth model in pedal maneuver in hover	92
Figure 3.54	Time domain results of adaptive learning and maximum likelihood refinement in 70 knots forward flight	93

Figure 3.55	Frequency domain comparison of adaptive learning and maximum likelihood refinement with truth model in longitudinal cyclic maneuver in 70 knots forward flight	94
Figure 3.56	Coherence and errors of adaptive learning and maximum likelihood refinement with truth model in longitudinal cyclic maneuver in 70 knots forward flight	94
Figure 3.57	Frequency domain comparison of adaptive learning and maximum likelihood refinement with truth model in lateral cyclic maneuver in 70 knots forward flight	95
Figure 3.58	Coherence and errors of adaptive learning and maximum likelihood refinement with truth model in lateral cyclic maneuver in 70 knots forward flight	95
Figure 3.59	Frequency domain comparison of adaptive learning and maximum likelihood refinement with truth model in collective maneuver in 70 knots forward flight	96
Figure 3.60	Coherence and errors of adaptive learning and maximum likelihood refinement with truth model in collective maneuver in 70 knots forward flight	96
Figure 3.61	Frequency domain comparison of adaptive learning and maximum likelihood refinement with truth model in pedal maneuver in 70 knots forward flight	97
Figure 3.62	Coherence and errors of adaptive learning and maximum likelihood refinement with truth model in pedal maneuver in 70 knots forward flight	97
Figure A.1	Longitudinal cyclic 2311 input in negative direction during hover	107
Figure A.2	Longitudinal cyclic 3211 input in negative direction during hover	108
Figure A.3	Lateral cyclic 2311 input in negative direction during hover . . .	108

Figure A.4	Lateral cyclic 3211 input in negative direction during hover	109
Figure A.5	Collective 2311 input in negative direction during hover	109
Figure A.6	Collective 3211 input in negative direction during hover	110
Figure A.7	Pedal 2311 input in negative direction during hover	110
Figure A.8	Pedal 3211 input in negative direction during hover	111
Figure A.9	Longitudinal cyclic 2311 input in negative direction during 70 knots forward flight	111
Figure A.10	Longitudinal cyclic 3211 input in negative direction during 70 knots forward flight	112
Figure A.11	Lateral cyclic 2311 input in negative direction during 70 knots forward flight	112
Figure A.12	Lateral cyclic 3211 input in negative direction during 70 knots forward flight	113
Figure A.13	Collective 2311 input in negative direction during 70 knots for- ward flight	113
Figure A.14	Collective 3211 input in negative direction during 70 knots for- ward flight	114
Figure A.15	Pedal 2311 input in negative direction during 70 knots forward flight	114
Figure A.16	Pedal 3211 input in negative direction during 70 knots forward flight	115

LIST OF ABBREVIATIONS

AEE	Allowable Error Envelope
AFCS	Automatic Flight Control System
CG	Center of Gravity
CIFER	Comprehensive Identification from Frequency Responses
DFT	Discrete Fourier Transform
DoF	Degree of Freedom
EASA	European Union Aviation Safety Agency
MIMO	Multi Input Multi Output
ML	Maximum Likelihood
MUAD	Maximum Unnoticeable Added Dynamics
RMSE	Root Mean Square Error
SIDPAC	System Identification Programs for Aircraft
A, B, C, D	state space representation matrices
u, v, w	translational velocities in body fixed frame
a_x, a_y, a_z	specific accelerations in body fixed frame
p, q, r	angular rates in body fixed frame
θ	pitch angle
ϕ	roll angle
ψ	yaw angle
X, Y, Z	force components along body fixed frame
L, M, N	moments along body fixed frame
δ_{long}	longitudinal cyclic control
δ_{lat}	lateral cyclic control
δ_{coll}	collective control

δ_{ped}	pedal control
g	gravitational acceleration
\mathbf{x}	state vector
\mathbf{u}	control input vector
\mathbf{y}	output vector
\mathbf{z}	measurement vector
\mathbf{v}	measurement error vector
Θ	unknown parameter vector
n_y	number of observation variables
t	time
Δt	time step
τ	time delay
σ	standard deviation
m	mean value
$E\{\}$	expectation operator
ξ	Gaussian white noise
f	accelerometer measurement vector
ω	gyroscope measurement vector
R	measurement noise covariance matrix
N	number of samples
J	maximum likelihood cost function
\mathcal{F}	Hessian matrix
\mathcal{G}	gradient vector
λ	Levenberg-Marquardt parameter
I	identity matrix
ν	reduction factor
CR_i	Cramer-Rao bound of the i th parameter

$\overline{\text{CR}}_i$	normalized Cramer-Rao bound of the i th parameter
I_i	insensitivity of the i th parameter
\bar{I}_i	normalized insensitivity of the i th parameter
f	frequency
$X(f)$	input Fourier coefficient
$Y(f)$	output Fourier coefficient
$H(f)$	frequency response function
j	imaginary number, $\sqrt{-1}$
a_n	time based signal
\tilde{G}_{xx}	input autospectral density function
\tilde{G}_{yy}	output autospectral density function
\tilde{G}_{xy}	cross spectral density function
u_b	Boxcar window function
u_h	Hanning window function
n_d	number of windows
T_w	window length
$\hat{\gamma}_{xy}^2$	coherence function between input and output
ε	frequency domain error function

CHAPTER 1

INTRODUCTION

1.1 Background and Objectives

Mathematical models are constructed by employing the laws and concepts of mathematics and aim to express real life processes. These models are used in numerous fields of studies whether it is natural sciences, engineering or social sciences. In the field of aerospace engineering, mathematical models are often used to describe physical processes taking place in real life. The models of flight vehicle dynamic systems aim to reflect the actual behavior of those systems with certain degrees of accuracy. They relate pilot inputs to dynamic vehicle response using theoretical formulations. Accurate modelling of the actual system is challenging, as all influences on the flight of an aircraft and their underlying physics are not straightforward. One approach to construct mathematical models for a system with available input and output data is system identification. System identification is a field of study which focuses on extracting the information that is present in the available experimental data by solving an inverse problem. Even though system identification has numerous areas of utilization, this work focuses on aerospace applications and specifically rotorcraft system identification.

The problem of system identification is to determine a mathematical model that produces the best matching responses to the measurements when the same test inputs are provided. The mathematical model structure for state space systems is not unique, therefore a prior knowledge or a systematic approach to determine the necessary system parameters is necessary. System identification is an essential step in aircraft design as its products can be used to verify wind tunnel data or analytical calculations,

examine system performance and handling qualities, develop flight stability augmentation systems and build mathematical models for in-flight simulators [18]. Moreover, system identification can provide insight to actual processes taking place, leading to more accurate physics based modelling.

The system identification procedure to build mathematical models from experimental data can be carried out in either frequency domain or time domain. The choice of domain may depend on the application and the system to be identified, as practices in both domains have their advantages. Frequency domain methods provide direct insight to aircraft stability characteristics and are better in dealing with noisy data. The methods aim to reduce the frequency response errors between (errors of magnitude and phase content) the measured signals and the mathematical model. Algorithms are usually more efficient since low number of data points are present and no integration of the system equations is required. For flight vehicle identification, frequency sweep type maneuvers are well suited for these methods. On the other hand, time domain methods aim to reduce the errors between time domain signals of measurements and estimated responses. Usually, 3211 type multistep inputs with shorter durations are utilized in time domain identification. These methods are more intuitive to work with, and physical systems are more closely resembled by state space models in time domain. Furthermore, a state space model is often the desired final product of system identification. For these reasons, time domain system identification is studied in this work.

There are numerous applications of time domain and frequency domain methods on fixed wing or rotary wing aircraft. The problem of fixed wing aircraft identification is more straightforward, as the whole aircraft can be considered as a single rigid body. Furthermore, due to planar symmetry, most fixed wing aircraft exhibit uncoupled dynamics between longitudinal and lateral axes. This is not the case for most rotorcraft, especially for single rotor helicopters. Helicopters are versatile air vehicles that can be used to execute numerous tasks owing to their ability to hover. However, due to the presence of rotor, the aircraft cannot be considered as a rigid body. For an accurate helicopter model, the rotor dynamics and the rotor-fuselage interactions are usually needed to be modelled, but modelling of such dynamics is not straightforward. They exhibit MIMO flight characteristics which vary considerably with the

flight condition. Furthermore, due to their unstable and highly nonlinear nature, the identification of helicopter dynamics is challenging, and the data collected is prone to be corrupted by noise due to mechanical vibrations. Therefore, the identification of rotorcraft dynamics is usually more challenging than fixed wing identification.

The usual workflow of a system identification procedure is as follows. First, the aim and scope of identification is determined. The optimal inputs to excite the aircraft are designed, and flight tests are executed. With the collected data, compatibility checks are performed, and data post-processing is done as required. The mathematical model structure is determined and constructed with the available information regarding the system. The collected data are then inserted to the estimation algorithm to identify a mathematical model that produces the best fitting responses. Finally, the obtained mathematical model is verified to assess model fidelity. The preferred practice is to verify the system in frequency domain, if the identification is carried out in time domain, and vice versa.

The objective of this work is to establish a time domain system identification software and use it to identify the dynamics of a full scale helicopter. It is aimed to develop a software that encompasses powerful identification methods in time domain to identify rotorcraft with additional dynamics. For this purpose, the output error algorithm, which is widely known in the field, is used as the primary optimization method. One of the drawbacks of time domain methods is intermediate divergence, which is especially true for output error method. Owing to the nonlinear behavior of rotorcraft around hover, simulations in time domain identification can encounter divergence. To remedy this issue, time domain output error method is coupled with the Levenberg-Marquardt algorithm. This algorithm not only prevents intermediate divergence to a great extent, it also alters the iteration step size towards steepest descent of the cost function. Utilizing the capability of time domain methods to identify linear or nonlinear systems, the option to enable state and control delays on desired parameters is implemented. With these delays, the aim is to account for the higher order dynamics in the system due to rotor. The acquired models are then verified in frequency domain, using dissimilar inputs.

1.2 Literature Review

This section discusses the historical summary of research in system identification and the evolution of the methods used. References [18], [44] and [28] present summaries regarding their discipline of system identification and a more comprehensive investigation covering the advancements in both time and frequency domains can be found in [15]. The early examples of flight vehicle system identification relied on the experimental analysis of the stability derivatives in the 1920s. The interest in determination of aircraft derivatives from flight test data continued rising since then. In the 1940s and 1950s, a number of other estimation approaches are proposed. Milliken [26] used steady state oscillatory excitations to identify aircraft dynamics with frequency response data, and Seamans et al. [34] introduced the pulse method for aircraft performance evaluation. Another important milestone is the usage of response curve fitting method by Shinbrot [40]. This method is equivalent to the output error algorithm, that is practiced in this work [18]. Even though the concept of response curve fitting is implemented to flight vehicle system identification as early as 1950s, the approach is abandoned at the time due to inadequacy of processing power. Therefore, the identification means during the 1940s and 1960s evolved around frequency domain methods. In 1960, analog matching technique became popular to verify or correct wind tunnel data. The procedure requires manual tuning of the aircraft derivatives, hence a few parameters can be adjusted simultaneously and the process time-consuming.

With the technological advancements allowing more powerful processors to be built, the focus is shifted from frequency domain methods to time domain methods. In 1965, Åström and Bohlin carried out time domain identification with maximum likelihood parameter estimation [3]. Following that, several other contributions are made regarding implementations of various algorithms in the 1970s. A modified Newton-Raphson optimization technique is proposed by Iliff and Taylor [17] and a Kalman Filter representation is used with maximum likelihood estimation principle to identify linear systems by Mehra [25].

One of the early examples of rotorcraft system identification is presented by Kaufman and Peress [19] where longitudinal dynamics of S-55 helicopter is identified by matching frequency responses. Marchand and Fu [23] developed maximum likeli-

hood parameter estimation in frequency domain to identify Bo-105 helicopter. The transfer function models of XV-15 tilt-rotor aircraft and Bell214-ST helicopter are identified using frequency responses and frequency sweep maneuvers by Tischler [43, 46]. An overview of rotorcraft identification research is presented by Padfield in [32]. Seher-Weiss carried out identification of H135 helicopter with additional rotor and engine dynamics in frequency domain [35, 37, 38]. The time domain system identification methods are applied to small scale unmanned rotorcraft by Li [21], Shim et al. [39] and Khaligh et al. [20]. Grauer et al. [12] performed system identification in both time and frequency domains, employing equation error and output error methods for a small scale hobby helicopter.

The discipline of system identification is studied by many organizations, and numerous contributions have been made over past decades. The contributions include system identification software products such as CIPHER [44] SIDPAC [28] and FITLAB [36], which are being used for commercial projects or for research purposes.

1.3 Outline of the Thesis

In Chapter 1, a general background for the discipline of system identification is presented. The purpose of system identification is provided with a brief history and the objective of this thesis. Chapter 2 deals with the mathematical backgrounds of the algorithms used for the development of the system identification software. It starts with the discussion of appropriate input designs to generate the test data to be employed in system identification. Then, the mathematical model structure adopted in this work to represent the dynamics of the actual system is examined, along with a discussion on modelling higher order dynamics. The maximum likelihood parameter estimation principle and the implementation of Levenberg-Marquardt algorithm to the output error optimization method are presented. A systematic model structure determination routine is discussed to eliminate unnecessary parameters from the model structure. Finally, the procedure to verify the identified system in frequency domain is examined. Discrete Fourier transformation to transform time domain signals to frequency domain is presented, as well as the windowing approach to achieve greater accuracy during this transformation. Chapter 3 deals with the implementation of the mathe-

mathematical theory discussed in the previous chapter and the results obtained. The whole procedure followed during the implementation of the algorithms and the approaches to solve the problems confronted are explained. In this chapter, results obtained from two different implementations of this system identification software are presented. In the first case, no prior knowledge of the model structure and the initial parameter values are known, hence model reduction and system identification are carried out with the algorithms covered in Chapter 2. The second case examines the application of the maximum likelihood identification method to a model, whose structure is determined via adaptive learning algorithm along with the initial values of the parameters. Chapter 4 concludes the studies with a summary of the work done and presents possible fields of research to extend this study.

CHAPTER 2

THEORY AND PROCEDURE

This study focuses on development of a system identification software for rotorcraft dynamics using output error algorithm. However, the nonlinear nature of rotorcraft dynamics due to the presence of rotor creates a challenging identification problem. The flight test campaign to generate the data set suitable for identification must be handled with care. Since the identification is carried out in time domain, where simulation of a mathematical model is required for identification, utilization of an optimization algorithm prone to convergence is required to avoid intermediate divergence. The higher order dynamics due to rotor also have to be accounted for to achieve an accurate model. Finally, the identified models must be validated to prove suitability for applications like controller design or flight simulator development. This chapter discusses theories behind each step of system identification. Appropriate input design for identification purposes is discussed, mathematical model structures for flight vehicle identification are examined along with an approach to account for additional dynamics. The mathematical background of the output error optimization loop coupled with Levenberg-Marquardt algorithm are examined and a systematic approach to model structure determination is presented. Finally, the validation of the identified system in frequency domain is discussed, along with methods to accurately convert time domain signals to frequency domain.

2.1 Input Design for Time Domain Identification

The first step of the procedure followed in this work is the collection of the test data suitable for system identification. In system identification applications for a real life

aircraft, data gathering is performed by carrying out flight tests and recording the inputs given to the system and the responses of the system. The aim is to excite modes of the aircraft independently with adequate intensity. It is a crucial step as the accuracy of parameter estimation relies on the information present in the test data. If the dynamic characteristics of the system are not reflected in the data, then those characteristics cannot be identified. Therefore, the maneuvers executed in flight tests must be tailored such that the aircraft is excited to show its distinct responses. Generally, the excitement of dynamic modes of an aircraft is done through pulse, step, multistep or harmonic type inputs [18].

In figure 2.1, the energy spectrum of step, doublet and 3211 type inputs are presented. The plot shows the frequency bandwidths of the excitations that the inputs generate. It is important that the natural frequency of the mode aimed to be excited to lie within the bandwidth of the excitement. As can be seen from the figure, step, and doublet type inputs excite the system in a narrower frequency range compared to 3211 type inputs. Therefore, 3211 type inputs are chosen to be adequate for system identification of rotorcraft dynamics in time domain. Owing to its simplicity and easy applicability, this type of inputs are widely used in time domain system identification of air vehicles. These inputs are executed starting from a trimmed state of aircraft. Trim condition of an aircraft is a state of equilibrium where the velocity is fixed and no rotation around pitch and roll axes are present [41]. Having three time steps of initial step input may cause the aircraft to deviate far from its trim condition. Therefore, to prevent any divergence from initial trim condition, 2311 type inputs are also experimented to be used in the test campaign along with 3211 type inputs. As a result, it is decided that both 3211 and 2311 maneuvers are sufficient and both are included in the campaign to provide more tests to the estimation algorithm.

It should be noted that frequency sweep type inputs has a wider bandwidth compared to multistep inputs such as doublet or 3211. A frequency sweep is executed such that the input is given as a harmonic motion, starting with a lower frequency and gradually increasing it to cover a wide frequency range. With rewards of broader bandwidth and eliminating the need to execute test maneuvers in both directions, frequency sweep tests are usually longer than the discussed multistep input tests. Even though this type of input seems advantageous, 3211 and 2311 type input are better suited for

time domain identification. This is due to the fact that the estimation algorithm is prone to divergence with such lengthy maneuvers, which will be further discussed in Section 2.3. Nevertheless, frequency sweep type inputs are used for verification of the identified model in frequency domain, as explained in Section 2.5.

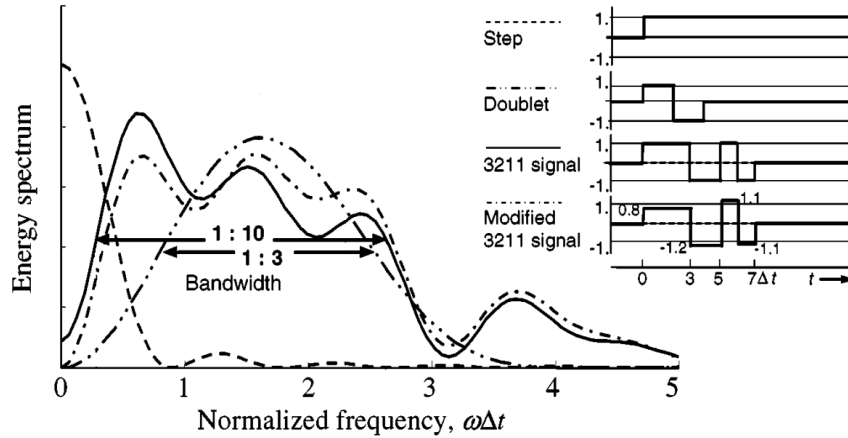


Figure 2.1: Frequency domain comparison of different input types [18]

A physics based high fidelity model of Airbus Helicopters H135 helicopter is used as the truth model to generate the simulated flight test data, which is also referred as the truth model data. It is a light utility helicopter with a twin engine configuration. The helicopter has a four bladed bearingless fiber composite main rotor and the Fenestron shrouded tail rotor [2]. It can carry five to six passengers, can achieve 136 knots of speed and 342 nautical miles of range and has a maximum take-off weight of 2980 kg. The helicopter model is developed in MATLAB Simulink environment and utilizes Aerotim Engineering's [1] core model components that are developed for level D flight models certified by European Union Aviation Safety Agency (EASA). The main rotor model has 10 virtual and 4 actual blades with Pitt-Peters dynamic inflow model and 2-D lookup tables of C_L , C_D and C_M for blade elements. Also, second order flapping, dynamic wake distortion, ground effect and vortex ring state models are present in the model. The maneuvers are simulated with AFCS turned off.

In system identification projects, the scope of a flight test campaign depends on the goal of identification. This study aims to implement the developed software to identify the dynamics of the H135 full scale helicopter model in two flight conditions, namely hover and forward flight with 70 knots speed. Therefore, it is of interest to

excite the characteristic of the truth model with all input channels separately, which are longitudinal cyclic, lateral cyclic, collective and pedal. Using 3211 and 2311 type inputs in both directions and for all four control channels, 16 maneuvers are executed for one trim condition.

A trial and error process is handled with care to generate adequate truth model data. First, the truth model is trimmed to one of the desired trim conditions, which are hover and 70 knots forward flight. Then from the trimmed state of the model 3211 and 2311 inputs are given to each input channel in both directions, where each time step of a 3211 or 2311 type input is considered to be one second. Note that each input is given separately, while the model is at trimmed condition. After each input signal is given, it is checked whether the parameters related to the on axis response of the input channel is excited sufficiently or not. Pitch rate in longitudinal cyclic tests, roll rate in lateral cyclic tests, vertical acceleration in collective tests and yaw rate and lateral acceleration in pedal tests are monitored throughout the simulation process. Input magnitude is adjusted to ensure that the excitations of the on axis parameters are adequate. If necessary, the magnitudes of each step of 3211 signal can be altered, as shown in figure 2.1 as the modified 3211 signal. While simulating test maneuvers, a closed loop low frequency controller is used in all four controls to prevent the helicopter from deviating from the linear region around the initial trim condition. The controller gains are also adjusted such that the lower frequency controls in the other axes are not aggressive.

Figures 2.2, 2.3, 2.4 and 2.5 show the feedback controllers used to keep the helicopter in the linear region around the trim condition. The controllers for the longitudinal and lateral channels are similar, as they both use ground speed references. For heave channel, vertical speed is held with a simple proportional feedback controller and lastly, heading feedback is used for pedal controls.

Figure 2.6 shows that the 3211 type input given to the longitudinal cyclic channel of the truth model and its response. The control inputs are shown as the delta values from the trim condition, and the unmodified multistep input is also provided as the raw input. It can be seen that the feedback controller modifies the multistep input given to the system and make low frequency adjustments in other controls to keep the

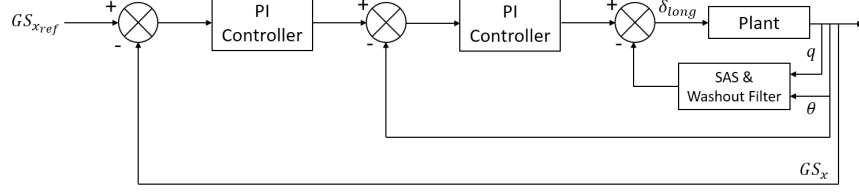


Figure 2.2: Feedback controller for longitudinal channel

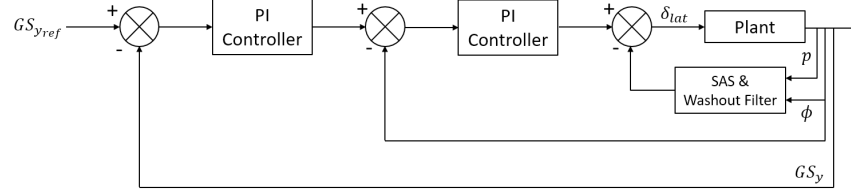


Figure 2.3: Feedback controller for lateral channel

system around hover.

Time histories of Euler angles, accelerations and angular rates are recorded for each maneuver during simulations with a sampling rate of 60 Hz. During simulations, Gaussian white noise is added to the control signals which are fed into the plant to represent process noise. Computer generated noises are associated with seed numbers, where every seed indicates a different noise signal. In all control channels, noise signals with different seed numbers are added, meaning that the noise contents in each signal are not the same. For process noise ξ_p , the variance of the noise is decided to be $\sigma_p^2 = \text{Var}(\xi_p) = 0.15$. Even though process noise is implemented during simulations, it is assumed that the inputs to the system can be measured accurately, therefore noise free input signals are recorded to be used in identification.

Along with process noise, Gaussian white noise is added to state measurements to mimic measurement noise in accelerometer and gyroscope readings in real flight tests. Similarly, noise signals with different seed numbers are added to model outputs. For accelerometer measurements, the variance of noise is selected to be $\sigma_a^2 = \text{Var}(\xi_a) = 0.04$ and for gyroscope, the variance of noise is $\sigma_g^2 = \text{Var}(\xi_g) = 0.15$. The accelerometer measurements are modelled as $\tilde{f} = f + \xi_a$ and the gyroscope measurements are modelled as $\tilde{\omega} = \omega + \xi_g$ where f and ω are model outputs and $\tilde{\cdot}$ is used to denote

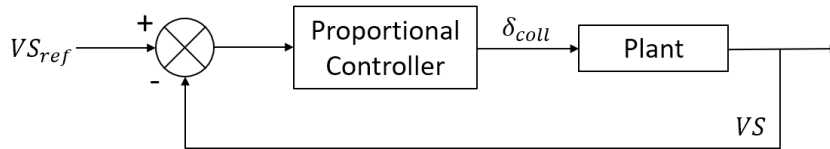


Figure 2.4: Feedback controller for heave channel

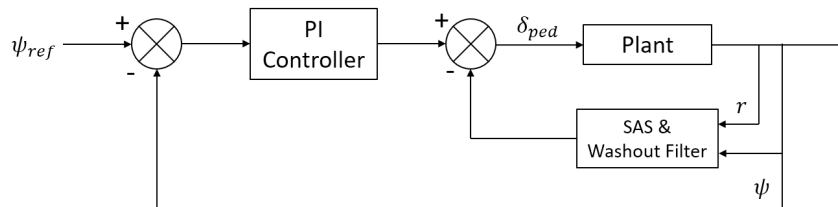


Figure 2.5: Feedback controller for yaw channel

measurements. As the data set to be identified is generated through simulations, the need to remedy biases and drifts in data stemming from weather conditions and instrumentation is eliminated, which are usually required in real flight applications.

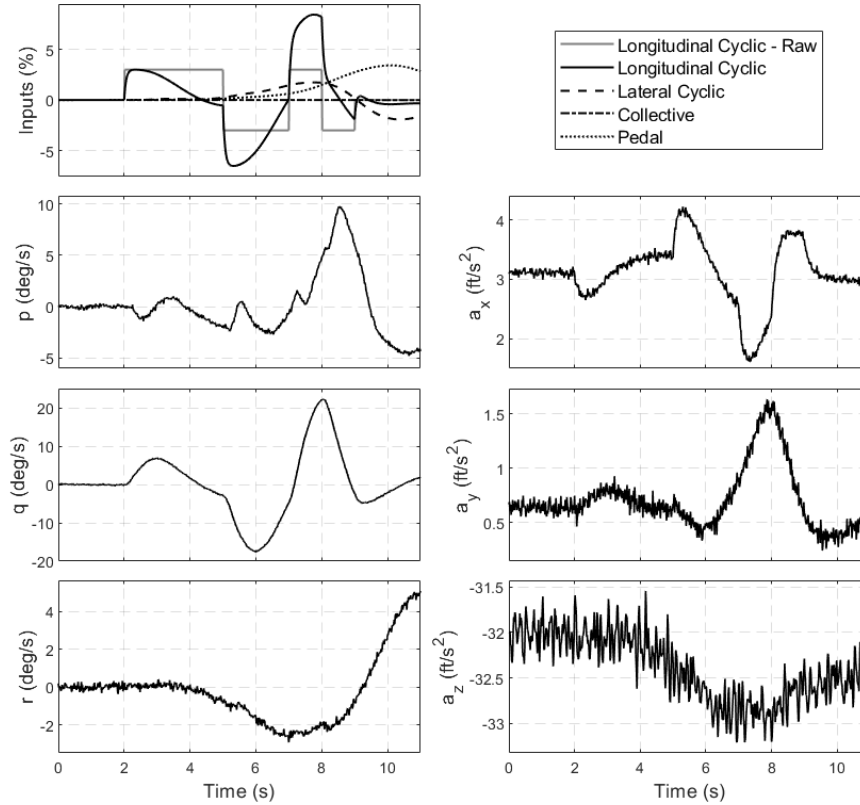


Figure 2.6: 3211 type input given to longitudinal cyclic channel of truth model and its response in hover

2.2 Mathematical Model

In this work, the dynamics of a helicopter in hover and forward flight conditions are identified with the developed software, as a physical mathematical model. For such models, determination of the complexity and the structure of the model depends on the application [18, 44]. Since this work focuses on identification in time domain, a state space representation for aircraft dynamics is adopted as the mathematical model.

Before moving further, some terms and definitions must be examined. First of all, body fixed reference frame is used throughout the study, as it is preferred for air vehicles with the ability to hover [44]. The origin of this coordinate frame is located at the center of gravity of the aircraft. x -axis is towards the nose of the aircraft, z -axis points towards the downwards of the fuselage and y -axis obeys the right-hand rule as illustrated in figure 2.7. The notation associated with this coordinate system is also important. X , Y and Z are resultant aerodynamic force components along body

axes. L , M and N are rolling, pitching and yawing moments. u , v and w are the translational velocities along body axes and p , q and r are roll, pitch and yaw rates around these axes. To express the orientation of the aircraft relative to Earth fixed coordinate frame, Euler angles are utilized. These are roll angle ϕ , pitch angle θ and yaw angle ψ .

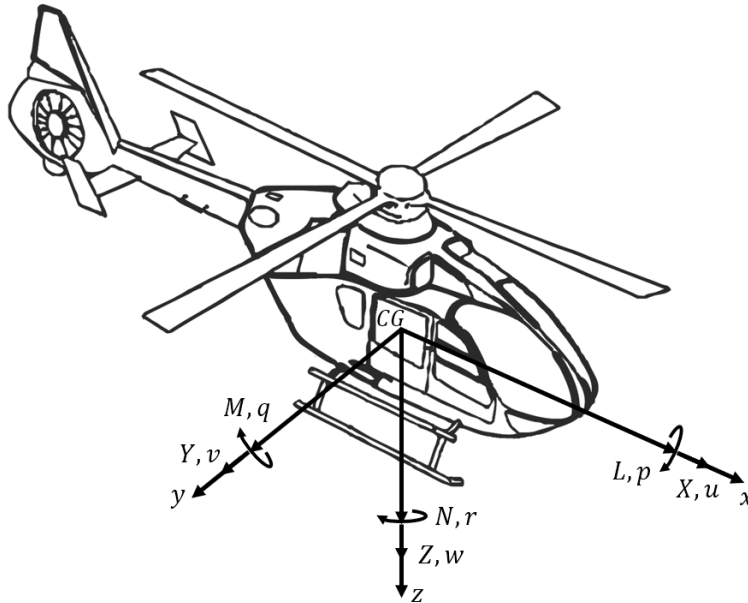


Figure 2.7: Body fixed reference frame (adapted from [42])

The rigid body dynamics of an aircraft with six degrees of freedom can be expressed with equations of motion derived from Newton's second law. The derivation for equations of motion is not explicitly shown here, but can be found in [10]. The nonlinear equations of motion are then linearized around a trim condition using small perturbation theory [10]. The trim condition of the aircraft is expressed with values of states at trim indicated with subscript 0 as u_0 , v_0 , w_0 , θ_0 and ϕ_0 . Then the linearized set of equations of motion can be represented in a state space form. State space representation of a dynamic system is a set of first order differential equations. It is a convenient manner to represent aircraft dynamics as with appropriate selection of system states, system parameters become aerodynamic derivatives.

The state and control perturbation parameters are translational velocities u , v , w , angular rates p , q , r , Euler angles θ , ϕ and control deflections δ_{long} , δ_{lat} , δ_{col} , δ_{ped} . Note that the adopted notation for aircraft controls is for rotorcraft. For fixed wing aircraft,

the aircraft controls can be expressed as δ_{elev} , δ_{ail} , δ_{rud} , δ_{thr} . The yaw angle ψ is omitted as a perturbation state, as it only indicates the aircraft's heading, not the dynamics. The aerodynamic forces and moments are expressed as Taylor Series expansions. By ignoring higher order terms, the linearized equations of motion are acquired as a set of equations 2.1. The aerodynamic forces and moments with subscripts in the equations indicate partial derivatives of these forces and moments relative to the parameter in the subscript. The derivations of these equations and the assumptions made can be found in [10, 44]. It is important to note that the linearized equations presented here indicate the dynamics from the trimmed state of the aircraft.

$$\begin{aligned} \dot{u} = & (-g \cos \theta_0) \theta + X_u u + X_w w + (X_q - w_0) q + X_v v + X_p p + (X_r + v_0) r \\ & + X_{\delta_{long}} \delta_{long} + X_{\delta_{lat}} \delta_{lat} + X_{\delta_{col}} \delta_{col} + X_{\delta_{ped}} \delta_{ped} \end{aligned} \quad (2.1a)$$

$$\begin{aligned} \dot{v} = & (-g \sin \phi_0 \sin \theta_0) \theta + (g \cos \phi_0 \cos \theta_0) \phi + Y_u u + Y_w w + Y_q q + Y_v v \\ & + (Y_p + w_0) p + (Y_r - u_0) r + Y_{\delta_{long}} \delta_{long} + Y_{\delta_{lat}} \delta_{lat} \\ & + Y_{\delta_{col}} \delta_{col} + Y_{\delta_{ped}} \delta_{ped} \end{aligned} \quad (2.1b)$$

$$\begin{aligned} \dot{w} = & (-g \cos \phi_0 \sin \theta_0) \theta + (-g \sin \phi_0 \cos \theta_0) \phi + Z_u u + Z_w w + (Z_q + u_0) q \\ & + Z_v v + (Z_p - v_0) p + Z_\phi \phi + Z_r r + Z_{\delta_{long}} \delta_{long} + Z_{\delta_{lat}} \delta_{lat} \\ & + Z_{\delta_{col}} \delta_{col} + Z_{\delta_{ped}} \delta_{ped} \end{aligned} \quad (2.1c)$$

$$\begin{aligned} \dot{p} = & L_u u + L_w w + L_q q + L_v v + L_p p + L_r r \\ & + L_{\delta_{long}} \delta_{long} + L_{\delta_{lat}} \delta_{lat} + L_{\delta_{col}} \delta_{col} + L_{\delta_{ped}} \delta_{ped} \end{aligned} \quad (2.1d)$$

$$\begin{aligned} \dot{q} = & M_u u + M_w w + M_q q + M_v v + M_p p + M_r r + M_{\delta_{long}} \delta_{long} + M_{\delta_{lat}} \delta_{lat} \\ & + M_{\delta_{col}} \delta_{col} + M_{\delta_{ped}} \delta_{ped} \end{aligned} \quad (2.1e)$$

$$\begin{aligned} \dot{r} = & N_u u + N_w w + N_q q + N_v v + N_p p + N_r r \\ & + N_{\delta_{long}} \delta_{long} + N_{\delta_{lat}} \delta_{lat} + N_{\delta_{col}} \delta_{col} + N_{\delta_{ped}} \delta_{ped} \end{aligned} \quad (2.1f)$$

$$\dot{\theta} = q \cos \phi_0 - r \sin \phi_0 \quad (2.1g)$$

$$\dot{\phi} = q \sin \phi_0 \tan \theta_0 + p + r \cos \phi_0 \tan \theta_0 \quad (2.1h)$$

The linearized set of equations can be written in state space form as:

$$\dot{\mathbf{x}} = A\mathbf{x} + B\mathbf{u} \quad (2.2)$$

$$\mathbf{y} = C\mathbf{x} + D\mathbf{u} \quad (2.3)$$

Where \mathbf{x} is the state vector and \mathbf{u} is the control vector given in equations 2.4 and 2.5 respectively. Equation 2.7 shows the eight by eight A matrix, which consists of stability derivatives reflecting the sensitivity of aerodynamic forces and moments to state parameters. Similarly, the elements of B matrix are control derivatives, reflecting the sensitivity of forces and moments to aircraft controls, which is given in 2.8. \mathbf{y} is the measurement vector as shown in 2.6. In real life flight test applications, the angular rate measurements are obtained directly from the gyroscope and the Euler angles are acquired by the integration of angular rates. The non-gravitational acceleration a body has is called specific acceleration and since accelerometers measure specific accelerations, terms a_x , a_y and a_z are present in the measurement vector instead of translational velocities. Consequently, for the measurements calculated by 2.3, the C and D matrices are constructed such that specific accelerations are present in the measurement vector as shown in equations 2.9 and 2.10.

$$\mathbf{x} = \begin{bmatrix} u & w & q & \theta & v & p & \phi & r \end{bmatrix}^T \quad (2.4)$$

$$\mathbf{u} = \begin{bmatrix} \delta_{long} & \delta_{lat} & \delta_{coll} & \delta_{ped} \end{bmatrix}^T \quad (2.5)$$

$$\mathbf{y} = \begin{bmatrix} a_x & a_z & q & \theta & a_y & p & \phi & r \end{bmatrix}^T \quad (2.6)$$

$$A = \begin{bmatrix} X_u & X_w & X_q - w_0 & -g \cos \theta_0 & X_v & X_p & 0 & X_r + v_0 \\ Z_u & Z_w & Z_q + u_0 & -g \cos \phi_0 \cos \theta_0 & Z_v & Z_p - v_0 & -g \sin \phi_0 \cos \theta_0 & Z_r \\ M_u & M_w & M_q & 0 & M_v & M_p & 0 & M_r \\ 0 & 0 & \cos \theta_0 & 0 & 0 & 0 & 0 & -\sin \theta_0 \\ Y_u & Y_w & Y_q & -g \sin \phi_0 \sin \theta_0 & Y_v & Y_p + w_0 & g \cos \phi_0 \cos \theta_0 & Y_r - u_0 \\ L_u & L_w & L_q & 0 & L_v & L_p & 0 & L_r \\ 0 & 0 & \sin \phi_0 \tan \theta_0 & 1 & 0 & 0 & 0 & \cos \phi_0 \tan \theta_0 \\ N_u & N_w & N_q & 0 & N_v & N_p & 0 & N_r \end{bmatrix} \quad (2.7)$$

$$B = \begin{bmatrix} X_{\delta_{\text{long}}} & X_{\delta_{\text{lat}}} & X_{\delta_{\text{coll}}} & X_{\delta_{\text{ped}}} \\ Z_{\delta_{\text{long}}} & Z_{\delta_{\text{lat}}} & Z_{\delta_{\text{coll}}} & Z_{\delta_{\text{ped}}} \\ M_{\delta_{\text{long}}} & M_{\delta_{\text{lat}}} & M_{\delta_{\text{coll}}} & M_{\delta_{\text{ped}}} \\ 0 & 0 & 0 & 0 \\ Y_{\delta_{\text{long}}} & Y_{\delta_{\text{lat}}} & Y_{\delta_{\text{coll}}} & Y_{\delta_{\text{ped}}} \\ L_{\delta_{\text{long}}} & L_{\delta_{\text{lat}}} & L_{\delta_{\text{coll}}} & L_{\delta_{\text{ped}}} \\ 0 & 0 & 0 & 0 \\ N_{\delta_{\text{long}}} & N_{\delta_{\text{lat}}} & N_{\delta_{\text{coll}}} & N_{\delta_{\text{ped}}} \end{bmatrix} \quad (2.8)$$

$$C = \begin{bmatrix} X_u & X_w & X_q - w_0 & 0 & X_v & X_p & 0 & X_r + v_0 \\ Z_u & Z_w & Z_q + u_0 & 0 & Z_v & Z_p - v_0 & 0 & Z_r \\ 0 & 0 & 1 & 0 & 0 & 0 & 0 & 0 \\ 0 & 0 & 0 & 1 & 0 & 0 & 0 & 0 \\ Y_u & Y_w & Y_q & 0 & Y_v & Y_p + w_0 & 0 & Y_r - u_0 \\ 0 & 0 & 0 & 0 & 0 & 1 & 0 & 0 \\ 0 & 0 & 0 & 0 & 0 & 0 & 1 & 0 \\ 0 & 0 & 0 & 0 & 0 & 0 & 0 & 1 \end{bmatrix} \quad (2.9)$$

$$D = \begin{bmatrix} X_{\delta_{\text{long}}} & X_{\delta_{\text{lat}}} & X_{\delta_{\text{coll}}} & X_{\delta_{\text{ped}}} \\ Z_{\delta_{\text{long}}} & Z_{\delta_{\text{lat}}} & Z_{\delta_{\text{coll}}} & Z_{\delta_{\text{ped}}} \\ 0 & 0 & 0 & 0 \\ 0 & 0 & 0 & 0 \\ Y_{\delta_{\text{long}}} & Y_{\delta_{\text{lat}}} & Y_{\delta_{\text{coll}}} & Y_{\delta_{\text{ped}}} \\ 0 & 0 & 0 & 0 \\ 0 & 0 & 0 & 0 \\ 0 & 0 & 0 & 0 \end{bmatrix} \quad (2.10)$$

The first four states in the state vector x are mainly associated with the longitudinal dynamics, and the last four are related to lateral dynamics of the aircraft. By adopting this order, the coupling terms in A matrix can be easily seen. The assumption of uncoupled longitudinal and lateral dynamics for fixed wing aircraft is generally a reasonable one. However, the longitudinal and lateral dynamics of helicopters cannot be assumed as uncoupled, mainly due to the presence of rotor. One good example of this coupled motion is due to gyroscopic effect of the rotor. The rotor of a helicopter can be thought of as a giant gyroscope. As the helicopter and hence the rotor has a nonzero pitch rate, a moment is generated in the lateral axis, which produces a nonzero roll rate. For this reason, it is thought to be necessary to include both longitudinal and lateral states in the state space formulation of the identification model, as also stated in [44]. Therefore, the identification model has all aerodynamic derivatives shown in set of equations 2.1 as identification parameters.

The state space model obtained is a set of first order differential equations expressing the dynamic behavior of the aircraft. In order to identify a mathematical model that shows similar behavior to the truth model data, the mathematical model must be simulated to get outputs. For this purpose, numerical integration is used. Numerous numerical integration methods are applicable for simulation of mathematical models, depending on the accuracy required. The simplest of them is the Taylor Series based Euler's method, which is a first order accurate numerical method used to approximate solutions of ordinary differential equations (ODE) with known initial conditions. Let x be the state vector to be calculated and Δt to be the simulation time step. It approximates the value at the next time step as:

$$\mathbf{x}(t + \Delta t) = \mathbf{x}(t) + (\Delta t)f(t, \mathbf{x}(t)) \quad (2.11)$$

Where $f(t, \mathbf{x}(t)) = \dot{\mathbf{x}}(t)$. By using i as the time step index, the equation above can also be written as:

$$\mathbf{x}_{i+1} = \mathbf{x}_i + (\Delta t)\dot{\mathbf{x}}_i \quad (2.12)$$

Therefore, by iterating the algorithm, the time histories of states in vector \mathbf{x} can be acquired. There are other numerical integration methods that can be used for simulation purposes, such as second order accurate Heun's method or Runge-Kutta methods with greater order of accuracy. However, as the accuracy of the numerical integration increases, the computational cost also increases. Therefore, Euler's method is adopted for this study to avoid computational overhead and its accuracy is thought to be sufficient.

2.2.1 Modelling of Additional Dynamics

The model structure discussed so far consists of linearized equations of motion for rigid body dynamics. This study, however, focuses on identification of rotorcraft dynamics. Due to the presence of rotor, additional dynamics to the conventional 6DoF model are observed. These transient effects can be observed in truth model signals as higher frequency behavior and delayed response between the states and controls. Tischler [44] proposed modelling each of the additional dynamics as additional states to the 6DoF model structure. The obtained hybrid model structure has 20 states to be modelled and identified.

One example to this issue is given in [18] as the downwash lag effect in a fixed wing aircraft. The angle of attack of the horizontal tail of an aircraft is altered due to downwash of the wing. A change in the flow over the wing also results in a change in downwash flow. Hence, the angle of attack that the horizontal tail experiences is altered. However, due to the transit time effect, the change in the angle of attack of the horizontal tail is not instant, but with a time delay. This time delay can be used to

model the angle of attack of the horizontal tail. Following [10, 18], the angle of attack of the horizontal tail can be modelled as:

$$\alpha_H = \alpha_{wb} + i_H - \varepsilon_H + \alpha_{dyn} \quad (2.13)$$

Where α_{wb} is the angle of attack of the wing-body, i_H is the horizontal tail trim angle ε_H is the downwash angle and α_{dyn} is the dynamic angle of attack. The downwash angle is further expressed as:

$$\varepsilon_H = \frac{\partial \varepsilon_H}{\partial \alpha} \alpha(t - \tau) + \frac{\partial \varepsilon_H}{\partial C_T} C_T(t - \tau) \quad (2.14)$$

Where the partial derivatives are the unknown parameters to be identified, C_T is the thrust coefficient and τ represents the transient time delay. In this example, the time delay is only modelled to account for the transient change in the flow characteristics. Jategaonkar [18] proposes delay arrays as a more general solution to model additional dynamics in a system. In this approach, any parameter in the model structure can be delayed, and the delay amount can be included as an unknown parameter. During optimization, the unknown time delays should be identified together with the rest of the unknown parameters. To model the additional dynamics in a helicopter, the delay array approach can be utilized. Some key derivatives in the model structure can be delayed to reflect the higher order dynamics.

Additional dynamics in the helicopters mainly stem from the existence of rotor. It not only introduces asymmetrical flight conditions throughout the operational envelope, but also the aircraft cannot be considered as a single rigid body. Some of these dynamics are results of rotor blade flapping, lead lag dynamics, coning/inflow dynamics and yaw/engine dynamics. Implementation of time delays in the model structure to account for such dynamics requires understanding of rotor dynamics, as the parameters to be delayed must be selected reasonably. It is to avoid multiple solutions during optimization, and time delays lacking physical meanings. One example of the delays in helicopter dynamics is simply the input delay, as helicopters utilize main rotor flapping to maneuver. The cyclic and collective controls do not directly change the flapping angles, instead, they modify the pitch angles of each blade and the flapping

is developed with the rotation of the rotor. To represent this behavior, time delays can be added to the derivatives relating the longitudinal and lateral cyclic controls to the pitch and roll moments in the control matrix.

The pitch to roll coupling in helicopters can be given as another example to this discussion. The main rotor acts like a giant gyroscope, as whenever the helicopter has a nonzero pitch rate or roll rate, the rotor has a nonzero moment in the other direction. To illustrate, if the helicopter pitches up, the rotor develops a rolling moment resulting in coupled longitudinal and lateral dynamics. To account for this gyroscopic effect, time delays can be introduced to derivatives which relate pitch and roll rates to moments. Equations 2.15 and 2.16 represent the implementation of time delays to related parameters in system and control matrices, where symbol τ is used to represent time delays. Each time delay can have a different value, which are left as unknown parameters to be identified. However, they cannot physically take negative values, as that would mean using information from future times. Note that these equations with all time delays employed on discussed parameters is only representative, as identification in different flight conditions can require only few of these time delays or none at all in the model structure.

$$\begin{aligned} \dot{p} = & L_p p(t - \tau_1) + \dots + L_q q(t - \tau_2) + \dots \\ & + L_{\delta_{long}} \delta_{long}(t - \tau_3) + \dots + L_{\delta_{lat}} \delta_{lat}(t - \tau_4) \end{aligned} \quad (2.15)$$

$$\begin{aligned} \dot{q} = & M_p p(t - \tau_5) + \dots + M_q q(t - \tau_6) + \dots \\ & + M_{\delta_{long}} \delta_{long}(t - \tau_7) + \dots + M_{\delta_{lat}} \delta_{lat}(t - \tau_8) \end{aligned} \quad (2.16)$$

2.3 Output-Error Method

Having discussed the mathematical model to be estimated and adequate input types to be used for identification purposes, the parameter estimation method used in this work can now be discussed.

There are numerous studies that focus on identification of aircraft dynamics in both frequency and time domains. This study covers identification of rotorcraft dynamics

in time domain using maximum likelihood based output error algorithm. It is one of the two central identification methods, while the other is filter-error method [18]. Maximum likelihood output-error method is widely used for fixed wing aircraft and rotorcraft system identification purposes since 1960s. It can handle both linear and nonlinear model structures with arbitrary complexity [18]. The output-error method focuses on minimizing the error between the actual system responses (flight test measurements or truth model outputs) and simulated mathematical model outputs by iterating the unknown system parameters. As it is an iterative approach, model response must be simulated multiple times at each iteration step until a local minimum in the cost function is achieved.

2.3.1 Maximum Likelihood Estimation Principle

The maximum likelihood estimation theory is based on statistics, where the likelihood of a number coming within a range of values is expressed by probability density functions. Although the principle is applicable to any type of probability density functions, Gaussian (normal) distribution is considered throughout this derivation. A Gaussian distribution is defined by mean and covariance values. Let a be a random variable, then the mean value and covariance are defined as:

$$m = E\{a\} \quad (2.17)$$

$$\sigma^2 = E\{(a - m)^2\} \quad (2.18)$$

Where E is the expected value, which can also be expressed as the sum of all possible values, multiplied by their probability of occurrence. Using the definitions of mean value m and covariance σ^2 , the Gaussian distribution function of a random variable a can be written as [18]:

$$p(a) = \frac{1}{\sqrt{2\pi}\sigma} \exp\left[-\frac{(a - m)^2}{2\sigma^2}\right] \quad (2.19)$$

The discussion can also be extended for a multidimensional distribution where \mathbf{a} is a vector with n Gaussian distribution elements $\mathbf{a}^T = (a_1, \dots, a_n)$ and correspondingly

$\mathbf{m}^T = (m_1, \dots, m_n)$. The joint probability distribution function is given as:

$$p(a_1, \dots, a_n) = \frac{1}{(2\pi)^{n/2} \sqrt{|R|}} \exp \left[-\frac{1}{2} (\mathbf{a} - \mathbf{m})^T R^{-1} (\mathbf{a} - \mathbf{m}) \right] \quad (2.20)$$

R in equation 2.20 is the measurement error covariance matrix calculated as:

$$R_{ij} = E\{(a_i - m_i)(a_j - m_j)\} = \sigma_i \sigma_j \rho_{ij} \quad (2.21)$$

Where ρ_{ij} are correlation coefficients with $\rho_{ii} = 1$.

In the use of the maximum likelihood principle in system identification, the parameter vector of Θ which is unknown at the beginning is estimated using a set of observations (z_1, z_2, \dots, z_N) with N number of samples. Defining the conditional probability $p(z | \Theta)$ as the probability of z given Θ . Assuming that the observations in vector z are independent of each other, the probability $p(z | \Theta)$ can be written as the multiplication of the conditional probability of each observation.

$$p(z | \Theta) = \prod_{k=1}^N p(z_k | \Theta) = p(z_1 | \Theta) \cdot p(z_2 | \Theta) \cdot p(z_3 | \Theta) \cdot \dots \cdot p(z_N | \Theta) \quad (2.22)$$

It is shown that for a multidimensional Gaussian distribution of variables, the joint probability function also depends on the measurement noise covariance matrix R . Therefore, the likelihood function can be expressed as $p(z(t_1), \dots, z(t_N) | \Theta, R)$ given parameters Θ and R .

The aim of the maximum likelihood parameter estimate founded by Fisher is to search values of unknown parameters Θ which maximizes the probability of $p(z | \Theta, R)$ [18]. Therefore, the likelihood function does not deal with the probability distribution of unknown parameters Θ but the probability distribution of z . In order to implement the maximum likelihood function to the system identification problem, the error $\mathbf{v}(t_k) = \mathbf{z}(t_k) - \mathbf{y}(t_k)$ is defined. z is the vector of observations and \mathbf{y} is the vector of model outputs. Assuming that the error \mathbf{v} at each time step t_k are statistically independent, the following relation can be written:

$$E\{\mathbf{v}(t_k)\mathbf{v}(t_l)^T\} = R\delta_{kl} \quad (2.23)$$

δ_{kl} is the Kronecker delta, which takes the value of 1 when $k = l$ and 0 otherwise. The probability density at a singular time is given to be [18]:

$$p(\mathbf{z}(t_k) | \Theta, R) = \frac{1}{(2\pi)^{n_y/2} \sqrt{|R|}} \times \exp \left[-\frac{1}{2} \{\mathbf{z}(t_k) - \mathbf{y}(t_k)\}^T R^{-1} \{\mathbf{z}(t_k) - \mathbf{y}(t_k)\} \right] \quad (2.24)$$

Where n_y is the number of observation variables. The likelihood function including all time steps $p(\mathbf{z}(t_1), \dots, \mathbf{z}(t_N) | \Theta, R)$ becomes:

$$p(\mathbf{z}(t_1), \dots, \mathbf{z}(t_N) | \Theta, R) = \prod_{k=1}^N p(\mathbf{z}(t_k) | \Theta, R) \\ = \{(2\pi)^{n_y} |R|\}^{-N/2} \exp \left[-\frac{1}{2} \sum_{k=1}^N [\mathbf{z}(t_k) - \mathbf{y}(t_k)]^T R^{-1} [\mathbf{z}(t_k) - \mathbf{y}(t_k)] \right] \quad (2.25)$$

The parameters Θ and R that maximizes the probability $p(\mathbf{z}(t_1), \dots, \mathbf{z}(t_N) | \Theta, R)$ can be found by simply taking the derivatives of 2.25 with respect to Θ and R and equating them to zero. However, for an easier practice, the equivalent problem of minimization of the negative logarithm of the maximum likelihood function $L(\mathbf{z} | \Theta, R)$ is considered.

$$L(\mathbf{z} | \Theta, R) = \frac{1}{2} \sum_{k=1}^N [\mathbf{z}(t_k) - \mathbf{y}(t_k)]^T R^{-1} [\mathbf{z}(t_k) - \mathbf{y}(t_k)] \\ + \frac{N}{2} \ln(\det(R)) + \frac{Nn_y}{2} \ln(2\pi) \quad (2.26)$$

2.3.2 Implementation of Maximum Likelihood Parameter Estimation on Mathematical Models

As a general form, a mathematical model of a linear or nonlinear system can be expressed as [14]:

$$\dot{\mathbf{x}} = f(\Theta, \mathbf{x}(t), \mathbf{u}(t)), \quad \mathbf{x}(t_0) = \mathbf{x}_0 \quad (2.27)$$

$$\mathbf{y} = g(\Theta, \mathbf{x}(t), \mathbf{u}(t)) \quad (2.28)$$

$$\mathbf{z}(t_k) = \mathbf{y}(t_k) + \mathbf{v}(t_k), \quad t_k = 1, \dots, N \quad (2.29)$$

In this mathematical model, it is assumed that inputs are measured without error and process noise is negligible, meaning that only measurement noise is present. The measurement noise is assumed to be defined by a Gaussian distribution with zero mean and identity covariance. It is also assumed that the measurement errors at each time step t_k are statistically independent, as stated in the previous section. The cost function to be minimized is the negative logarithm of the maximum likelihood function given in equation 2.26 which can also be denoted as $J(\Theta, R)$. The last term in this cost function has a constant value, as the number of observation parameters and number of observation data points have a constant value for a given data set. Therefore, its existence has no impact on the minimization problem. For the rest of the terms, the measurement noise covariance matrix R has to be known or calculated.

If R is known, the second term in the cost function becomes a constant and can again be dropped as it does not affect the optimization procedure. The cost function then becomes:

$$J(\Theta) = \frac{1}{2} \sum_{k=1}^N [\mathbf{z}(t_k) - \mathbf{y}(t_k)]^T R^{-1} [\mathbf{z}(t_k) - \mathbf{y}(t_k)] \quad (2.30)$$

However, in the problem examined in this study, the matrix R is not known and has to be calculated. First, an expression for R is obtained by taking the partial derivative of the cost function with respect to R and setting it to zero [18].

$$R = \frac{1}{N} \sum_{k=1}^N [\mathbf{z}(t_k) - \mathbf{y}(t_k)] [\mathbf{z}(t_k) - \mathbf{y}(t_k)]^T \quad (2.31)$$

Substitution of expression 2.31 into cost function equation given in 2.26 yields

$$J(\Theta) = \frac{1}{2} n_y N + \frac{N}{2} \ln(\det(R)) + \frac{N n_y}{2} \ln(2\pi) \quad (2.32)$$

As mentioned, for a given data set, the values for n_y and N are constant and known. Thus, the cost function is reduced to the determinant of R .

$$J(\Theta) = \det(R) \quad (2.33)$$

The measurement noise covariance matrix R is a diagonal matrix as stated by equation 2.23. Therefore, the cost function to be minimized is calculated by the product of the diagonal elements in matrix R .

Now, the aim is to minimize equation 2.33 using an optimization algorithm. First, appropriate initial guesses for unknown system parameters Θ are chosen. Then the mathematical model outputs \mathbf{y} are calculated. Using measurements \mathbf{z} , measurement noise covariance matrix R is calculated. Utilizing a nonlinear optimization algorithm, values for Θ are updated. This procedure is repeated until sufficient convergence is achieved.

2.3.3 Gauss-Newton Algorithm

The Gauss-Newton algorithm is a modified form of the Newton-Raphson algorithm. It is a second order nonlinear optimization method that is widely used for aircraft system identification. The aim is to minimize the cost function by iterating the values for unknown system parameters Θ , therefore the condition for minimization is given to be:

$$\frac{\partial J(\Theta)}{\partial \Theta} = 0 \quad (2.34)$$

The first two terms of the Taylor expansion about i th iteration value of the parameter vector Θ is:

$$\left(\frac{\partial J}{\partial \Theta}\right)_{i+1} \approx \left(\frac{\partial J}{\partial \Theta}\right)_i + \left(\frac{\partial^2 J}{\partial \Theta^2}\right)_i \Delta \Theta \quad (2.35)$$

$\Delta \Theta$ is the parameter update between iterations i and $i + 1$. The term multiplied with $\Delta \Theta$ is the Hessian matrix, which is the second derivatives of the cost function with respect to system parameters at i th iteration. Using the minimization criteria in equation 2.34, the parameter update becomes:

$$\Delta \Theta = - \left[\left(\frac{\partial^2 J}{\partial \Theta^2}\right)_i \right]^{-1} \left(\frac{\partial J}{\partial \Theta}\right)_i \quad (2.36)$$

By using initial guesses for system parameters Θ_0 , the iteration can be initiated to find the minimum of the cost function. This procedure is called the Newton-Raphson method. The parameter updates are larger when the cost function is away from its minima, and they become smaller as the cost is minimized. The number of steps required for minimization depends on the initial values of the parameters and the shape of the cost function. To apply the minimization algorithm to the maximum likelihood function, the first and second partial derivatives of equation 2.30 with respect to parameters Θ are calculated.

$$\frac{\partial J}{\partial \Theta} = - \sum_{k=1}^N \left[\frac{\partial \mathbf{y}(t_k)}{\partial \Theta} \right]^T R^{-1} [\mathbf{z}(t_k) - \mathbf{y}(t_k)] \quad (2.37)$$

$$\frac{\partial^2 J}{\partial \Theta^2} = \sum_{k=1}^N \left[\frac{\partial \mathbf{y}(t_k)}{\partial \Theta} \right]^T R^{-1} \frac{\partial \mathbf{y}(t_k)}{\partial \Theta} - \sum_{k=1}^N \left[\frac{\partial^2 \mathbf{y}(t_k)}{\partial \Theta^2} \right]^T R^{-1} [\mathbf{z}(t_k) - \mathbf{y}(t_k)] \quad (2.38)$$

The calculation of the first gradient of the cost function given in equation 2.37 is simple, as measured data and system response are known and R can be calculated from 2.31. It only requires the calculation of response gradients $\partial \mathbf{y}(t_k)/\partial \Theta$. The calculation of the second gradient of the cost function, however, is more involved as it requires calculation of second response gradients. The optimization procedure tries

to minimize the error between measurements and system responses. Therefore, the last term in equation 2.38 becomes negligible with sufficient data length due to the assumption of zero mean and identity covariance [18]. The second gradient of J can be approximated as:

$$\frac{\partial^2 J}{\partial \Theta^2} \approx \sum_{k=1}^N \left[\frac{\partial \mathbf{y}(t_k)}{\partial \Theta} \right]^T R^{-1} \left[\frac{\partial \mathbf{y}(t_k)}{\partial \Theta} \right] \quad (2.39)$$

With this simplification, the algorithm is called the Gauss-Newton method or modified Newton-Raphson method. Denoting the parameter update at each iteration step i as:

$$\Theta_{i+1} = \Theta_i + \Delta \Theta \quad (2.40)$$

The Gauss-Newton parameter update vector $\Delta \Theta$ at each iteration can be calculated from equation 2.41.

$$\Delta \Theta = \mathcal{F}^{-1} - \mathcal{G} \quad (2.41)$$

$$\mathcal{F} = \sum_{k=1}^N \left[\frac{\partial \mathbf{y}(t_k)}{\partial \Theta} \right]^T R^{-1} \left[\frac{\partial \mathbf{y}(t_k)}{\partial \Theta} \right] \quad (2.42)$$

$$\mathcal{G} = - \sum_{k=1}^N \left[\frac{\partial \mathbf{y}(t_k)}{\partial \Theta} \right]^T R^{-1} [\mathbf{z}(t_k) - \mathbf{y}(t_k)] \quad (2.43)$$

\mathcal{F} is the Hessian matrix and \mathcal{G} is the gradient vector. Since the measurement noise covariance matrix R is diagonal, the inverse of this matrix is again a diagonal matrix with reciprocals of the elements. From equation 2.31, matrix R represents the squared and summed errors between each measurement and estimated signal, divided by the number of data points. The R^{-1} term in expressions 2.42 and 2.43 represents a division to squared errors, which is dependent on the units of the signals. This term is multiplied by partial differences from both sides in 2.42 and by partial differences

from one side and errors from the other side in 2.43. Therefore, the calculations of \mathcal{F} , \mathcal{G} and the parameter update vector do not depend on the units of the measurements.

Hessian and gradient vector are both constructed from partial derivatives of the system response y with respect to model parameters Θ . Therefore, these derivatives have to be calculated to construct \mathcal{F} and \mathcal{G} . The derivatives can be calculated analytically by differentiating equation 2.28 with respect to Θ , however, this approach becomes cumbersome when the model structure is nonlinear [18]. To account for any model structure, numerical differentiation is employed. The forward differentiation of model responses with respect to system parameters is expressed as:

$$\begin{aligned} \left[\frac{\partial \mathbf{y}(t_k)}{\partial \Theta} \right]_{ij} &\approx \frac{y_i^p(t_k) - y_i(t_k)}{\delta \Theta_j}; \quad i = 1, \dots, n_y; \quad j = 1, \dots, n_q \\ &\approx \frac{g_i(\mathbf{x}^p(t_k), \mathbf{u}(t_k), \Theta + \delta \Theta_j \mathbf{e}^j) - g_i(\mathbf{x}(t_k), \mathbf{u}(t_k), \Theta)}{\delta \Theta_j} \end{aligned} \quad (2.44)$$

Where n_y is the number of observation variables, n_q is the number of unknown system parameters. The superscript p indicates the perturbed variables $\delta \Theta_j$ is the perturbed system parameter at j th element and \mathbf{e}^j is a vector with one on j th index and zero elsewhere. As can be seen from the expression, the unperturbed system response is subtracted from the perturbed system response and divided by the perturbation. The perturbed system response is obtained by simulating the mathematical model with perturbed system parameters ($\Theta + \delta \Theta_j \mathbf{e}^j$). The perturbation size for each parameter is taken to be 10^{-6} times the value of that parameter. This approach to calculate the perturbation size is proposed by Jategaonkar in [18], however, since the difference between perturbed and unperturbed system responses are divided to the perturbation, different perturbation sizes also work as long as they do not divert the model from the linear region.

$$\delta \Theta_j = 10^{-6} \Theta_j \quad (2.45)$$

If the value of a parameter is zero, then the perturbation is directly taken as 10^{-6} as suggested in [18].

The forward difference approach presented in 2.44 is a first order accurate approximation for the first derivative of a function. Central differentiation, a second order accurate approximation method, can also be used to achieve greater precision. However, it requires the perturbations to be given in both positive and negative directions. Calculation of the sensitivity matrix $\partial \mathbf{y} / \partial \Theta$ is computationally expensive, as all tests must be simulated for each perturbed variable in Θ . Therefore, to avoid further computational burden, forward difference formula is thought to be satisfactory and used to obtain sensitivity matrices.

2.3.4 Levenberg-Marquardt Algorithm

The discussed Gauss-Newton method forms the basis for the maximum likelihood parameter identification in this work. The parameter update law given in equation 2.41 works decently in applications where the initial guesses for system parameters are not far from their optimal values and when the identified system behavior is linear. However, the algorithm is prone to diverge in many applications where no knowledge is available for good initial parameter guesses. In order to avoid divergence, some approaches proposed in [18].

The first approach is to reduce the step size by directly multiplying the parameter update vector $\Delta \Theta$ with a learning rate gain α between 0 and 1 as shown in equation 2.46. With this approach, the optimization iteration takes smaller parameter update steps and intermediate divergence can be avoided in some cases. This approach can also be extended such that the step size reduction is repeated until a reduction in cost function in a given iteration step is achieved. Even though this approach is useful to prevent divergence in some cases, the optimization loop can still diverge depending on the initial guesses of parameters and the cost function.

$$\Theta_{i+1} = \Theta_i + \alpha \Delta \Theta \quad (2.46)$$

Another approach is to use a line search algorithm to determine the step size of iteration. The parameter update vector is again multiplied with a gain, but this time the gain is variable and denoted as α_i . The algorithm aims to have maximum reduction

in cost function at each iteration by calculating the proper value for α_i .

$$\Theta_{i+1} = \Theta_i + \alpha_i \Delta \Theta \quad (2.47)$$

There are multiple line search algorithms to calculate α_i , which can be found in [11, 29]. Similar to previous approach, line search methods result in improvement in parameter convergence as the optimization iteration converges in some cases whereas the base Gauss-Newton parameter update method diverges.

Lastly, Levenberg-Marquardt algorithm can be used to remedy intermediate divergence of the optimization loop and to have parameter update in the steepest descent direction. The algorithm uses the Gauss-Newton method parameter update 2.40 as it is, however the calculation of the parameter update vector is modified.

$$(\mathcal{F} + \lambda I) \Delta \Theta = -\mathcal{G} \quad (2.48)$$

In the expression 2.48, λ is the Levenberg-Marquardt parameter that is calculated to obtain the direction of maximum reduction of cost function. It can be seen that for $\lambda = 0$, the expression becomes the same as Gauss-Newton algorithm. As the value of λ increases, the parameter update approaches to steepest descent. The Levenberg-Marquardt algorithm follows few iterative steps at each iteration step of maximum likelihood cost optimization [18, 24]. Using i as the iteration index, the procedure is given as follows.

1. A reduction factor ν is chosen such that $\nu > 1$. Let $\lambda^{(i-1)}$ indicate the LM parameter in the previous iteration. Select an initial value for $\lambda^{(0)}$ such as $\lambda^{(0)} = 0.001$.
2. For $\lambda^{(i-1)}$ and $\lambda^{(i-1)}/\nu$, calculate the parameter update from 2.48. Then simulate the model and calculate costs $J_i = J(\Theta(\lambda^{i-1}))$ and $J_i^\nu = J(\Theta(\lambda^{i-1}/\nu))$.
3. Follow the logic such that
 - (i) If $J_i^\nu \leq J_{i-1}$, set $\lambda^{(i)} = \lambda^{(i-1)}/\nu$ and $\Delta \Theta = \Delta \Theta (\lambda^{(i-1)}/\nu)$
 - (ii) If $J_i^\nu > J_{i-1}$ and $J_i \leq J_{i-1}$, then let $\lambda^{(i)} = \lambda^{(i-1)}$ and $\Delta \Theta = \Delta \Theta (\lambda^{(i-1)})$

- (iii) Else, $J_i' > J_{i-1}$ and $J_i > J_{i-1}$, then set $\lambda^{(i-1)} = \lambda^{(i-1)}\nu$ and repeat through procedure starting from step 2.

In the first case (indicated by (i)), if the cost obtained using the reduction factor ν is smaller than the previous cost, both the LM parameter and $\Delta\Theta$ are updated. In the second scenario, the cost without using ν provides a lower cost so that $\Delta\Theta$ is updated but LM parameter is kept the same. Lastly, if none of the two costs J_i and J_i' are smaller than the previous cost J_{i-1} , then the LM parameter is increased and the whole algorithm iterates until a lower cost is obtained.

The Gauss-Newton algorithm requires the system responses to be calculated once to obtain the parameter update vector. In addition, Levenberg-Marquardt algorithm creates an inner loop in the optimization algorithm to calculate the parameter update vector with the steepest descent. In one iteration of LM algorithm, the system responses must be calculated at least twice for parameter sets $\Theta(\lambda^{i-1})$ and $\Theta(\lambda^{i-1}/)$. If a lower cost compared to previous iteration is not acquired, λ is updated and the system is simulated two more times per each iteration. This computational burden can result in lengthy run times in problems with large number of unknown parameters, such as identification of system and control matrix parameters of 6DoF systems. However, LM algorithm shows superior performance in preventing divergence of the algorithm. It is also seen that the algorithm can achieve satisfactory results even with initial values far away from their optimal values. Therefore, it is worth to implement the algorithm even with the drawback of prolonged run times. It is found that the algorithm works decently with $\lambda^{(0)} = 0.001$ and $\nu = 2$ for flight vehicle system identification problems.

2.4 Model Structure Determination

The modern system identification methods have been used to identify flight vehicle dynamics since 1960s. The studies have been in the both time and frequency domains, where the identification is generally done for linear model structures as they are easier to deal with. While using a linear model structure, transfer function modelling can be preferred to express the dynamic relation between an input-output pair. Such transfer

functions are unique, and they hastily give insight to the dynamic characteristics of the system response, such as dominant modes and derivatives [44]. As the transfer functions are only used for a single input-output pair, a model involving a multi input multi output (MIMO) structure requires multiple transfer functions to be identified. With the increasing number of system states and control channels, the number of transfer functions to identify increases and becomes cumbersome.

In order to avoid aforementioned issues, state space model structure is adopted in this work to identify a MIMO helicopter system. State space systems are usually the desired final product of system identification for simulation model or control system design [44]. Even though they are better suited for MIMO systems, state space representations of dynamic systems are not unique. Meaning that infinitely many state space systems can be constructed to produce the same model output for the same inputs. Selecting all elements in system and control matrices A and B as identification parameters can result in multiple solutions during optimization. The system responses may converge to measurements, but the values of the parameters can be far from their actual values. In identification of flight vehicle dynamics, identification of the aerodynamic derivatives with high confidence is crucial as they are used for control system design and simulation modelling. Therefore, a model structure determination procedure is required to reduce the uncertainties in the identification parameters.

First of all, the parameters in system and control matrices known from a prior information must be calculated. The state and control matrices with all elements as identification parameters is:

$$A_{8 \times 8} = \begin{bmatrix} \Theta_1 & \Theta_9 & \dots & \Theta_{57} \\ \Theta_2 & & & \vdots \\ \vdots & & & \vdots \\ \Theta_8 & \dots & \dots & \Theta_{64} \end{bmatrix}, \quad B_{8 \times 4} = \begin{bmatrix} \Theta_{65} & \Theta_{73} & \dots & \Theta_{89} \\ \Theta_{66} & & & \vdots \\ \vdots & & & \vdots \\ \Theta_{72} & \dots & \dots & \Theta_{96} \end{bmatrix} \quad (2.49)$$

The state space model formulation from linearized equations of motion discussed in section 2.2 includes some terms dependent on the trim condition of the aircraft. The trim speeds u_0 , v_0 , w_0 and Euler angles θ_0 , ϕ_0 are known from the simulated data

(or flight test data for a real life application) and must be implemented to the model structure. When the dynamics for pitch angle θ and roll angle ϕ are examined, it is seen that they are not governed by any aerodynamic derivatives, meaning that the corresponding rows and columns in matrices A and B are defined. Using the state vector $\mathbf{x} = [u \ w \ q \ \theta \ v \ p \ \phi \ r]^T$ and control vector $\mathbf{u} = [\delta_{long} \ \delta_{lat} \ \delta_{coll} \ \delta_{ped}]^T$, the state and control matrices with known values and identification parameters are given in 2.50 and 2.51. This is also the model structure where all the aerodynamic derivatives in equations 2.7 and 2.8 are written as identification parameters.

$$A = \begin{bmatrix} \Theta_1 & \Theta_9 & \Theta_{17} & -g \cos \theta_0 & \Theta_{33} & \Theta_{41} & 0 & \Theta_{57} \\ \Theta_2 & \Theta_{10} & \Theta_{18} & -g \cos \phi_0 \sin \theta_0 & \Theta_{34} & \Theta_{42} & -g \sin \phi_0 \cos \theta_0 & \Theta_{58} \\ \Theta_3 & \Theta_{11} & \Theta_{19} & 0 & \Theta_{35} & \Theta_{43} & 0 & \Theta_{59} \\ 0 & 0 & \cos \phi_0 & 0 & 0 & 0 & 0 & -\sin \phi_0 \\ \Theta_5 & \Theta_{13} & \Theta_{21} & -g \sin \phi_0 \sin \theta_0 & \Theta_{37} & \Theta_{45} & g \cos \phi_0 \cos \theta_0 & \Theta_{61} \\ \Theta_6 & \Theta_{14} & \Theta_{22} & 0 & \Theta_{38} & \Theta_{46} & 0 & \Theta_{62} \\ 0 & 0 & \sin \phi_0 \tan \theta_0 & 0 & 0 & 1 & 0 & \cos \phi_0 \tan \theta_0 \\ \Theta_8 & \Theta_{16} & \Theta_{24} & 0 & \Theta_{40} & \Theta_{48} & 0 & \Theta_{64} \end{bmatrix} \quad (2.50)$$

$$B = \begin{bmatrix} \Theta_{65} & \Theta_{73} & \Theta_{81} & \Theta_{89} \\ \Theta_{66} & \Theta_{74} & \Theta_{82} & \Theta_{90} \\ \Theta_{67} & \Theta_{75} & \Theta_{83} & \Theta_{91} \\ 0 & 0 & 0 & 0 \\ \Theta_{69} & \Theta_{77} & \Theta_{85} & \Theta_{93} \\ \Theta_{70} & \Theta_{78} & \Theta_{86} & \Theta_{94} \\ 0 & 0 & 0 & 0 \\ \Theta_{72} & \Theta_{80} & \Theta_{88} & \Theta_{96} \end{bmatrix} \quad (2.51)$$

The model parameters left to be identified are the aerodynamic derivatives related to translational forces and moments on the aircraft. Even if Euler angle terms are eliminated from identification, the remaining parameters in a six degree of freedom model structure might still cause multiple solutions during identification. If the number of test maneuvers is large, then the scatter of converged parameter values can indicate the parameter accuracy. However, this is not the case for most applications, as the number

of repeat maneuvers are usually too small to achieve statistical accuracy [44]. Therefore, another systematic manner is needed to predict parameter accuracy. Cramer-Rao bounds and insensitivities are widely used in literature [5, 38] for this purpose. They provide mathematical basis for parameter accuracy using parameter standard deviation. Cramer-Rao bounds are defined as the minimum standard deviation σ_i for each parameter estimate Θ_i obtained from multiple flight test maneuvers [44].

$$\sigma_i \geq \text{CR}_i \quad (2.52)$$

These bounds can be constructed using the Hessian matrix as:

$$\text{CR}_i = \sqrt{(\mathcal{F}^{-1})_{ii}} \quad (2.53)$$

Where the Hessian matrix (also denoted as \mathcal{H} in reference [44]) reflects the curvature of the cost function to changes in parameters Θ . If a variation in one of the parameters do not cause a significant change in the cost function, then the Cramer-Rao bounds for that parameter is expected to be large. On the other hand, if the cost function is sensitive to variations in a parameter, the Cramer-Rao bounds would be small. Since large Cramer-Rao bounds imply insensitivity of cost function for those parameters, they should be excluded from the identification or be fixed [44]. Instead of directly using the Cramer-Rao bounds calculated by equation 2.53, the calculated values are divided by the parameter values to obtain percentages.

$$\overline{\text{CR}}_i = \left| \frac{\text{CR}_i}{\Theta_i} \right| \times 100\%. \quad (2.54)$$

Insensitivity of a parameter I_i indicates how insensitive the cost function is to changes in that parameter Θ_i . High insensitivity for a converged parameter indicates that the parameter is unimportant in the model structure. Insensitivity is calculated as:

$$I_i = \frac{1}{\sqrt{\mathcal{F}_{ii}}} \quad (2.55)$$

Similarly, insensitivities are normalized using the converged model parameters.

$$\bar{I}_i = \left| \frac{I_i}{\Theta_i} \right| \times 100\% \quad (2.56)$$

The Cramer-Rao bounds and insensitivities are related to each other. The geometric relation between the two is explained in [22] and shown that the Cramer-Rao bounds construct the upper limit for insensitivities.

$$\bar{I}_i \leq \overline{\text{CR}}_i \quad (2.57)$$

A systematic approach to model structure determination is presented in [44]. First, the unknown system parameters are initialized, and the model structure is converged to a solution using the optimization algorithm while all model parameters are present. The insensitivities for each of the parameters are calculated and normalized using equations 2.55 and 2.56. The parameter with the largest insensitivity is then dropped (equated to zero) from the model structure. To repeat this procedure, the remaining parameters are again initialized, and the optimization is run until convergence. With the obtained Hessian matrix, insensitivities are calculated again and the parameter with the greatest insensitivity is removed from the model. This procedure is repeated until all remaining parameters obey the guideline of $\bar{I}_i \leq 10\%$. After all insensitive parameters are dropped, Cramer-Rao bounds are examined. At this point, all parameters in the model structure important, as the cost function is sensitive to all of them. However, large Cramer-Rao bounds indicate correlation between parameters. With the remaining parameters, the algorithm is initiated again and the parameter with the largest Cramer-Rao bound is dropped from the model. The procedure is repeated until all parameters agree with the guideline $\overline{\text{CR}}_i \leq 20\%$. When there is no parameter to drop according to guidelines, the process is terminated. Throughout the iteration, the converged cost after each parameter drop should be monitored. If dropping a parameter results in a significant increase in the cost, then the procedure is terminated. Since the number of parameters in the model structure is reduced by the end of the whole process, it can also be referred as model reduction.

The model reduction routine aims to avoid multiple solutions in the state space representation during optimization and acquire a minimal representation of the dynamic

system. With the minimal representation, the important derivatives left in the model structure converge closer to their actual values. Since one of the main goals in flight vehicle system identification is accurate estimation of the key aerodynamic derivatives, model reduction procedures are essential. Even though this Hessian based approach provides a systematic procedure, it does not guarantee the uniqueness of the obtained model structure. The parameters are dropped from the model structure one by one, and not introduced to the model structure later. Since the solutions obtained with the output error algorithm in state space representation are not unique, the obtained final model structure is also not unique. A solution to this issue is proposed in [13] with the employment of adaptive learning algorithm for model structure determination. Adaptive learning provides unique optimal solutions with guaranteed convergence, independent of the initial parameter guesses. Results with the Hessian based model reduction routine and model structure determination with adaptive learning algorithm are both examined in Chapter 3.

By using a systematic approach to determine the model structure, one can eliminate the problem of existence of multiple solutions in state space model identification. Eliminating the least important derivatives from the model, a minimal representation of the system is achieved. The remaining derivatives are crucial for identification and since the model is reduced to a minimal form, the accuracy of their converged values is increased.

2.5 Validation of the Identified System

The system identification procedure examined in this work can be adopted to fit a mathematical model to a truth model data. The obtained model produces the best fitting outputs to the truth model measurements when the same inputs are being used. In order to validate the final product model, the identification results must be verified. Although validation in frequency domain is of greater importance since the identification is done in time domain, model accuracy is also checked using a time domain error criteria. A root mean square error (RMSE) is defined to verify the model outputs in time domain [44].

$$\text{RMSE} = \sqrt{\left(\frac{1}{N \cdot n_o}\right) \sum_{i=1}^N [(z - y)^T (z - y)]} \quad (2.58)$$

Where z are the truth model (or flight test) measurements to be used in validation, y are the simulated model outputs, N is the total number of data points in signals and n_o is the number of state signals in each test. The presented formulation offers a measure to examine if the time domain errors between simulated and measured signals are acceptable or not. For fixed-wing aircraft identification, the guideline for acceptable model accuracy is [44]:

$$\text{RMSE} \leq 0.5 \text{ to } 1.0 \quad (2.59)$$

For helicopters, due to largely coupled longitudinal and lateral dynamics, the adequate error values are larger than fixed-wing models as:

$$\text{RMSE} \leq 1.0 \text{ to } 2.0 \quad (2.60)$$

The guidelines given in 2.59 and 2.60 can be used to make sure the identified model has good accuracy in time domain. In the literature, however, it is common practice to verify the results in time domain if the identification is done in frequency domain and vice versa. Since the focus of this work is time domain identification, the results are verified in frequency domain. For this purpose, frequency sweep type maneuvers are need to be simulated with the identified model and the outputs must be converted to frequency domain. As discussed, frequency sweep inputs are sine wave like signals with increasing frequency throughout the maneuver. Tischler [44] presents a formulation for this type of input signal. The input signal is expressed as:

$$\delta_{\text{sweep}} = A_m \sin[\theta(t)] \quad (2.61)$$

with

$$\theta(t) \equiv \int_0^{T_{\text{rec}}} \omega(t) dt \quad (2.62)$$

The term A_m in equation 2.61 is the input amplitude, taken as 1. The frequency of the oscillations vary with the following expression:

$$\omega = \omega_{\min} + K (\omega_{\max} - \omega_{\min}) \quad (2.63)$$

Where $\omega_{\min} = 0.3rad/s$, $\omega_{\max} = 12.0rad/s$ and K is calculated from:

$$K = C_2 [\exp (C_1 t / T_{\text{rec}}) - 1] \quad (2.64)$$

with $C_1 = 4.0$ and $C_2 = 0.0187$ as suggested in [44].

2.5.1 Transformation of Time Domain Signals to Frequency Domain

The validation of the identified mathematical model in frequency domain requires transformation of time domain signals to frequency domain. In other words, frequency response functions between input-output pairs must be calculated. As discussed in the previous sections, it is of better practice to use dissimilar test maneuvers for verification than the ones used for identification. Furthermore, since frequency sweep maneuvers cover a greater frequency bandwidth compared to multistep input types, these types of maneuvers are better suited for frequency domain analyses.

Frequency sweep type inputs excite the system with a sine wave like oscillation in one channel where the frequency is gradually increased starting from lower frequency to higher frequency. In figure 2.8, the model response to a frequency sweep type input given to the longitudinal channel of the truth model in 70 knots forward flight is shown. The input signals are the delta values from the trim condition and the raw input signal in the longitudinal cyclic channel without controller interference is also provided with the input signals modified by the controller.

The frequency sweep type test maneuvers are more lengthy than the multistep input tests. In order to avoid deviation far from the trim condition, the same low frequency controllers are used during simulations with the truth model and the identified model. Now that the time domain input and output signal pairs for both truth model and

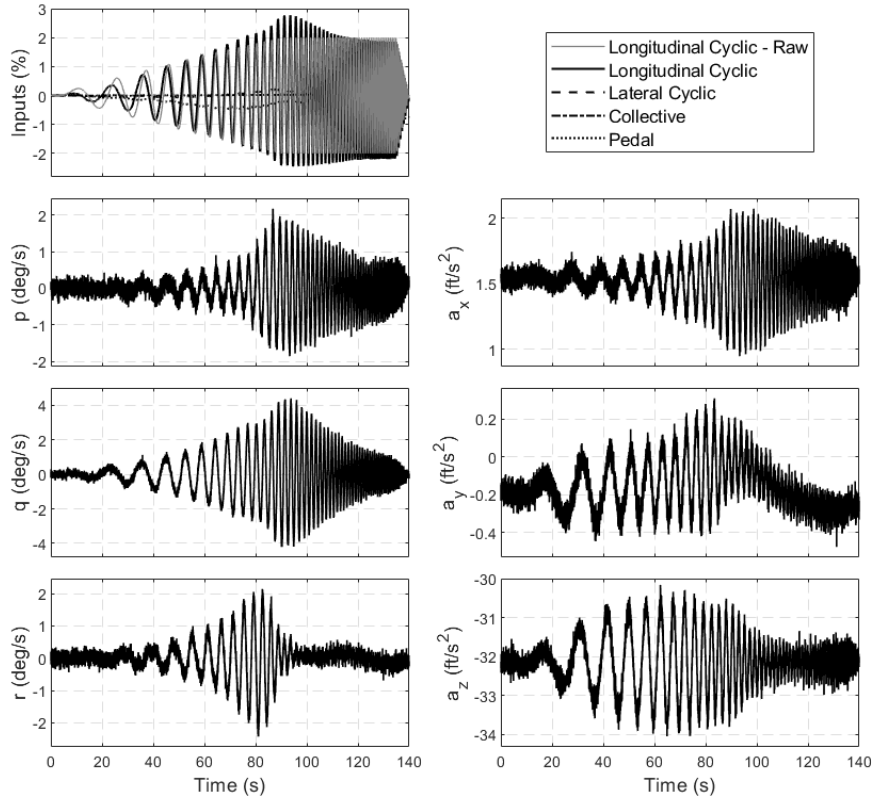


Figure 2.8: Frequency sweep type input given to longitudinal cyclic channel of truth model and its response in forward flight

identified model are generated, the obtained signals must be converted to frequency domain. For this purpose, Fourier transform is applied to input-output signal pairs. Fourier transform is used to decompose time based signals which can be periodic or non-periodic into their frequency components. The integral governing the Fourier transform for the input signal $x(t)$ is expressed as:

$$X(f) = \int_{-\infty}^{\infty} x(t)e^{-j2\pi ft} dt \quad (2.65)$$

Similarly, for output signal $y(t)$:

$$Y(f) = \int_{-\infty}^{\infty} y(t)e^{-j2\pi ft} dt \quad (2.66)$$

The frequency based signals $X(f)$ and $Y(f)$ are the Fourier coefficients. The frequency response function $H(f)$ can be written as:

$$H(f) = \frac{Y(f)}{X(f)} \quad (2.67)$$

Once the frequency response function is calculated, magnitude and phase information can be acquired. However, the expressions 2.65 and 2.66 are not practical since the time based signal does not extend from $-\infty$ to $+\infty$ in applications. Considering a test maneuver recorded for a finite time interval, the appropriate transformation method for continuous time based signals is finite Fourier transform.

$$X(f, T) = \int_0^T x(t) e^{-j2\pi ft} dt \quad (2.68)$$

It is also known that the data sampled during flight tests or truth model simulations is not continuous, but discrete. For discrete signals with constant sampling time, the discrete Fourier transform (DFT) is used.

$$X(f_k) = X(k\Delta f) = \Delta t \sum_{n=0}^{N-1} a_n \exp \left[-\frac{j2\pi(kn)}{N} \right] \quad (2.69)$$

Again, $X(f)$ are the Fourier coefficients at each frequency f_k . The number of discrete frequencies is the same as the number of discrete time points in the time based signal. Therefore, the index k is defined such that $k = 0, 1, 2, \dots, N - 1$. Δf is the frequency resolution ($\Delta f = 1/N\Delta t$) which is also the minimum frequency point. The discrete frequency points are distributed from $f_{min} = 1/N\Delta t$ to sampling rate $f_s = 1/\Delta t$. The selection of discrete frequencies is given as shown in equation 2.70 [4]. Finally, a_n is the time based recorded signal with $n = 0, 1, 2, \dots, N - 1$.

$$f_k = \frac{k}{N\Delta t} \quad k = 0, 1, 2, \dots, N - 1 \quad (2.70)$$

To calculate the frequency response function H , autospectral (also referred to as power spectral) density functions are needed. These functions represent the change of the mean square of the time based signal with respect to frequency. Following the notation used by Bendat and Piersol [4], the rough estimates of the input and output autospectral density functions and input-output cross spectral density function are

calculated as:

$$\tilde{G}_{xx}(f) = \frac{2}{T}|X(f)|^2 \quad (2.71)$$

$$\tilde{G}_{yy}(f) = \frac{2}{T}|Y(f)|^2 \quad (2.72)$$

$$\tilde{G}_{xy}(f) = \frac{2}{T}[X^*(f)Y(f)] \quad (2.73)$$

Where T is the length of a test record and $*$ indicates complex conjugate.

2.5.2 Windowing

The estimates of spectral functions are prone to have errors due to noisy measurements of input and output signals. During real life flight testing, the external disturbances from atmospheric conditions also contribute to these errors. There are methods that can be applied to reduce the errors in spectral function estimates. An averaging procedure is proposed in [4] to improve the quality of the estimates. A recorded data of length T_r is divided into multiple shorter time segments, where each segment has the same length T . The discrete Fourier transform given in equation 2.69 is applied to each of these segments and spectral functions are evaluated separately. The average of these spectral functions is taken to obtain the final (smooth) estimates.

Even though the method of averaging improves the estimates of spectral functions, the obtained signals in frequency domain still suffer from side lobe leakage if the signal is non-periodic. The Fourier transform requires the time domain signal to be periodic by its nature. If the time based signal does not have an integer number of cycles at the time span of interest, leakage will occur during transformation to frequency domain. Fourier transformation is a tool to understand the dominant frequency content in a time based signal. If the estimations of frequency based signals are corrupted with leakage, frequency content that is not present in the time signal would appear. Since test recordings are non-periodic most of the time, leakages in frequency domain es-

timates are unavoidable. In order to diminish the corruption of data with side lobe leakage, time history windowing (or tapering) is utilized.

As discussed, the side lobe leakage occurs due to discontinuities in time history data. Windowing can be thought of as multiplying the time intervals with a window gain to reduce the discontinuities between these intervals. The aforementioned approach of averaging the rough spectral estimates from multiple time segments directly uses the time signals. It can be also said that the time section of interest is multiplied by one and the else by zero, which is essentially the Boxcar (or rectangular) window. This window can be expressed as:

$$u_b(t) = \begin{cases} 1 & 0 \leq t \leq T \\ 0 & \text{otherwise} \end{cases} \quad (2.74)$$

Where $u_b(t)$ is the window function. Figure 2.9 shows the Boxcar window for a time based signal from 0 to T .

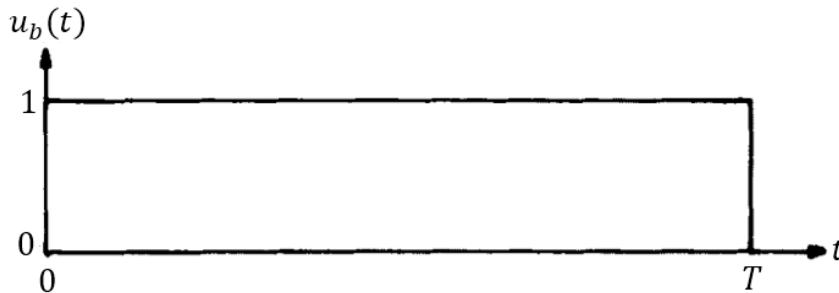


Figure 2.9: Boxcar (rectangular) window in time domain [4]

$U_b(f)$ is the Fourier transform of the window function given in 2.74. $U_b(f)$ is plotted with respect to frequency in figure 2.10. The side lobe leakage can be clearly seen as the frequency content away from the main lobe is distorted. In this type of window, the difference between the main lobe and the first side lobes is 13dB and 6dB thereafter [4].

A window function is introduced to reduce the corruption due to side lobe leakage. The most common window type that is used in flight vehicle system identification studied is Hanning window, which has $(1 - \cos)$ shape [4, 44]. The Hanning window

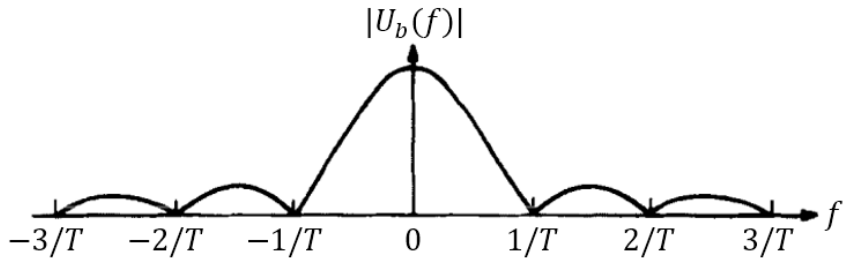


Figure 2.10: Boxcar (rectangular) window in frequency domain [4]

function $u_h(t)$ is expressed as:

$$u_h(t) = \begin{cases} \frac{1}{2} (1 - \cos \frac{2\pi t}{T}) = 1 - \cos^2 (\frac{\pi t}{T}) & 0 \leq t \leq T \\ 0 & \text{otherwise} \end{cases} \quad (2.75)$$

The shape of the Hanning window is presented in figure 2.11

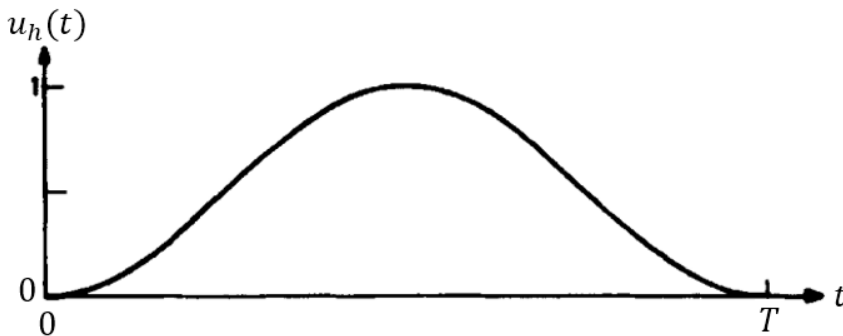


Figure 2.11: Hanning window in time domain [4]

Instead of a constant window gain throughout the time interval, Hanning window starts and ends at zero. By multiplying the time signal with Hanning window function, seamless transition between time intervals is achieved. The Fourier transform $U_h(f)$ of the Hanning window function is plotted in figure 2.12.

As one can see, the side lobe leakage is now significantly suppressed as the drop from the main lobe to the first side lobe is now 32dB and follows with 18dB. Implementing the Hanning window function into the DFT expression given in 2.69 results in:

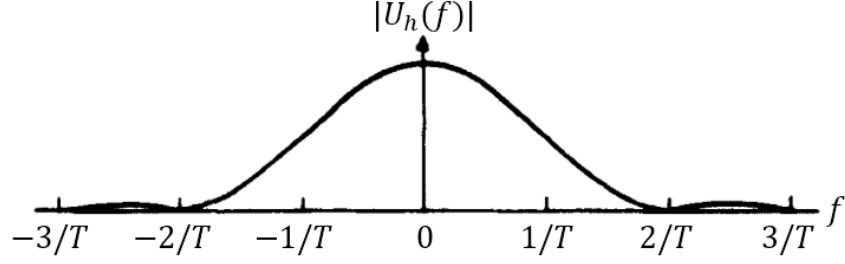


Figure 2.12: Hanning window in frequency domain [4]

$$X_i(f_k) = \Delta t \sqrt{\frac{8}{3}} \sum_{n=0}^{N-1} a_{in} \left(1 - \cos^2 \frac{\pi n}{N}\right) \exp \left[-\frac{j2\pi kn}{N} \right] \quad (2.76)$$

In equation 2.76, the subscript i is used to denote the window index. Using Hanning window in calculation of Fourier coefficients results in a loss in magnitude. To overcome this issue, a correction factor of $\sqrt{8/3}$ calculated from equation 2.77 is added.

$$\frac{\int_0^T u_h^2(t) dt}{\int_0^T u_b^2(t) dt} = \frac{3}{8} \quad (2.77)$$

The segments of the time based test signal can be selected such that they overlap each other. In fact, by using this approach of overlapped windowing, the quality of spectral estimates are improved. The number of windows n_d for a given test signal and the overlap ratio can be selected by a trial and error process. As a rule of thumb, 80% overlap is suggested by Tischler in [44]. Using this method of sectioning the test signal into smaller segments, the minimum frequency for DFT calculations is updated accordingly. The minimum frequency is governed by the window length, such that $f_{min} = 1/T_w$. For a time segment, there is no information about the frequency content for frequencies smaller than f_{min} . By increasing the window size, calculations in smaller frequencies can be done, however, the number of windows to be averaged decrease for the same overlap ratio [44].

For time history tapering, numerous window functions are available and any one of them can be adopted depending on the application. Reference [33] presents a detailed

discussion on these window functions and their properties. Hanning window is one of the most commonly used window functions in system identification studies, therefore it is also adopted for this work.

The rough estimates of spectral functions can be obtained for each windowed time segment using equations 2.71, 2.72 and 2.73. Averaging the rough estimates from each window, smooth estimates (denoted with $\hat{\cdot}$) are obtained.

$$\hat{G}_{xx}(f) = \left(\frac{1}{n_d}\right) \sum_{k=1}^{n_d} \tilde{G}_{xx,k}(f) \quad (2.78)$$

$$\hat{G}_{yy}(f) = \left(\frac{1}{n_d}\right) \sum_{k=1}^{n_d} \tilde{G}_{yy,k}(f) \quad (2.79)$$

$$\hat{G}_{xy}(f) = \left(\frac{1}{n_d}\right) \sum_{k=1}^{n_d} \tilde{G}_{xy,k}(f) \quad (2.80)$$

The smooth estimates of autospectral density function of input and output signals and their cross power spectral density are used to obtain the frequency response function H from 2.81.

$$\hat{H}_1(f) = \frac{\hat{G}_{xy}(f)}{\hat{G}_{xx}(f)} \quad (2.81)$$

An alternative expression is presented in [44] as:

$$\hat{H}_2(f) = \frac{\hat{G}_{yy}(f)}{\hat{G}_{yx}(f)} \quad (2.82)$$

Both of these expressions essentially produce the same result when input and output measurements are not corrupted by noise. It is stated in [44] that when output measurements are noisy, but the input measurements are noise free, the expression 2.81 should be adopted. Since this is the case for this study, the frequency response function is calculated using 2.81. The alternative expression given in 2.82 should be used in certain situations where the output signal can be considered noise free and noise is present in the input signal measurements.

For the visualization of the frequency response function, Bode plots are utilized. Bode plots display the magnitude and phase content with respect to frequency in semilogarithmic plots. The adopted units for magnitude, phase, and frequency are decibels, degrees, and radians per second respectively. The magnitude and phase of the frequency response function can be found as:

$$H_{dB} = 20 \log_{10} |H(j\omega)| \quad (2.83)$$

$$H_{deg} = \angle H(j\omega) \text{ deg} \quad (2.84)$$

2.5.3 Coherence Function

By plotting the magnitude and phase information, the relations between each input and output signal pair can be examined throughout the frequency range that DFT is calculated. However, the input output relation for the whole frequency bandwidth is not of interest. To determine the appropriate frequency interval, the coherence function is used.

$$\hat{\gamma}_{xy}^2(f) = \frac{|\hat{G}_{xy}(f)|^2}{|\hat{G}_{xx}(f)| |\hat{G}_{yy}(f)|} \quad (2.85)$$

Coherence function indicates linear relation between the input and output spectrums. It takes values between 0 and 1 and the value of 1 implies perfect linear relation between input and output. Due to the presence of noise in measurements and process, the coherence function does not take the value of 1 in practice. In system identification studies, the guideline for the adequate frequency range is indicated by the frequencies where $\hat{\gamma}_{xy}(f) \geq 0.6$ and not oscillating.

2.5.4 Validation Criteria

Up to this point, the discussion on this chapter focuses on transformation from time domain to frequency domain with high accuracy. The time domain input output signal pairs can be converted to frequency domain using DFT with windowing and by using equations 2.83 and 2.84, the Bode plots can be generated. By following this procedure for input output pairs from both simulations of the identified model and truth model signals, a comparison in frequency domain can be made. For this purpose, an error function is defined as [44]:

$$\varepsilon(f) \equiv \frac{H_{sim}(f)}{H_{flight}(f)} \quad (2.86)$$

Applying equations 2.83 and 2.84 to the error function given in 2.86, the magnitude and phase characteristics of the error between the truth model and the identified model can be acquired. These magnitude and phase errors compared with error bounds of maximum unnoticeable added dynamics (MUAD) and allowable error envelopes (AEE). The zero value for both magnitude and phase signals of the error function indicates perfect model fit to the truth model data. Therefore, both boundaries are constructed around the zero value as shown in figure 2.13.

The boundaries of MUAD are constructed such that beyond these bounds, a pilot would notice the difference between the simulation model and the actual aircraft. The error tolerances become narrower around the usual pilot operating regime, which is mid-frequencies [30]. Therefore, the most important section of these bounds for flight vehicle identification can be considered to be between 1rad/s and 10rad/s. For smaller or larger frequencies, pilot sensitivity decreases, as can be seen from figure 2.13. These criteria of model validation is proposed to be used as Level D model fidelity criteria by Tischler [45] and used for identified model validation in references [9, 13, 30, 47].

Along with MUAD bounds, another validation criteria proposed by Mitchell et al. [27] known as allowable error envelopes (AEE). Figure 2.13 also shows AEE boundaries on a semilogarithmic plot. Even though these bounds look similar to MUAD boundaries, they both established with different criteria. AEE bounds are constructed

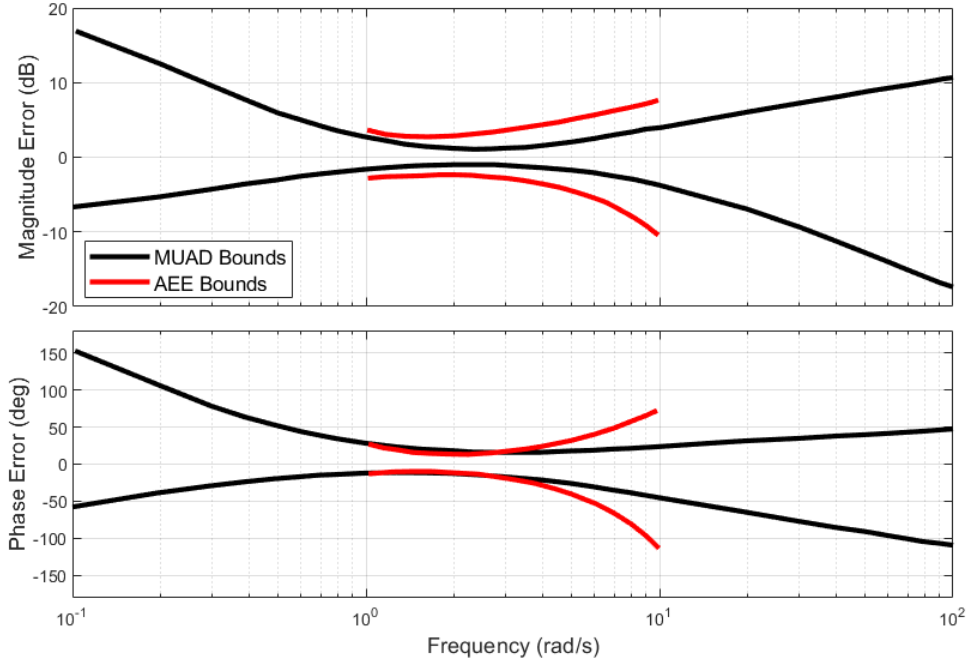


Figure 2.13: Boundaries of maximum unnoticeable added dynamics (MUAD) [16] and allowable error envelopes (AEE) [27]

using pilot opinion on task performance, whereas the MUAD bounds are constructed according to handling quality [30].

The MUAD and AEE bounds constitute the validation criteria for the identified mathematical model. The validation procedure can be summarized as follows. The model and the truth model are simulated with dissimilar inputs compared to identification maneuver set. Appropriate window size and number of windows are selected for windowing. The input output signal pairs for both simulation and truth models are transformed to frequency domain using DFT with windowing given in equation 2.76. Rough spectral function estimates are obtained from equations 2.71, 2.72 and 2.73. The rough spectral estimates for each window are averaged to calculate smooth estimates. The frequency response functions are calculated using equation 2.81. The error function is calculated from 2.86 and its magnitude and phase information are obtained by applying equations 2.83 and 2.84. The coherence function is calculated using equation 2.85. Considering the guideline for coherence and by evaluating the magnitude and phase errors according to MUAD and AEE bounds, the model fidelity is examined.

CHAPTER 3

IMPLEMENTATION AND RESULTS

The theory and procedure discussed in Chapter 2 are implemented to identify the dynamics of a helicopter in two flight conditions. The identification is carried out in two cases. In the first one, no prior knowledge of the model structure or initial values of the parameters are available, and the model structure is established via Hessian based model reduction approach. In the second case, the model structure determination is carried out using adaptive learning [13] along with an estimation for the initial values for the parameters. For both trim conditions, the time domain comparisons between the identified model without time delays, the identified model with time delays and the truth model are presented for 3211 and 2311 type input tests. Only the tests starting in the positive input direction are shown in this section for simplicity, however, the rest of the identification maneuvers are presented in Appendix A.

Along with time domain comparison, the frequency response comparisons of the aforementioned models are illustrated in bode plots obtained from discrete Fourier transform to frequency sweep maneuvers. Since bode plots can be drawn for any input output pair, only the most important pairs for each input signal are shown. For longitudinal cyclic maneuvers p/δ_{long} and q/δ_{long} , for lateral cyclic maneuvers p/δ_{lat} and q/δ_{lat} , for collective maneuvers r/δ_{coll} and a_z/δ_{coll} , for pedal maneuvers r/δ_{ped} and a_y/δ_{ped} are plotted.

Finally, the magnitude and phase errors of the identified systems are shown along with the coherence functions. The errors in cyclic maneuvers are compared with MUAD and AEE bounds, and the errors in collective and pedal maneuvers are compared with MUAD bounds only.

3.1 Identification with Hessian Based Model Reduction

In this section, the system identification results with the Hessian based model reduction approach and no initial parameter guesses are presented. The identification is carried out for two trim conditions, namely hover and 70 knots forward flight. The model reduction procedure discussed in Chapter 2 is applied for both trim conditions, and time delays are added to the model structures as necessary.

The first step of flight vehicle system identification is data gathering through flight tests. Data gathering is a crucial step that has a direct impact on the identification results. The flight test campaign must be designed with care to obtain data with adequate quality. For this purpose, the goal of system identification must be determined. In this study, the aim is to develop a system identification software which can obtain simple mathematical models for two different flight conditions of a helicopter. The flight conditions are determined to be hover and forward flight with 70 knots speed at sea level, where the helicopter exhibits distinct flight characteristics. The test maneuvers must be designed such that the dynamic modes of the aircraft are excited. If the maneuver data do not contain any information regarding these modes, they cannot be identified [18]. The types of maneuvers are also related to the domain at which the identification will be carried out. Frequency sweep type inputs cover a greater frequency bandwidth compared to multistep inputs and well suited for identification in frequency domain identification. For time domain identification, frequency sweep inputs are not preferred as they are lengthy and can result in divergence of the algorithm. Since this work focuses on time domain identification using output error algorithm, 3211 and 2311 type maneuvers are utilized for identification. However, frequency sweep type maneuvers are still used to verify the identified system.

The truth model used in this work is developed by Aerotim Engineering [1] and certified by EASA as a Level D flight simulation model. At the two flight conditions (hover and 70 knots forward flight), the aircraft is trimmed and starting from these trim conditions, test maneuvers are executed. The list of simulation maneuvers recorded at these two trim conditions can be seen in table 3.1. In order to avoid model deviation far from the initial trim condition, lower frequency controllers are employed. The generated truth model test data are then corrupted by artificial mea-

Table 3.1: List of maneuvers at each trim condition

	Hover	Forward Flight
3211 in both directions in all channels	8	8
2311 in both directions in all channels	8	8
Frequency Sweep in all channels	4	4

surement noise to mimic a real life flight test scenario. The recorded signals are translational velocities u, v, w in ft/s , translational specific accelerations a_x, a_y, a_z in ft/s^2 , rotational accelerations p, q, r in deg/s and Euler angles ϕ, θ, ψ in deg .

Once the tests signals from the truth model are generated, the initial model structure is formulated. As stated in [18], a large, extensive mathematical model do not necessarily indicate the best description of the actual system. Adopting the principle of simplicity, the mathematical model of the helicopter is chosen to be the linearized set of equations of motion, as shown in set of equations 2.1. When written in matrix form, the differential equations are of form 2.2 and the measurement equation is given to be as 2.3. The state and control vectors \mathbf{x} and \mathbf{u} are as given in 2.4 and 2.5. The measurement vector \mathbf{y} is expressed as 2.6, since angular rates and specific accelerations are outputs of gyroscope and accelerometer.

The optimization method for system identification is output error algorithm, which is based on maximum likelihood parameter estimation principle. The formulation of the algorithm is presented in Chapter 2 along with the Levenberg-Marquardt algorithm and each step is developed through MATLAB environment. With this optimization algorithm, a system identification software is obtained which estimates the model parameters when the truth model signals are provided and the model structure is specified. The system and control matrices are specified as shown in equations 2.50 and 2.51, where system parameters Θ are the unknown values to be determined via identification. As this case assumes no prior knowledge of the system parameters are available, the initial values for the unknown parameters are taken to be zeros.

The output error algorithm discussed in this work is an iterative method. The number of iterations to achieve convergence depends on the number of unknown system pa-

Table 3.2: Trimmed state values at hover

Parameter	Value	Parameter	Value
u_0	0 ft/s	δ_{long_0}	66.18 %
v_0	0 ft/s	δ_{lat_0}	52.65 %
w_0	0 ft/s	δ_{coll_0}	64.13 %
ϕ_0	-2.87 deg	δ_{ped_0}	37.45 %
θ_0	6.76 deg	Total Mass	2800.0 kg

rameters, number of available maneuvers and the initial conditions of the parameters. At each loop, the system states are integrated for the number of maneuvers to calculate model responses. When integrated with the Levenberg-Marquardt algorithm, not only an inner loop is added to the algorithm, but this additional loop requires the model to be simulated two times per loop. The computational overhead becomes more expensive as the number of Levenberg-Marquardt loops and number of maneuvers increase. To overcome prolonged runtimes, parallel computing in MATLAB environment is utilized during system simulations.

3.1.1 Identification of Dynamics in Hover

The first flight condition to be identified is hover at sea level. The values of the aircraft states at this trim condition is listed in table 3.2. Note that the values in this table are representative, not the actual values. As can be seen from table 3.1, there are 8 of 3211 and 2311 maneuvers each for identification and 4 frequency sweeps at all channels for verification purposes. Therefore, a total of 16 maneuvers are fed to the constructed maximum likelihood output error algorithm for this flight condition.

As discussed in section 2.4, state space representations of systems are not unique and using a model structure shown in equations 2.50 and 2.51 results in redundant parameters. In order to avoid multiple solutions and parameter redundancy, the model reduction procedure discussed in 2.4 is applied. This model reduction approach follows a systematic manner to identify parameters that are of lesser importance. These

parameters are then equated to zero and dropped from the model structure. First, the model structure with all system parameters is converged to a solution. The Cramer-Rao bounds and insensitivities for each parameter are calculated using the Hessian matrix from equations 2.53 and 2.55. The parameter with the greatest insensitivity is then dropped according to the guidelines discussed in section 2.4. This procedure is followed until all model parameters are dropped, to examine the fitting error after each parameter drop. The error function is the root mean square error, formulated as shown in equation 2.58. The guideline for an adequate model for rotorcraft is $RMSE < 2$ for rotorcraft as given in [44]. Figure 3.1 presents the variation of the cost function with parameter drop.

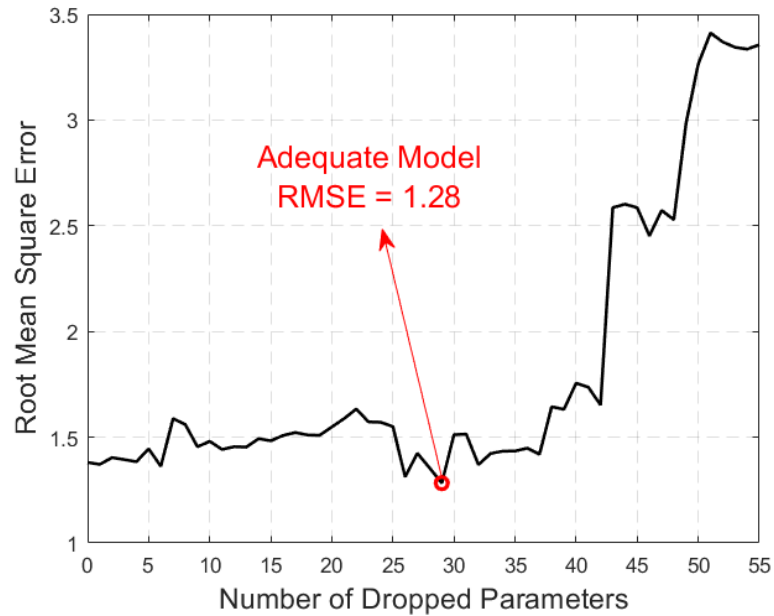


Figure 3.1: Variation of RMSE through model reduction in hover

As can be seen from figure 3.1, the cost function of the converged solution exhibits an oscillating behavior until 44th parameter drop and after that a jump is observed. For hover condition, the lowest cost is acquired with a model with 29 parameters dropped from the model structure. This solution has a RMSE value of 1.28, which is well below the recommended guideline value of 2. In this model structure, the dropped aerodynamic parameters from the model structure are $X_v, X_w, X_r, X_{lat}, X_{coll}, Y_p, Y_q, Y_u, Y_w, Y_{long}, Y_{lat}, Y_{coll}, Y_{ped}, Z_u, Z_v, Z_p, Z_q, Z_{long}, Z_{lat}, Z_{ped}, L_w, L_{coll}, L_{ped}, M_v, M_w, M_{coll}, M_{ped}, N_u$ and N_{long} . The order that these derivatives are removed

from the model along with their values, insensitivities and Cramer-Rao bounds are presented in Appendix B.

With the determined model structure, the converged identification result is examined. Figure 3.2 shows the variation of parameter values during optimization. It can be seen that all parameters are converged successfully.

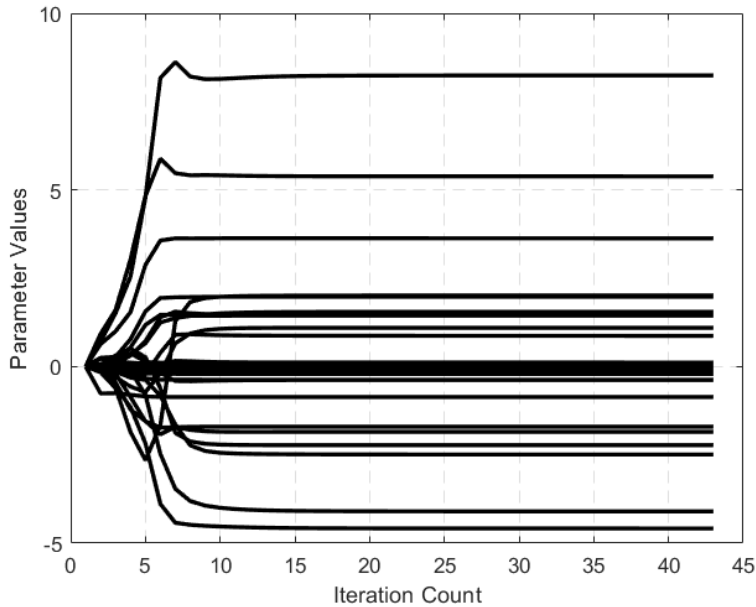


Figure 3.2: Iteration history of parameters for identification in hover

3.1.1.1 Results for Longitudinal Cyclic Input

Identification results to longitudinal cyclic inputs are examined first. Figure 3.3 illustrates the identified model response along with truth model signals for 2311 type input in positive direction in longitudinal cyclic channel. As can be seen from the figure, the on axis pitch and the specific acceleration in body x direction responses of the identified model shows good agreement with the outputs of the truth model. The yaw rate response and the specific accelerations in body y and z directions deviate from truth model signals, however, the magnitude of the excitements are also small. When the off axis roll response is compared, it can be noticed that the truth model response lags behind the identified system. This issue is also seen in the lateral cyclic tests, however, only longitudinal cyclic tests are shown here explicitly for simplicity.

To determine whether this delay in the actual system is acceptable or not, the model validation procedure in frequency domain discussed in section 2.5 is followed. The frequency sweep input that is used to generate truth model data are fed to the identified system. For the input output pairs for each state, frequency response functions are calculated using Fourier transformation. Bode plots for each input and output pair can be drawn individually, however, for the sake of simplicity only the important pairs are shown here as it is the usual practice in literature. For frequency sweep in longitudinal cyclic channel, q/δ_{long} and p/δ_{long} pairs are shown in figure 3.4

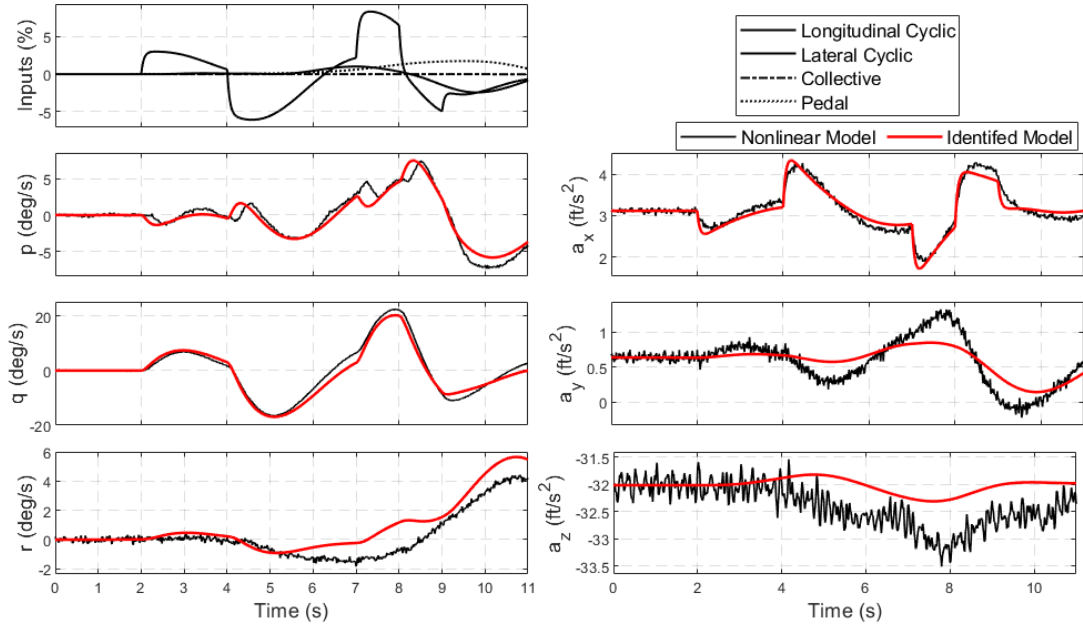


Figure 3.3: Time domain identification results for longitudinal cyclic 2311 input in positive direction during hover

The figures illustrate that the magnitude signals between the truth model and the identified model show good agreement, but the error between the phase signals grow as frequency increases. In figure 3.5, the magnitude and phase errors are compared with MUAD and AEE bounds. The figure also shows the coherence function of the related input output pairs.

The frequency range where good identification results are desired are obtained following the guidelines in [44]. It is stated that the frequency bandwidth of interest is where the coherence function is greater than 0.6 and not oscillating. For p/δ_{long} pair, there is a drop in the coherence function between 1-2 rad/s and after 9 rad/s.

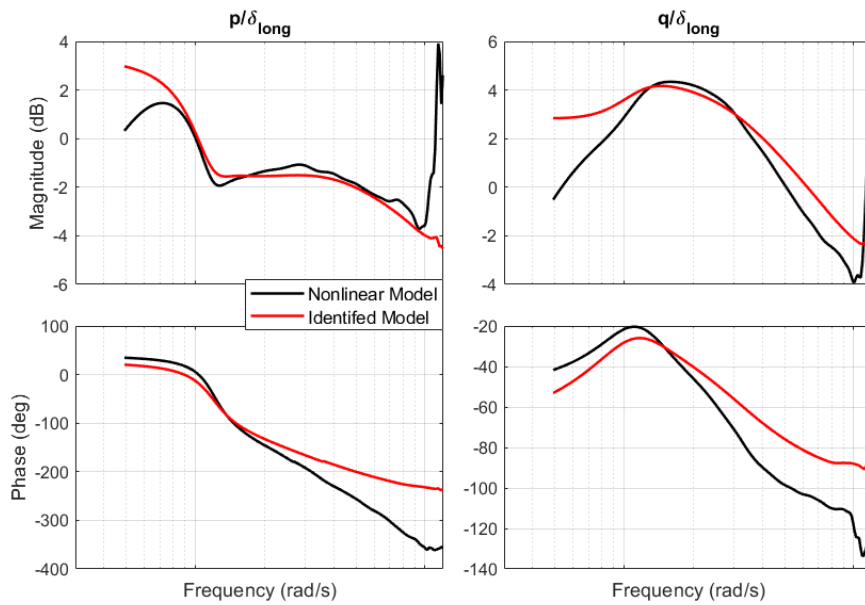


Figure 3.4: Bode plots of q/δ_{long} and p/δ_{long} pairs for frequency sweep in longitudinal cyclic in hover

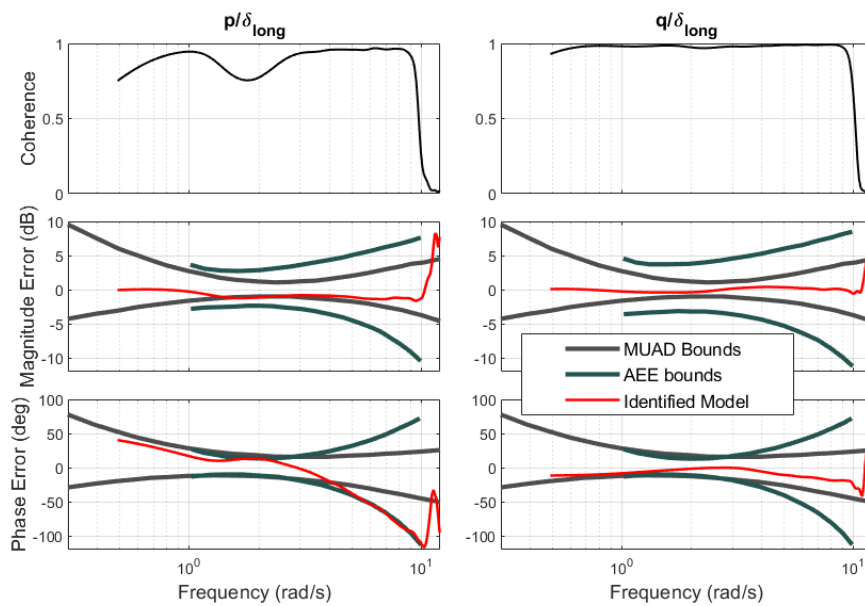


Figure 3.5: Coherence and Errors of q/δ_{long} and p/δ_{long} pairs for frequency sweep in longitudinal cyclic in hover

Therefore, the region of interest is between 2 rad/s to 9 rad/s. It can be said that the magnitude error stays within the error bounds throughout this frequency bandwidth. However, the phase error is outside of both MUAD and AEE bounds, hence, it is

not acceptable. For the on axis pair of q/δ_{long} , both magnitude and phase errors are acceptable.

With the model structure being used, the phase content present in the truth model data cannot be modelled with high accuracy. In order to overcome this problem, the reason of this behavior in off axis dynamics should be examined. As discussed in 2.2.1, the roll to pitch motion in helicopters is highly coupled due to the gyroscopic motion of the rotor. This effect can also be referred as the off axis coupling. Furthermore, the longitudinal and lateral cyclic controls require flapping to developed, meaning that the response of the rotor to controls is delayed. To account for such dynamics, time delays are employed in the model structure. When time delays are added to parameters in the control matrix, they represent delays between input-output pairs. However, time delays in the system matrix represent internal delays between the system states. In order to avoid unnecessary complications and inclusion of unnecessary parameters to the model structure, time delays are first added to the control derivatives of L_{long} , L_{lat} , M_{long} , M_{lat} . The time delays are implemented in the model structure such that the operations with the parameters with nonzero delay values are calculated separately during simulations of the model. These delay values are implemented as unknown parameters to be identified, where a saturation logic is implemented to prevent negative time delay values. With the obtained reduced model structure, the identification loop is initiated again. This time, the set of parameter values are used as initial conditions.

Figure 3.6 displays the iteration histories of the parameters starting from the initial values of the identification without time delays. It can be observed that convergence is achieved around 15 iterations. The values of the identified parameters are provided in Appendix C along with their relative insensitivity and Cramer-Rao percentages. To check the obtained parameter estimates, some important static stability derivatives are examined.

The static stability with the variation of angle of attack is examined with M_w derivative. When the angle of attack of the helicopter increases, the lift force generated by the rotor blades increase in both retreating and advancing sides. During hover, the lift increment in the two sides are similar on contrary to forward flight condition. As a result, the helicopter is neutrally stable and the value of M_w is around zero. In hover,

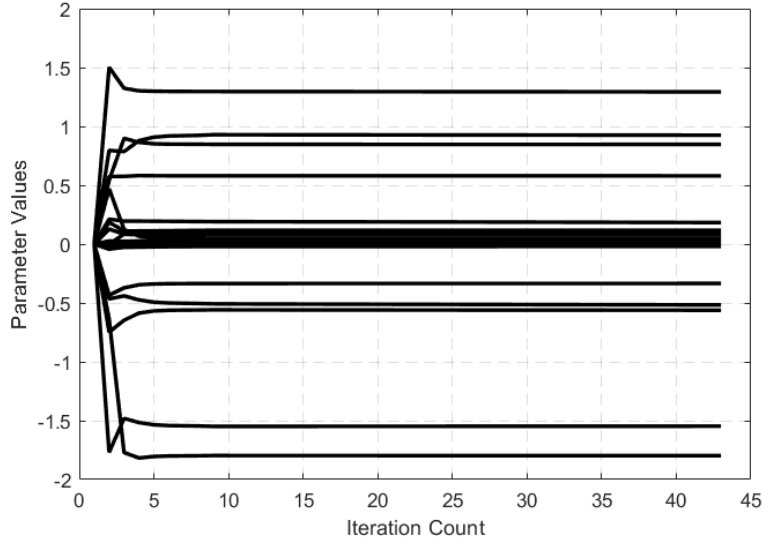


Figure 3.6: Iteration history of parameters for identification in hover with additional dynamics

it can be noticed that the derivative is dropped from the model structure due to high insensitivity. The dihedral effect is determined with L_v derivative. A stable dihedral effect indicates the tendency of the helicopter to create restoring rolling moment when sideslip angle changes. Helicopters have stabilizing dihedral effect, hence the sign of L_v is negative, as it is the case with the identification results. Helicopters also have directional (weathercock) stability due to the presence of tail rotor in hover, resulting in a positive N_v derivative. Finally, the heave stability is investigated with the sign of Z_w . As the vertical velocity increases, the main rotor experiences greater angle of attack and the thrust increases. Therefore, the sign of Z_w is negative for helicopters. By looking at the results in Appendix C, it can be seen that the identification results agree with the rotorcraft dynamics. The magnitudes and signs of other derivatives such as M_u , X_u , X_v , Y_u and Y_v are also checked and verified with reference [31], where a more extensive discussion on stability and control derivatives of helicopters can be found.

Figures 3.7, 3.8 and 3.9 show the identification results in time and frequency domains. The roll axis response in figure 3.7 exhibits the lag due to additional dynamics, similar to the truth model response. Furthermore, when the frequency responses in figure 3.9 are examined, it can be seen that the phase response of p/δ_{long} shows a similar

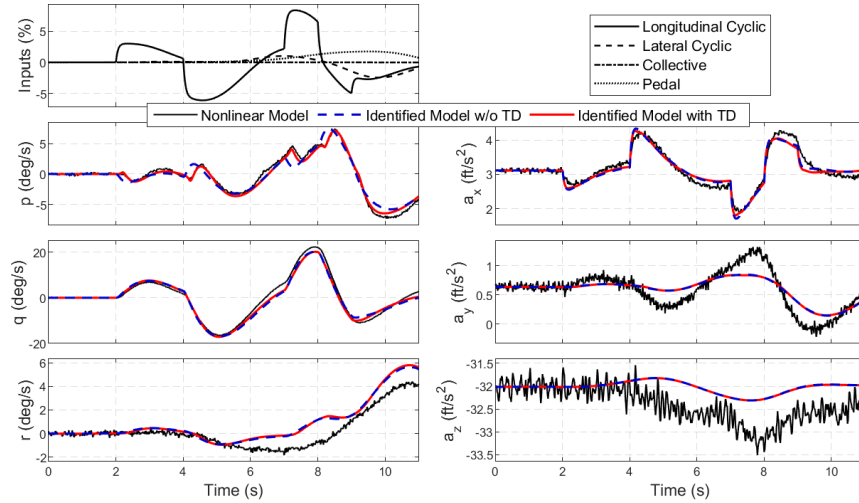


Figure 3.7: Time domain identification results for longitudinal cyclic 2311 input in positive direction during hover

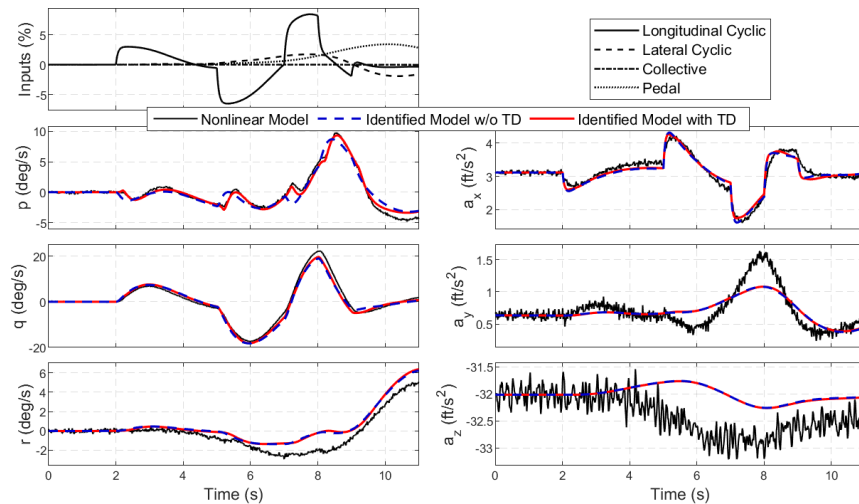


Figure 3.8: Time domain identification results for longitudinal cyclic 3211 input in positive direction during hover

behavior as the truth model. Finally, to validate the obtained results, the magnitude and phase errors are plotted along with MUAD and AEE bounds in figure 3.10. The addition of time delays to the model structure do not result in a significant change that a pilot can notice in q/δ_{long} response. However, the phase error in p/δ_{long} pair is reduced significantly. The magnitude and phase errors of the system with time delays are now satisfactory in the frequency bandwidth of acceptable coherence. As mentioned before, maneuvers where the inputs start in the negative input direction are

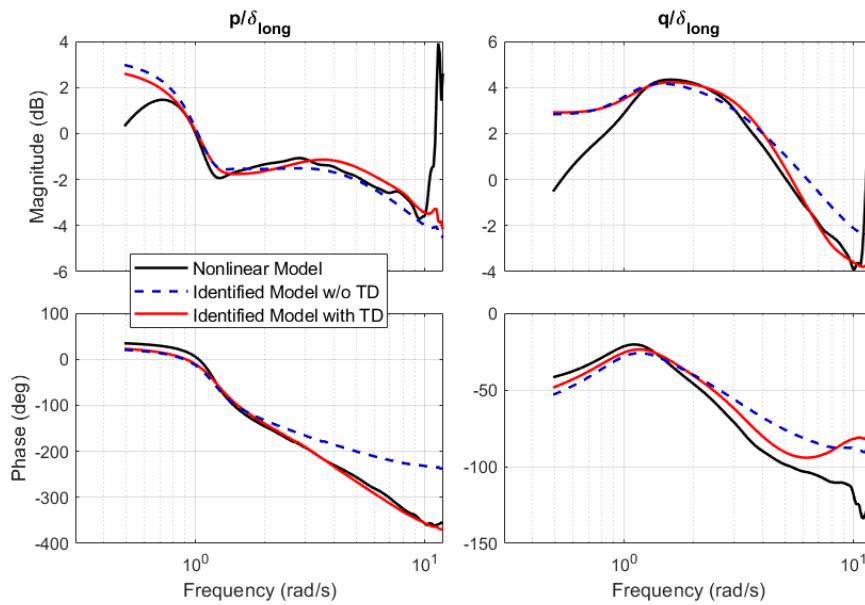


Figure 3.9: Frequency domain comparison of q/δ_{long} and p/δ_{long} input output pairs in longitudinal cyclic frequency sweep maneuver in hover

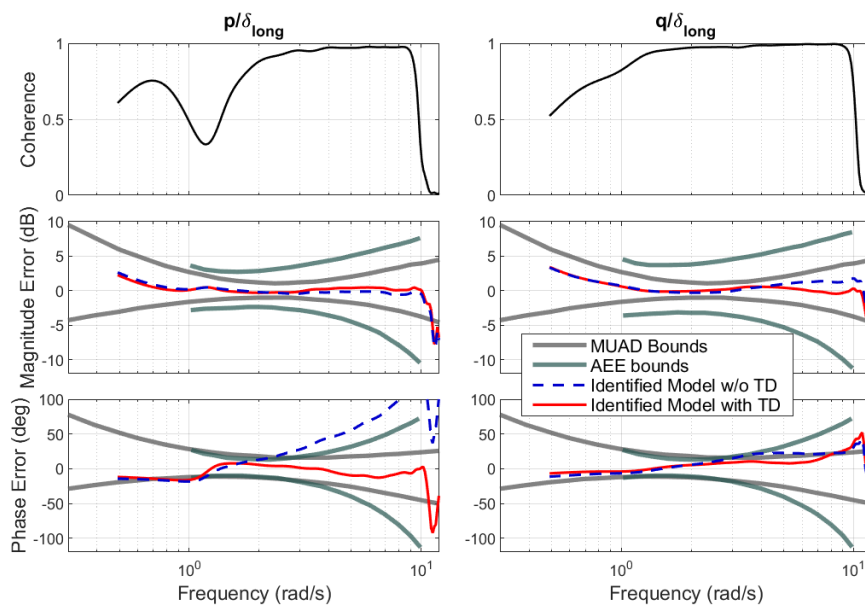


Figure 3.10: q/δ_{long} and p/δ_{long} input output pairs and error bounds in longitudinal cyclic frequency sweep maneuver in hover

presented in Appendix A.

3.1.1.2 Results for Lateral Cyclic Input

The second input channel that the identification results are examined is lateral cyclic. 3211 and 2311 maneuvers are used for optimization, and only the inputs starting in the positive direction are presented in this section. The rest of the maneuvers can be found in Appendix A. The time domain comparisons of the results given in figures 3.11 and 3.12 are examined first. It can be observed that pitch and roll channels exhibit greater excitation compared to the yaw channel, as expected. The on axis roll response of the identified model shows good agreement with the truth model. When the off axis pitch response is compared, it can be said that the overall trend of the response is similar to the one of truth model. However, the dynamics due to rotor are still present in the data from the truth model and not captured by the identified model without time delays. The error between the models is more clear in figure 3.14. While the model without time delays do not present acceptable results, the model with time delays does by capturing the higher order dynamics in the actual system. As it is done for the longitudinal cyclic input responses, the frequency responses of p/δ_{lat} and q/δ_{lat} are checked as they are the most important ones.

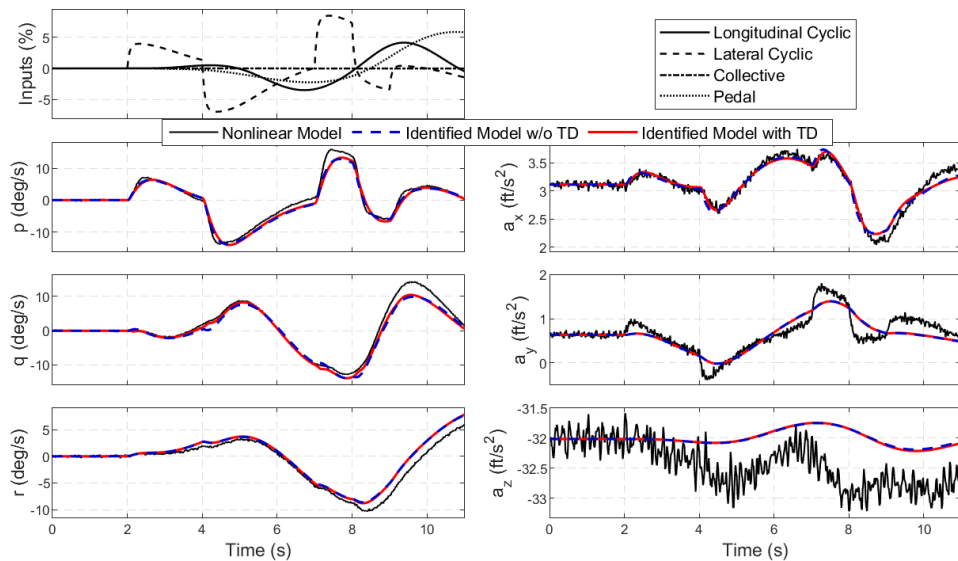


Figure 3.11: Lateral cyclic 2311 input in positive direction during hover

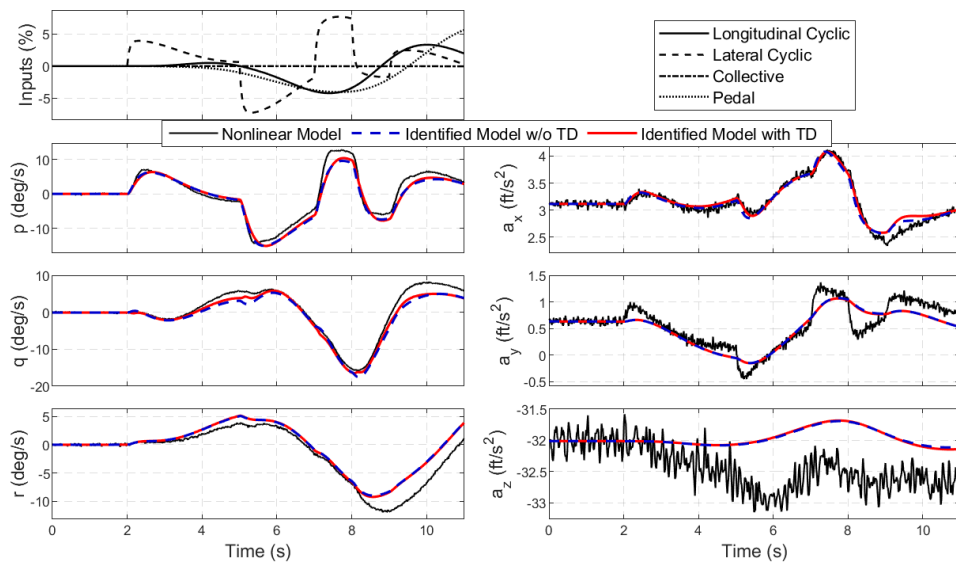


Figure 3.12: Lateral cyclic 3211 input in positive direction during hover

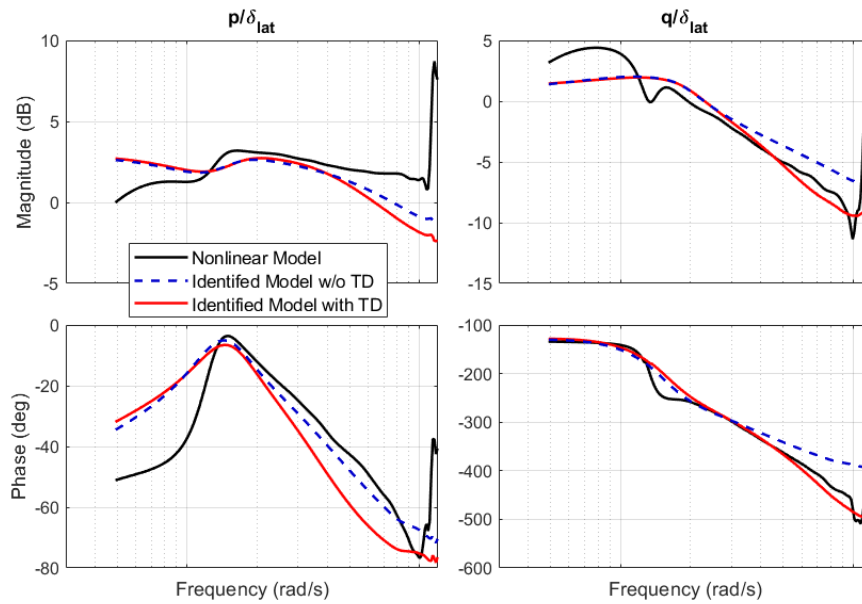


Figure 3.13: Frequency domain comparison of q/δ_{lat} and p/δ_{lat} input output pairs in lateral cyclic frequency sweep maneuver in hover

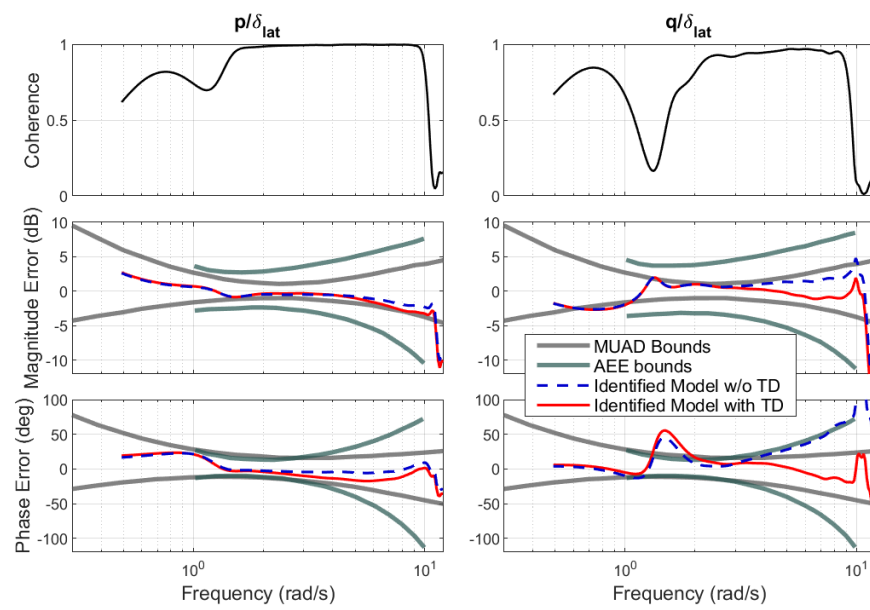


Figure 3.14: q/δ_{lat} and p/δ_{lat} input output pairs and error bounds in lateral cyclic frequency sweep maneuver in hover

3.1.1.3 Results for Collective Input

The results for 2311 and 3211 type inputs from the collective channel are presented. For this input channel the responses of yaw rate r and vertical specific acceleration a_z are considered since the excitations in other channels are small and are of lesser importance. Clearly, the identified systems with or without time delays can both capture the dynamics accurately.

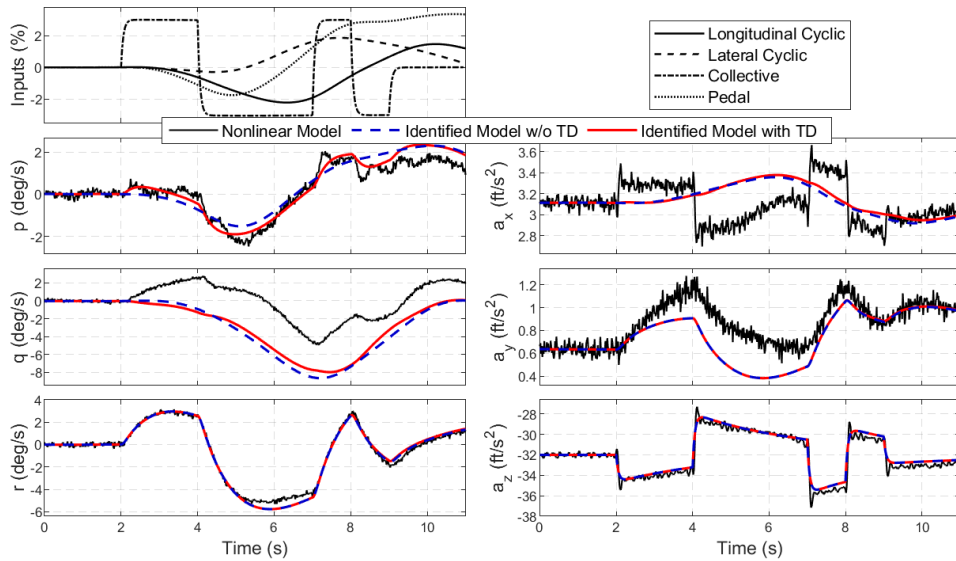


Figure 3.15: Collective 2311 input in positive direction during hover

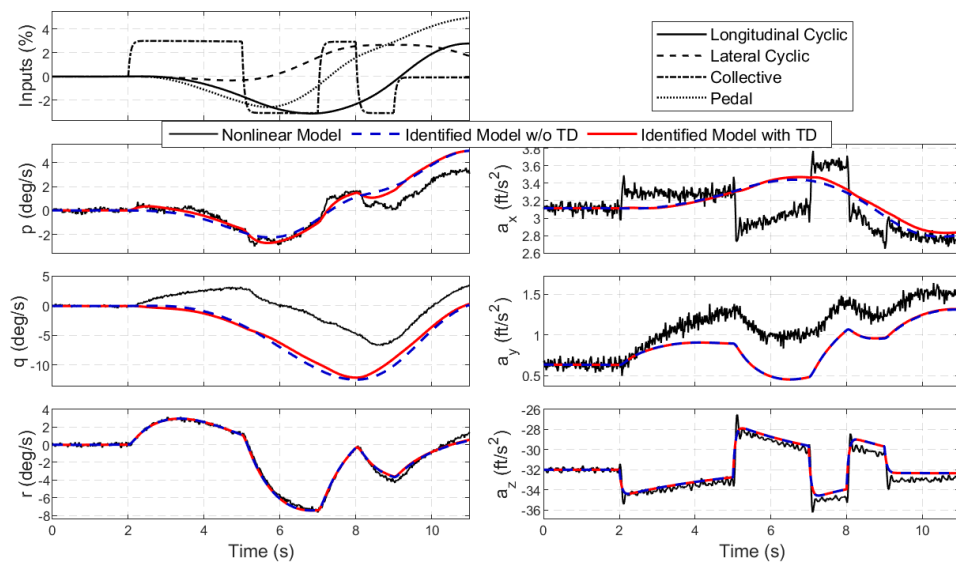


Figure 3.16: Collective 3211 input in positive direction during hover

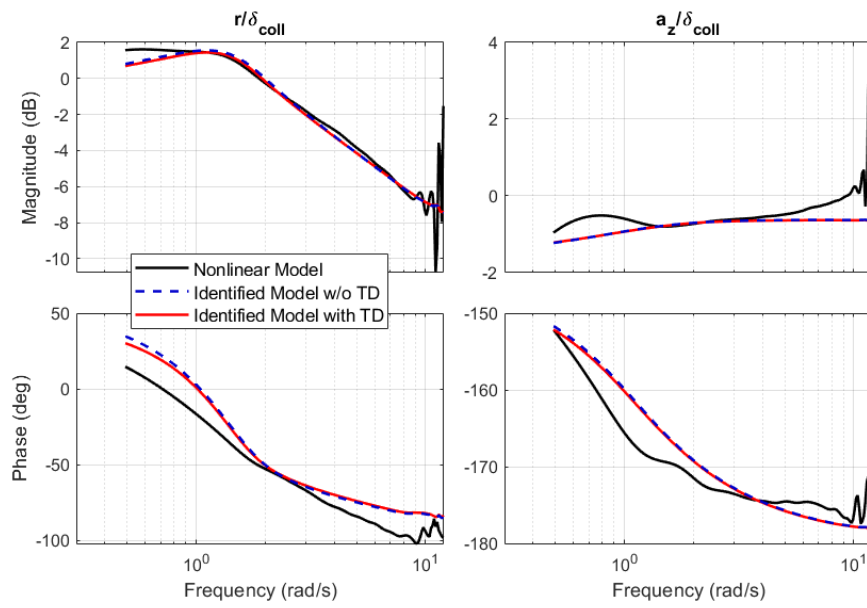


Figure 3.17: Frequency domain comparison of r/δ_{coll} and a_z/δ_{coll} input output pairs in collective frequency sweep maneuver in hover

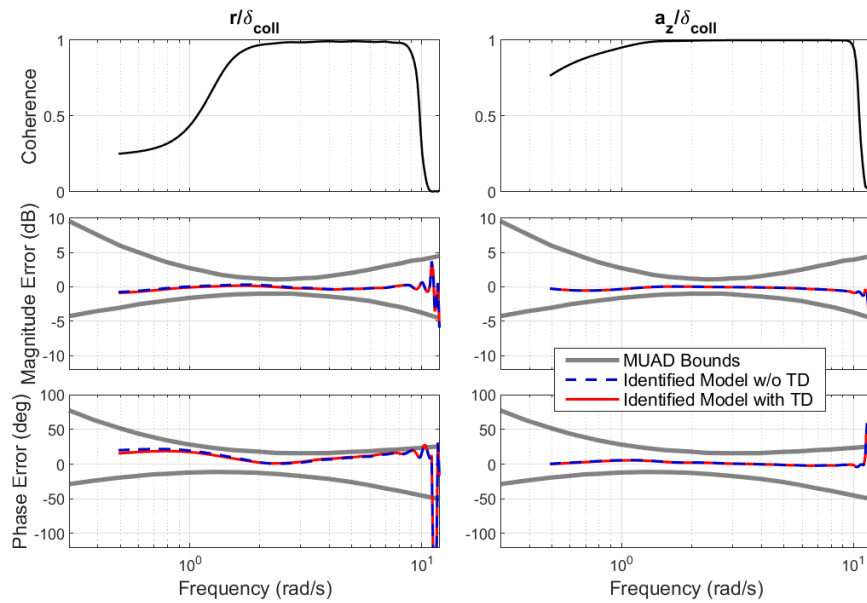


Figure 3.18: r/δ_{lat} and a_z/δ_{lat} input output pairs and error bounds in collective frequency sweep maneuver in hover

3.1.1.4 Results for Pedal Input

The last input channel to examine in hovering flight condition is pedal. The dynamics of yaw rate r and lateral specific acceleration a_y are crucial in pedal response. Similar to collective channel results, the identified systems are adequate whether they have time delays or not. This is an expected result, since time delays are only added to pitch and roll derivatives.

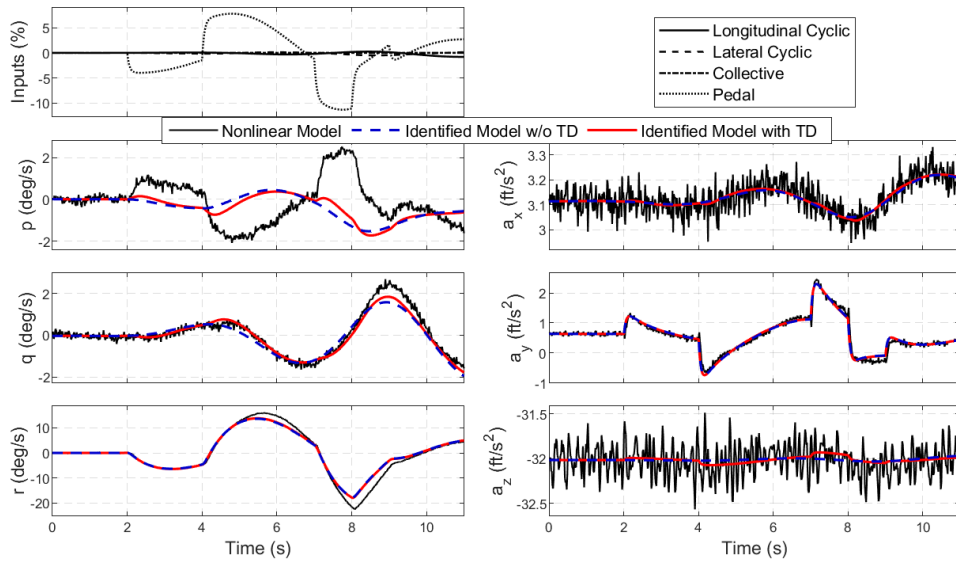


Figure 3.19: Pedal 2311 input in positive direction during hover

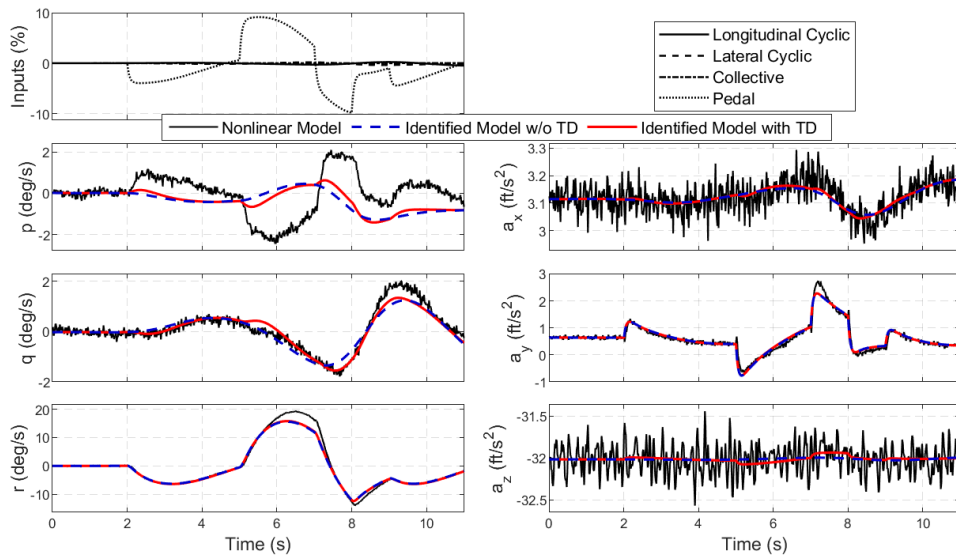


Figure 3.20: Pedal 3211 input in positive direction during hover

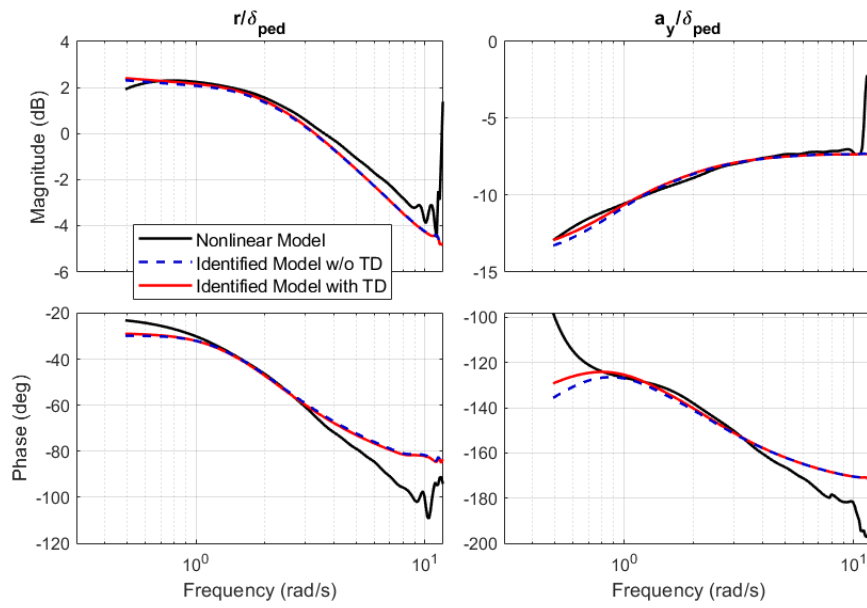


Figure 3.21: Frequency domain comparison of r/δ_{coll} and a_y/δ_{coll} input output pairs in pedal frequency sweep maneuver in hover

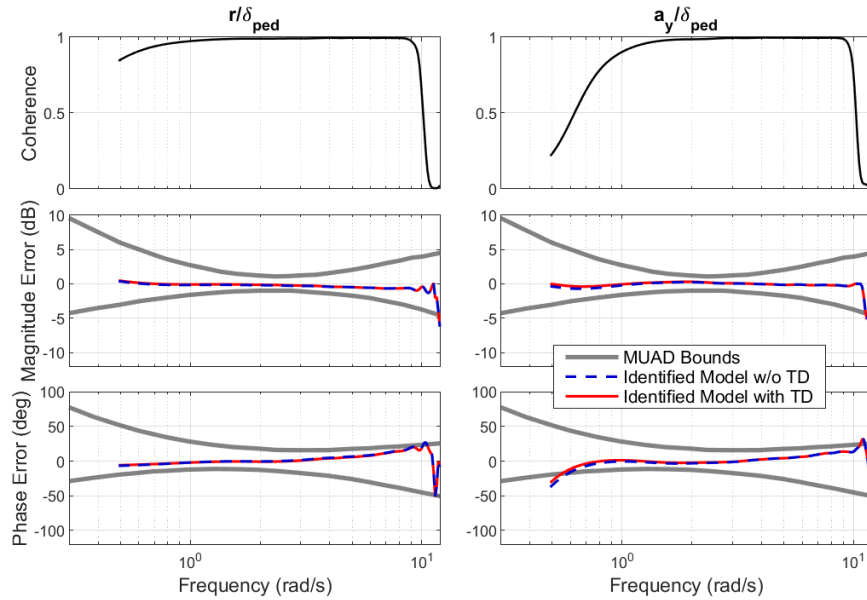


Figure 3.22: r/δ_{lat} and a_y/δ_{lat} input output pairs and error bounds in pedal frequency sweep maneuver in hover

3.1.2 Identification of Dynamics in Forward Flight

The second trim condition to be identified is forward flight with 70 knots of speed. The helicopter states and control positions at this trim condition is listed in table 3.3. Again, the values in the table are representative values.

As can be seen from table 3.1 there are 16 maneuvers of types 3211 and 2311 executed starting from this trim condition. The procedure followed for forward flight identification is similar to the hover case. As the first step, a model reduction procedure is carried out to determine an adequate model structure. As there is no prior information available about the system parameters, initial values of the parameters are set to zero. The model is converged with all identification parameters, and the one with the greatest insensitivity is removed by being equated to zero. Then, again starting from zero initial values, the procedure is repeated. The model reduction algorithm is continued until all parameters are dropped from the model structure and the variation of root mean square error is shown in figure 3.23.

By looking at figure 3.23, it can be seen that for the forward flight condition, the lowest root mean square error can be achieved with a model with 20 derivatives dropped from the fully populated model structure. Similar to hover trim condition, the RMSE value of the converged solution with adequate model structure is below the recommended threshold value of 2. The dropped derivatives are $X_v, X_q, X_r, X_{ped}, Y_u, Y_w, Y_q, Y_r, Y_{long}, Y_{coll}, Z_v, Z_p, Z_q, Z_{lat}, Z_{ped}, L_{ped}, M_u, M_v, M_{ped}$ and N_u . The elimination order of these parameters and their values, insensitivities and Cramer-Rao

Table 3.3: Trimmed state values at 70 knots forward flight

Parameter	Value	Parameter	Value
u_0	118.14 ft/s	δ_{long_0}	55.23 %
v_0	-8.65 ft/s	δ_{lat_0}	45.89 %
w_0	6.98 ft/s	δ_{coll_0}	58.54 %
ϕ_0	1.00 deg	δ_{ped_0}	70.35 %
θ_0	2.34 deg	Total Mass	2800.0 kg

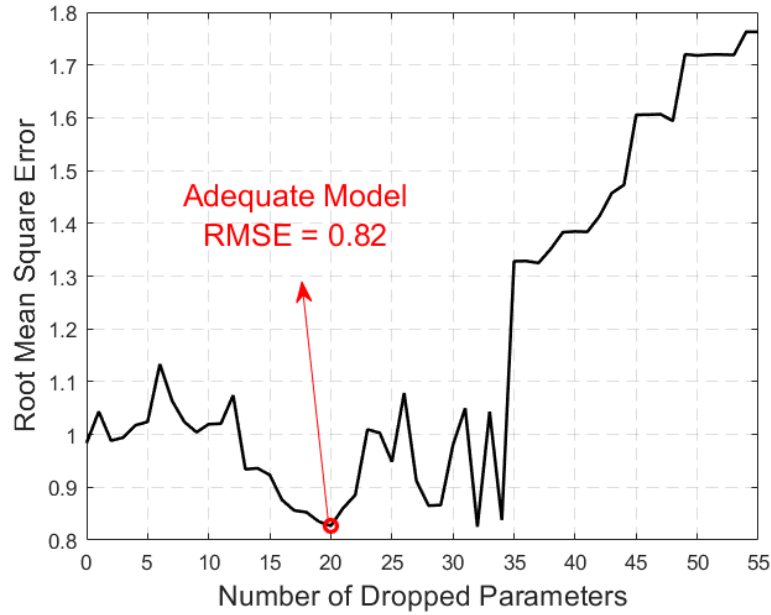


Figure 3.23: Variation of RMSE through model reduction in 70 knots forward flight

bounds are presented in Appendix B.

After the determination of the sufficient model structure, the obtained solution is examined. Figure 3.24 shows the iteration history of the model parameters. It can be seen that all parameters are converged after around 30 iterations. When the time domain results are examined, an inconsistency of the identified model to the truth model is seen. The phase error of the p/δ_{long} response in longitudinal cyclic tests do not satisfy the MUAD and AEE bounds. The q/δ_{lat} response in lateral cyclic frequency sweep test stays within the AEE bounds, but not MUAD bounds. This is a similar issue to the one experienced during identification of dynamics in hover. Since the error bounds are not satisfied in the off axis responses of cyclic input tests, the problem is thought to be due to additional dynamics that are not present in the identification model structure.

In helicopters, the pitch to roll motion is coupled due to gyroscopic effect of the rotor. In order to obtain a high accuracy model, these dynamics must be added to the model structure as with the employed model structure, the off axis responses to the cyclic inputs cannot be captured accurately. Following a similar procedure as the hover case, time delays are added to the model structure to account for the additional dynamics

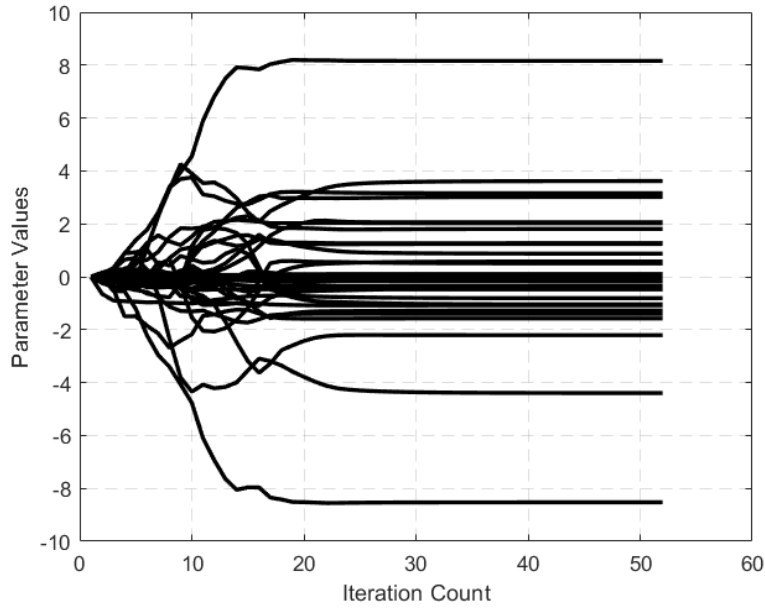


Figure 3.24: Iteration history of parameters for identification in 70 knots forward flight

due to rotor flapping. Initially, time delays are introduced only in the control matrix in order to avoid state delays. Time delays are added to derivatives L_{long} , L_{lat} , M_{long} , M_{lat} and the optimization loop is initiated. The parameter values found with the model structure without time delays are used as initial values, where the time delays are also identification parameters. Unlike identification in hover, the introduction of input delays to the control matrix are not sufficient to represent the additional dynamics in the system. Therefore, along with input delays, time delays are also introduced in the system matrix for pitch and roll related derivatives of L_p , L_q , M_p , M_q . With input and state delays, the optimization algorithm is executed again. Note that the delay parameters are saturated to zero to prevent negative time delays. Figure 3.25 shows the iteration histories of identification parameters.

The values, Cramer-Rao bounds and insensitivities of the identified parameters are provided in Appendix C. The values of the important derivatives are checked with reference [31] to confirm that they agree with rotorcraft dynamics. First of all, the angle of attack static stability derivative M_w is examined. In contrast to hover condition, this derivative is more dominant in forward flight conditions owing to the presence of

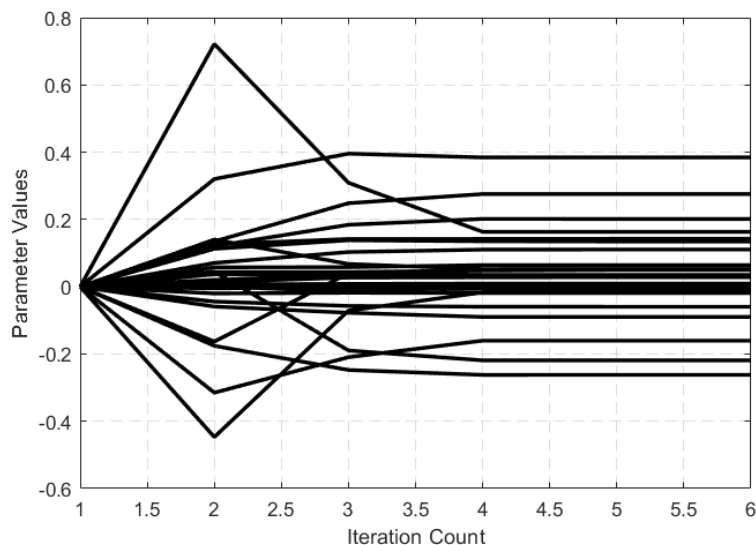


Figure 3.25: Iteration history of parameters for identification in 70 knots forward flight with additional dynamics

horizontal tail. Since the horizontal tail provides restoring moment when the angle of attack changes, this derivative is expected to be negative in forward flight. The discussions for the dihedral effect derivative L_v is similar to hover, where the sign of the derivative is again negative. The weathercock stability derivative N_v is positive in forward flight conditions, but along with the contribution of the tail rotor, the vertical tail also produces restoring yaw moment. The heave stability derivative Z_w is again negative, as it is in the hover condition. The results in Appendix C show that the obtained parameter values are consistent with helicopter dynamics.

3.1.2.1 Results for Longitudinal Cyclic Input

The first input channel that the results are examined is longitudinal cyclic. Responses from the identified models with and without time delays are shown in figures 3.26 and 3.27, along with the simulation data from the truth model. Similar to the discussion in hover, accurate identification of the pitch and roll dynamics in longitudinal and lateral cyclic maneuvers have the utmost importance. The pitch rate response of the two identified models are perfectly fitted to the truth model data. The specific acceleration responses also show good agreement with the truth model data. When the

roll rate responses are compared, It is seen that the identified models can capture the magnitude content accurately, but the higher frequency oscillations are not identified precisely without time delays.

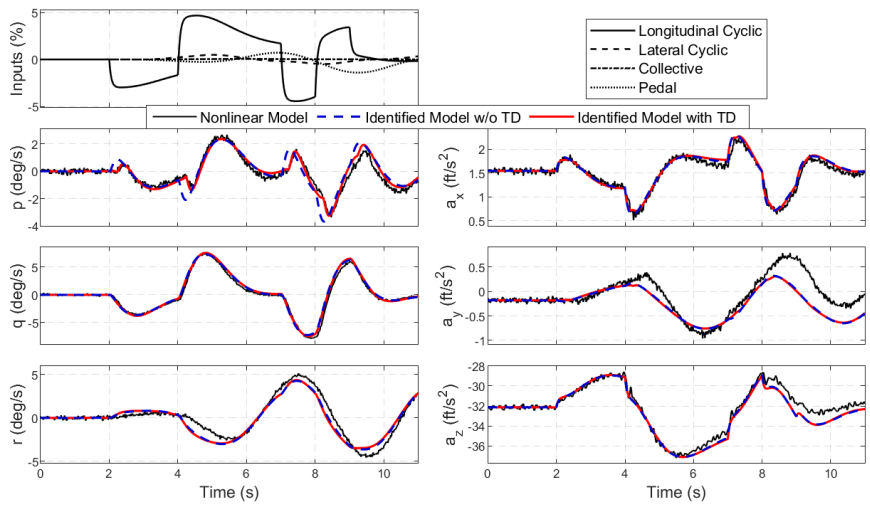


Figure 3.26: Longitudinal cyclic 2311 input in positive direction during 70 knots forward flight

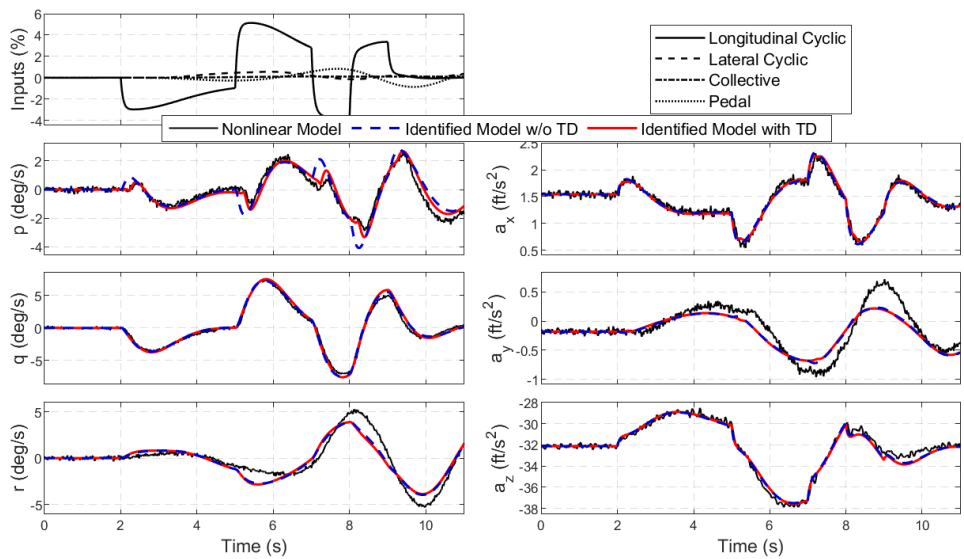


Figure 3.27: Longitudinal cyclic 3211 input in positive direction during 70 knots forward flight

The need for time delays become more apparent in figures 3.28 and 3.29. Figure 3.28 displays the frequency responses of the identified systems and the truth model with bode plots. The phase response of the identified model for p/δ_{long} input output pair is

refined significantly with the introduction of time delays. Figure 3.29 visualizes the error in the frequency responses of the two identified models. While no significant improvement is observed in pitch rate response errors, the phase error of the roll rate diminished significantly. Even though the phase error of the pitch rate degraded slightly, a pilot cannot notice this difference since the error is still within the MUAD bounds.

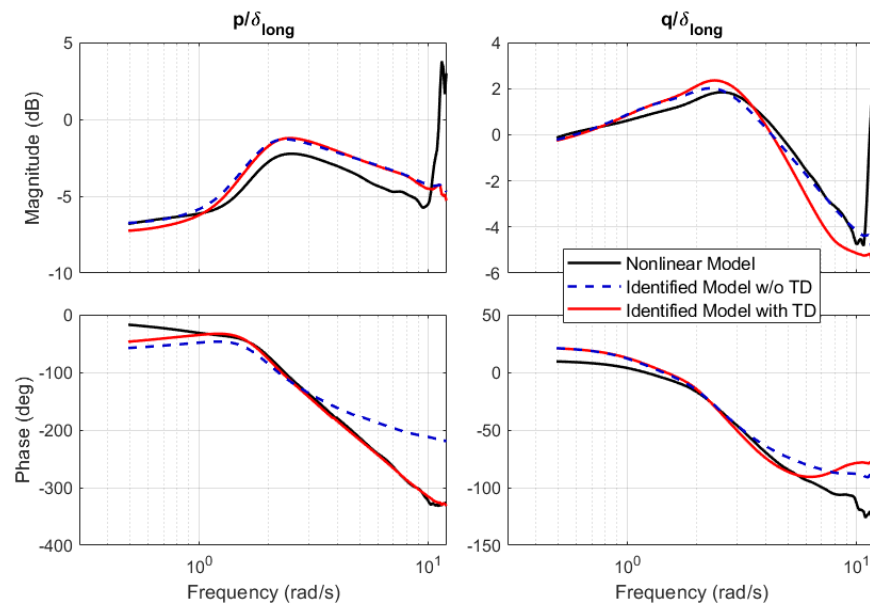


Figure 3.28: Bode plots of q/δ_{long} and p/δ_{long} pairs for frequency sweep in longitudinal cyclic in 70 knots forward flight

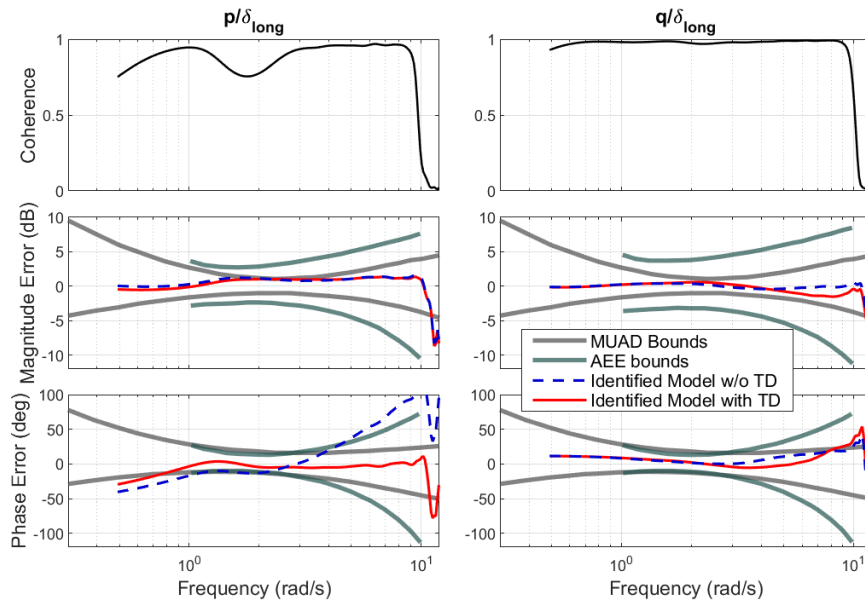


Figure 3.29: Coherence and Errors of q/δ_{long} and p/δ_{long} pairs for frequency sweep in longitudinal cyclic in 70 knots forward flight

3.1.2.2 Results for Lateral Cyclic Input

The obtained models produce overall satisfactory identification results in lateral cyclic maneuvers. However, the high frequency oscillations in the pitch rate response cannot be captured accurately with the model structure without time delays, as can be seen in figures 3.30 and 3.31. This error is also reflected in frequency domain responses. Figure 3.33 displays the magnitude and phase errors. The frequency response of roll rate produces good coherence values on a wide frequency range, and the errors are small. The phase error in the pitch rate response is brought down to acceptable region with utilization of time delays.

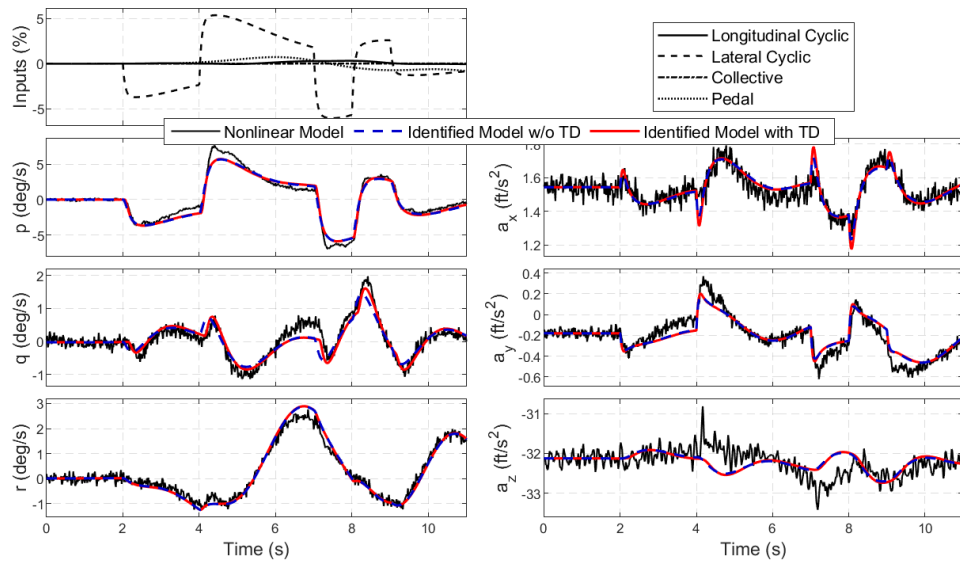


Figure 3.30: Lateral cyclic 2311 input in positive direction during 70 knots forward flight

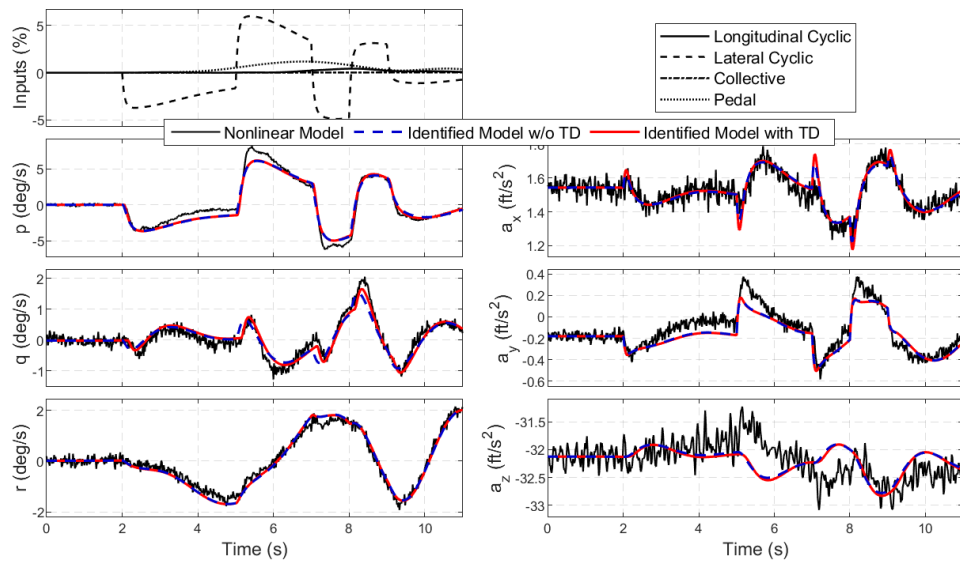


Figure 3.31: Lateral cyclic 3211 input in positive direction during 70 knots forward flight

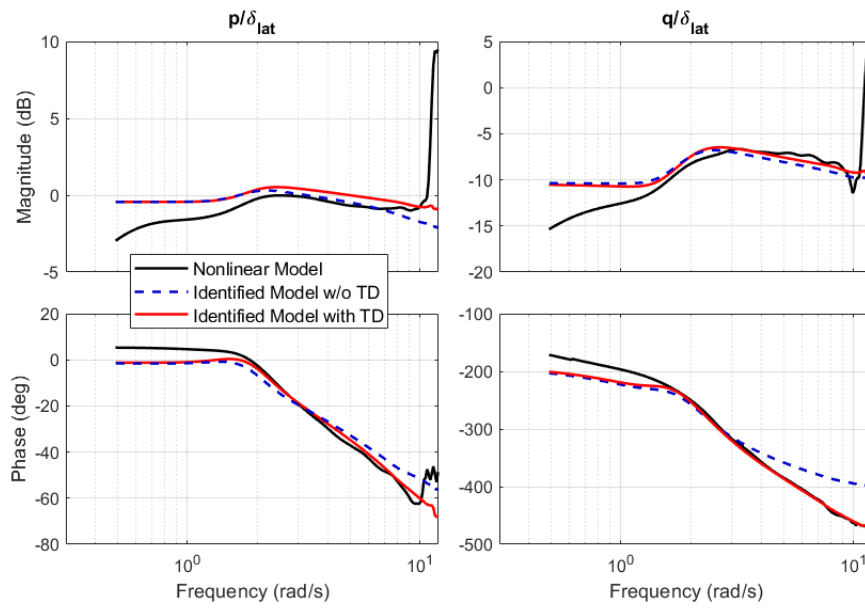


Figure 3.32: Frequency domain comparison of q/δ_{lat} and p/δ_{lat} input output pairs in lateral cyclic frequency sweep maneuver 70 knots in forward flight

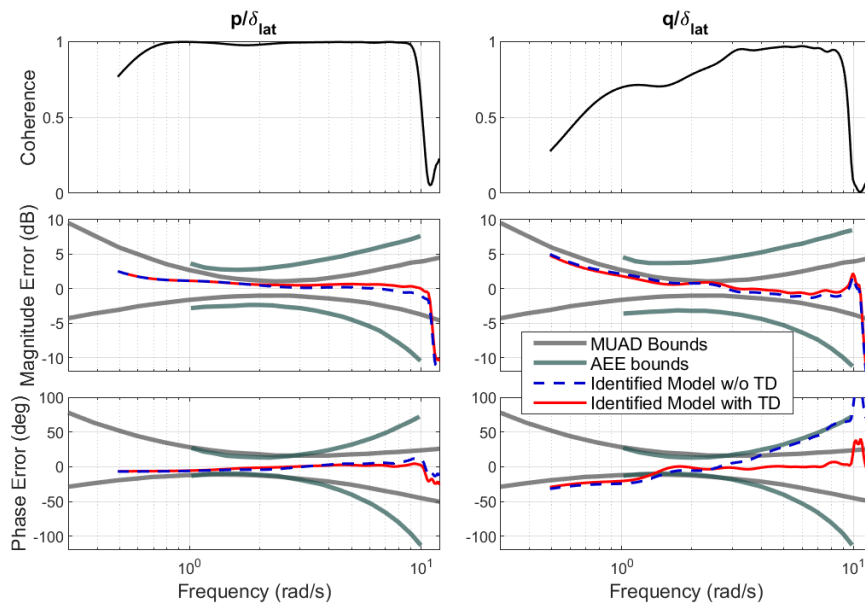


Figure 3.33: q/δ_{lat} and p/δ_{lat} input output pairs and error bounds in lateral cyclic frequency sweep maneuver in 70 knots forward flight

3.1.2.3 Results for Collective Input

When the obtained models are compared with the truth model signals in collective input tests, it is seen that an overall acceptable model fit is acquired. The models with or without time delays produce sufficient accuracy, as verified by the errors in frequency domain in figure 3.37.

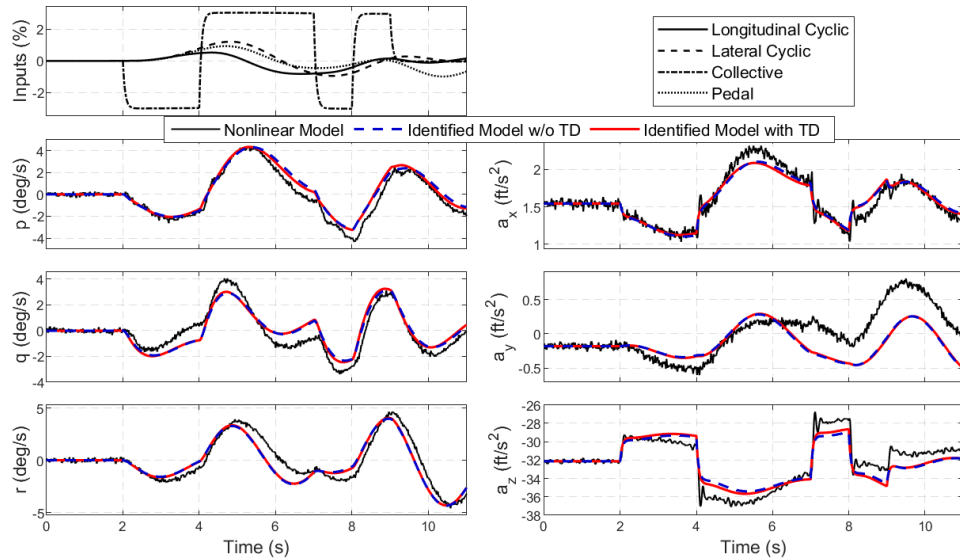


Figure 3.34: Collective 2311 input in positive direction during 70 knots forward flight

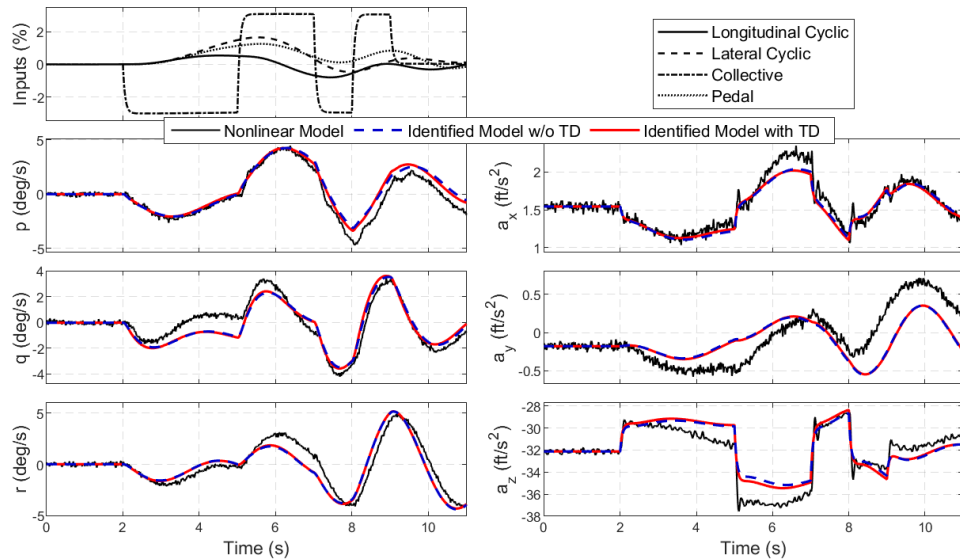


Figure 3.35: Collective 3211 input in positive direction during 70 knots forward flight

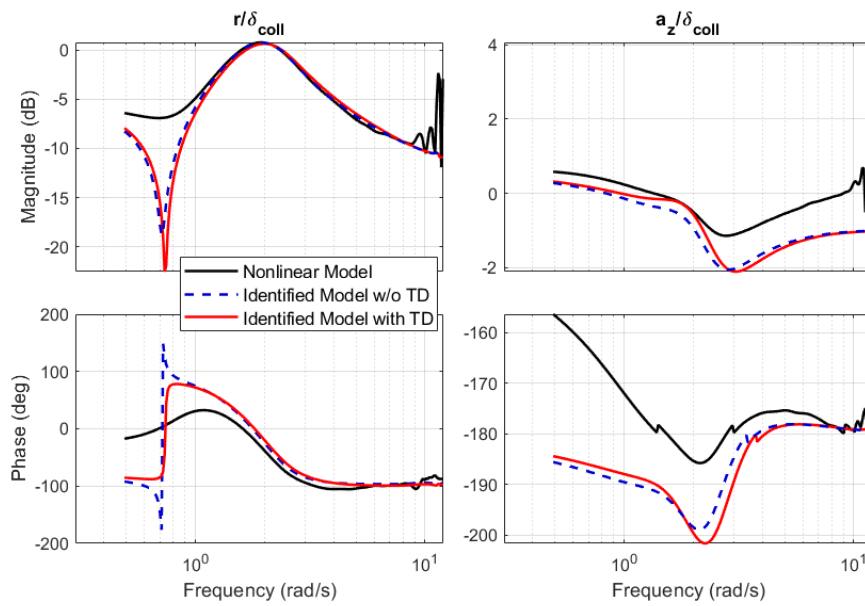


Figure 3.36: Frequency domain comparison of r/δ_{coll} and a_z/δ_{coll} input output pairs in collective frequency sweep maneuver in 70 knots forward flight

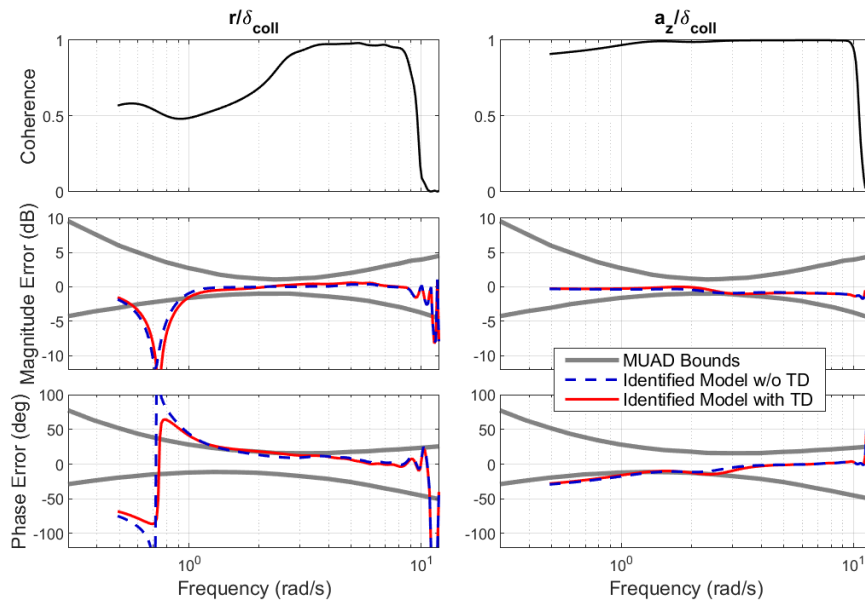


Figure 3.37: r/δ_{lat} and a_z/δ_{lat} input output pairs and error bounds in collective frequency sweep maneuver in 70 knots forward flight

3.1.2.4 Results for Pedal Input

The discussion for pedal tests is similar to the one for collective tests. The model fits are decent even without time delays, so no time delays are added to related derivatives.

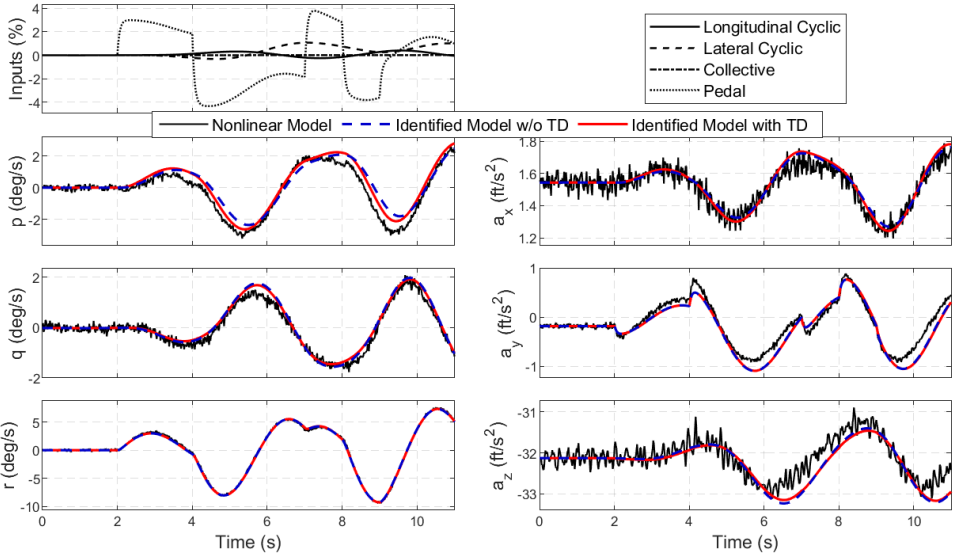


Figure 3.38: Pedal 2311 input in positive direction during 70 knots forward flight

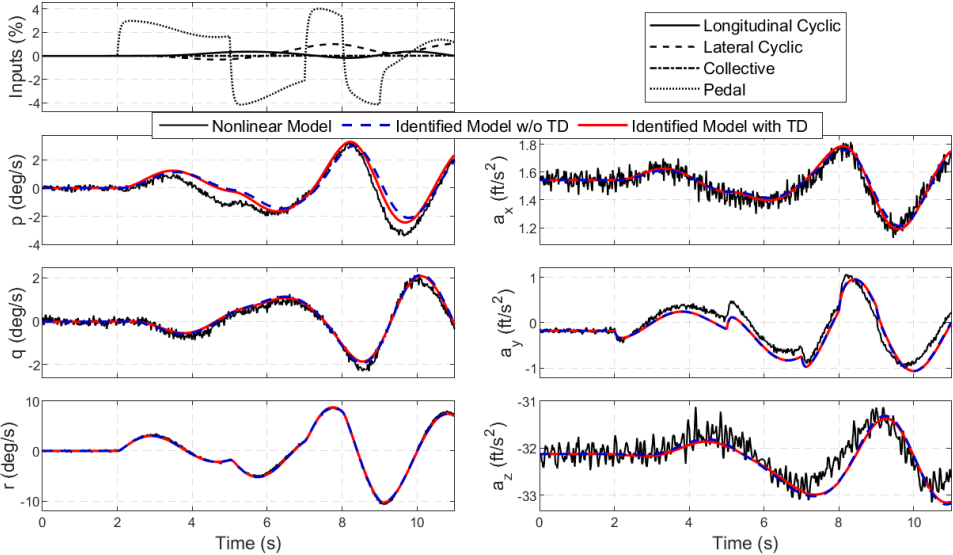


Figure 3.39: Pedal 3211 input in positive direction during 70 knots forward flight

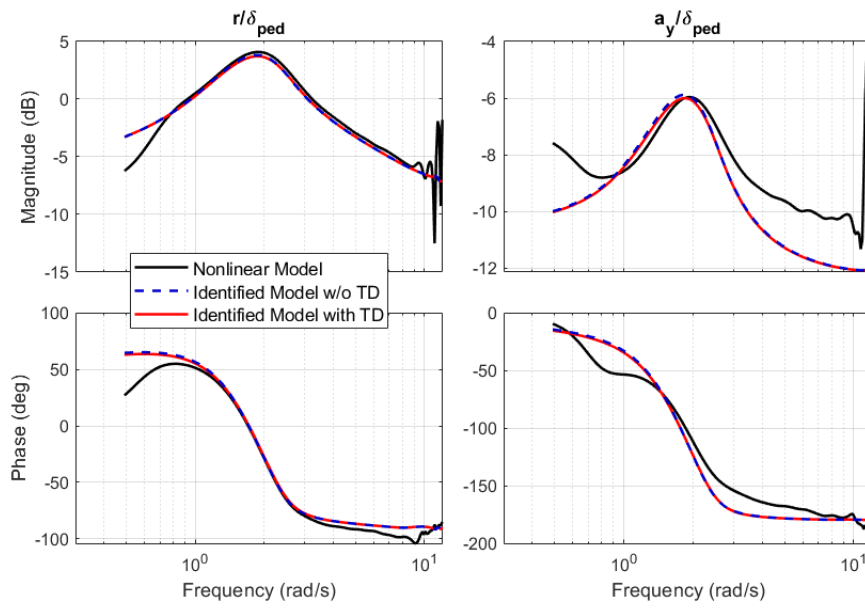


Figure 3.40: Frequency domain comparison of r/δ_{coll} and a_y/δ_{coll} input output pairs in pedal frequency sweep maneuver in 70 knots forward flight

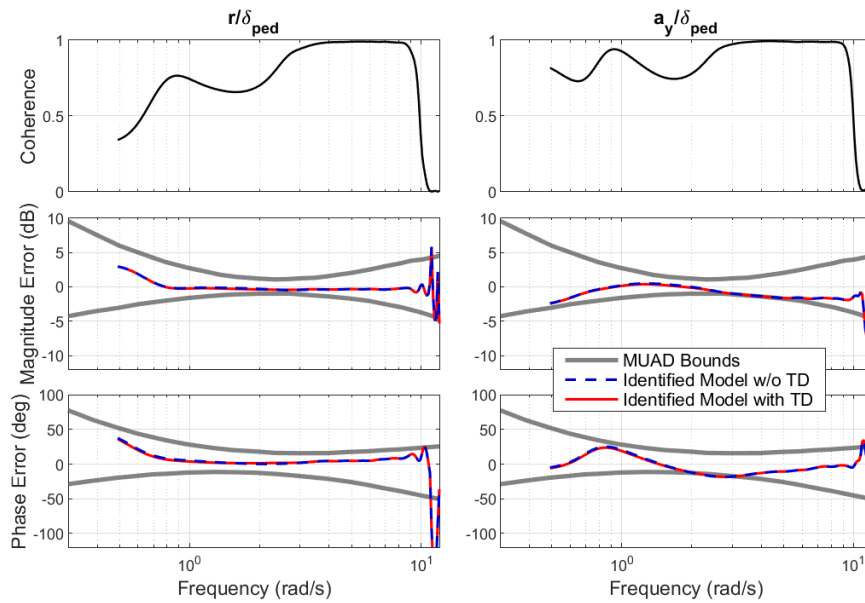


Figure 3.41: r/δ_{lat} and a_y/δ_{lat} input output pairs and error bounds in pedal frequency sweep maneuver in 70 knots forward flight

3.2 Results with an Initial Model Structure from Adaptive Learning

This section focuses on the identification of rotorcraft dynamics, where the initial model structure and the initial conditions of the model parameters are determined via adaptive learning algorithm. The obtained model structure is then inserted to the maximum likelihood output error algorithm developed through Chapter 2, to account for the higher order dynamics in the system and refine the identified model in time domain. The theory and implementation of the adaptive learning algorithm is not shown here explicitly, but can be accessed in [13]. To generate the truth model data, the same high fidelity model of H135 helicopter is utilized.

The adaptive learning algorithm is an equation error based optimization method, developed using the algorithms for adaptive control presented in [6–8]. The 6-Dof dynamics of the helicopter is implemented in the adaptive learning representation, where the aerodynamic derivatives in the state and control matrices have adaptive weights. Using the adaptive learning parameter update law, these weights, which can be referred as identification parameters, are converged around the ideal weight values. The algorithm guarantees the identification parameters to be constrained with constant oscillations in the converged state. As the weights are driven to their ideal values with convergence, a unique optimal solution exists as linearly independent set of vectors are accumulated in the data stack matrix. The data stack matrix is constructed by the concatenation of the basis (state) vectors selected from time histories of the truth model maneuver signals. The linear independence between the basis vectors is ensured by the maximization of the minimum singular value of the data stack matrix [6]. After the initiation of the learning algorithm, the minimum singular value of the data stack matrix increases as new basis vectors are selected to be included in the data stack matrix. Once the data stack matrix is full, new basis vectors are selected such that the minimum singular value is increased when an old basis vector is replaced with the new one. When minimum singular value stops increasing and converges, parameter convergence is achieved. Furthermore, by utilizing minimum singular value maximization principle, the same converged values of parameters can be achieved independent of the initial parameter guesses. This is due to the fact that the parameter estimates of adaptive learning depends on the data being used, not

initial values. Figure 3.42 illustrates this issue as the same parameter estimates are achieved with zero and random initial conditions and the same minimum singular value history is obtained for both cases. The horizontal axis represents epoch, which is the concatenated time histories of all test maneuvers used in identification.

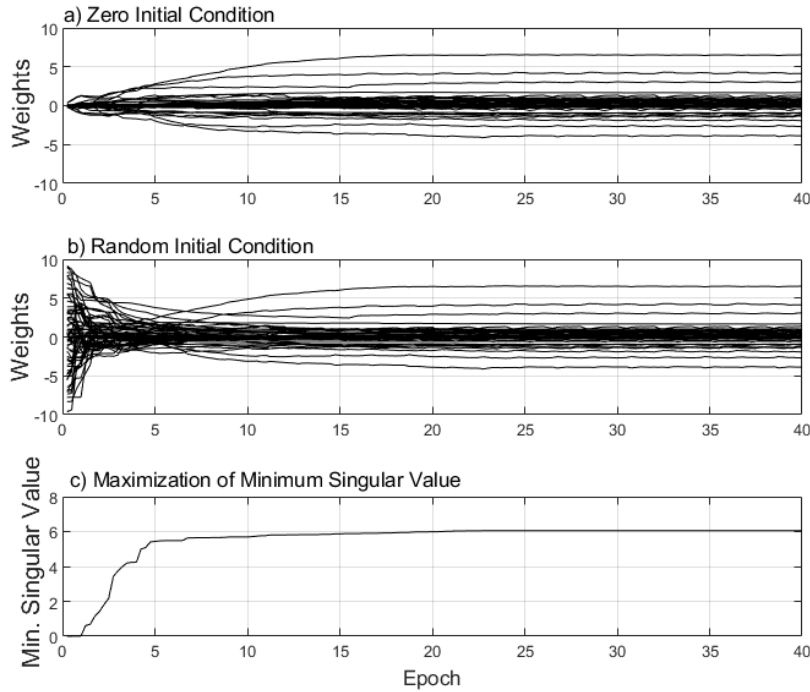


Figure 3.42: Example parameter convergence with adaptive learning (adapted from [13])

A model structure determination routine aims to achieve a minimal model representation with redundant derivatives dropped from the model structure. In that sense, the procedure can be referred to as model reduction. The oscillating boundedness of the converged parameters can also be employed as a basis for a model structure determination routine. Each identification parameter is considered as a random variable associated with a mean value and standard deviation. The statistical properties of the oscillations indicate the parameter influence on the model response. The standard deviation of each parameter estimate can be directly calculated from the oscillations in its converged state. Whenever a parameter is removed from the model structure, the remaining parameters converge and oscillate around another value, which creates a bias between the parameter estimates as shown in 3.43

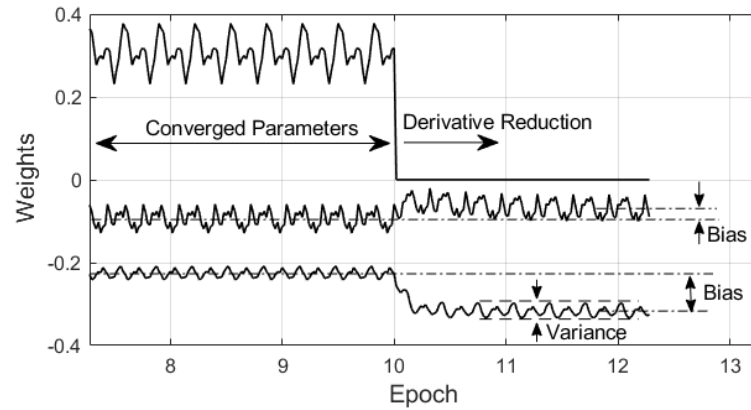


Figure 3.43: Example parameter reduction with adaptive learning [13]

Initially, with all unknown parameters present in the model structure, the algorithm is converged. Then, the parameter with the greatest variance (or standard deviation) is removed from the model by being equated to zero. After parameter elimination, the model is rapidly re-converged and the biases and variances of the converged parameter oscillations and biases are examined. This procedure is repeated and the parameters of lesser importance are dropped from the model structure one by one, similar to the Hessian based routine discussed in Chapter 2. The approach makes use of the bias variance tradeoff presented in [28] to determine an adequate model structure. In the initial phases of model reduction, the standard deviations of parameter estimates are large and the biases after parameter drops are small. As parameters are removed from the model, the bias errors grow and standard deviations become smaller. Using this principle, the model reduction procedure is terminated when the sum of squares of biases and sum of variances are roughly equal. The parameters removed from the model structure can be found in reference [13].

The converged parameter values are then inserted in the maximum likelihood output error algorithm developed in Chapter 2 to refine the obtained solution and introduce time delays in related parameters to account for additional dynamics in the actual system. During maximum likelihood refinement, Levenberg-Marquardt algorithm is again employed to avoid intermediate divergence and have parameter updates in the steepest descent direction of the cost function. Figure 3.44 shows the iteration histories of the parameters together with the acquired root mean square error (RMSE) values in hover.

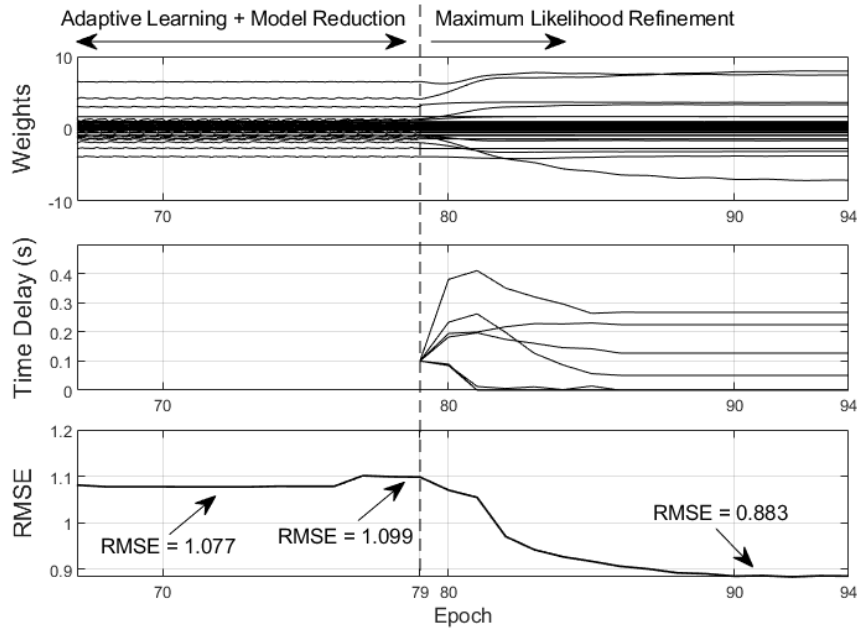


Figure 3.44: Iteration histories in hover [13]

As discussed in previous chapters, using maximum likelihood output error algorithm, the identification results may depend on the initial conditions of the model parameters and the model structure specified. If the starting point of the algorithm is far from the optimal solution, intermediate divergence can be experienced. The Hessian based model reduction approach discussed in Chapter 2 presents a systematic procedure to achieve an adequate model structure, but do guarantee uniqueness of the solution. As parameters are removed one by one using the Hessian matrix, the arrived final model structure might not be the unique and optimal one. The properties of adaptive learning makes up for these shortcomings of the output error algorithm, as it provides unique and optimal solutions independent of the initial parameter guesses. Therefore, it is a perfect startup method to be used prior to maximum likelihood optimization.

The identification using adaptive learning method is carried out by employing the 3211 type maneuvers as the identification data. 2311 and frequency sweep type maneuvers are used for verification in time and frequency domains respectively. The obtained model structures are then fed to the maximum likelihood algorithm, where time delays are added to related parameters as necessary. Similar to the previous case, the implemented time delay parameters are saturated to zero in order to prevent non-

physical negative time delays. Identifications in two flight conditions are performed, namely hover and forward light with 70 knots speed.

3.2.1 Identification of Dynamics in Hover

First, the identification results in hover are examined. Figure 3.45 shows the 2311 type maneuvers executed in each control channel. By looking at the responses, it can be seen that both standalone adaptive learning algorithm and maximum likelihood refinement are successful in terms of capturing the overall dynamics of the aircraft.

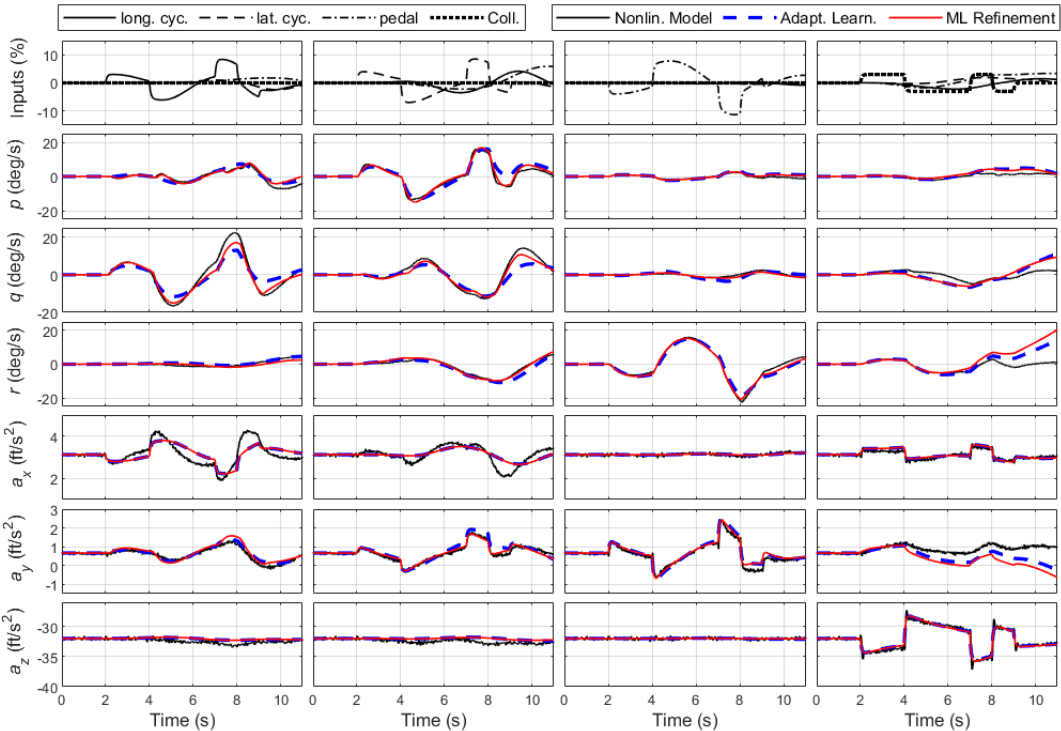


Figure 3.45: Time domain results of adaptive learning and maximum likelihood refinement in hover

The difference between the two algorithms becomes more apparent when the frequency responses are examined. The frequency response of the frequency sweep maneuver in longitudinal cyclic channel is displayed in figure 3.46. The error magnitude and phase errors of the identified models are compared with MUAD and AEE bounds in figure 3.47. Even though the general characteristics of the helicopter are captured by adaptive learning, the magnitude and phase errors are not within the bounds for

pitch and roll responses. Due to presence of rotor dynamics in the truth model data, a model structure with 6DOF is often found deficient to identify the system precisely. To refine the obtained results and to account for the additional dynamics due to rotor, a secondary algorithm is necessary. For this purpose, the maximum likelihood parameter estimation principle discussed in this work is employed. The output error algorithm developed in this work provides excellent results with its higher accuracy in identification and capability to handle time delays in the model structure. In figure 3.47, it is seen that with the ML refinement, phase and magnitude errors are reduced significantly.

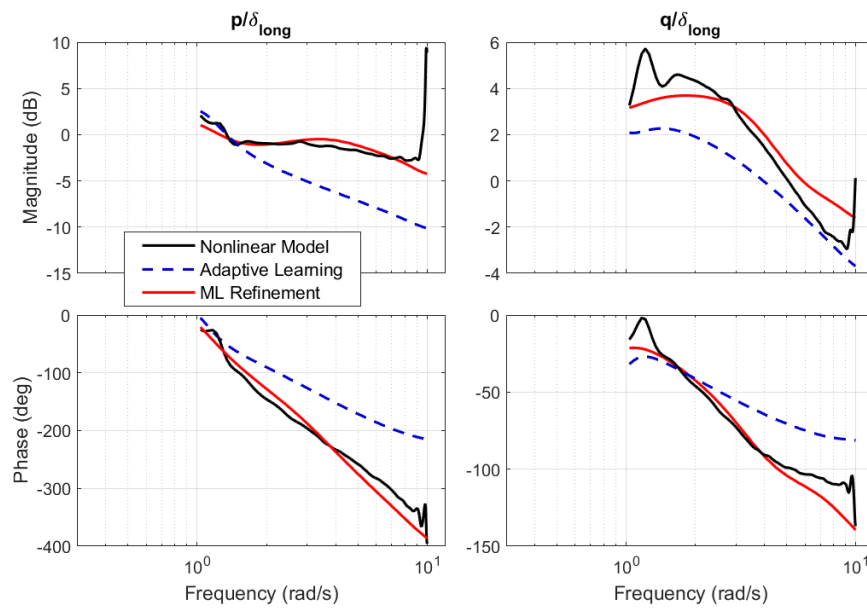


Figure 3.46: Frequency domain comparison of adaptive learning and maximum likelihood refinement with truth model in longitudinal cyclic maneuver in hover

A similar observation can be made for lateral cyclic input tests. The off axis pitch response of the model from adaptive learning produces high magnitude and phase errors. With the employment of time delays and output error method, the errors are diminished. When collective and pedal tests are considered, however, the models obtained via adaptive learning provide satisfactory results.

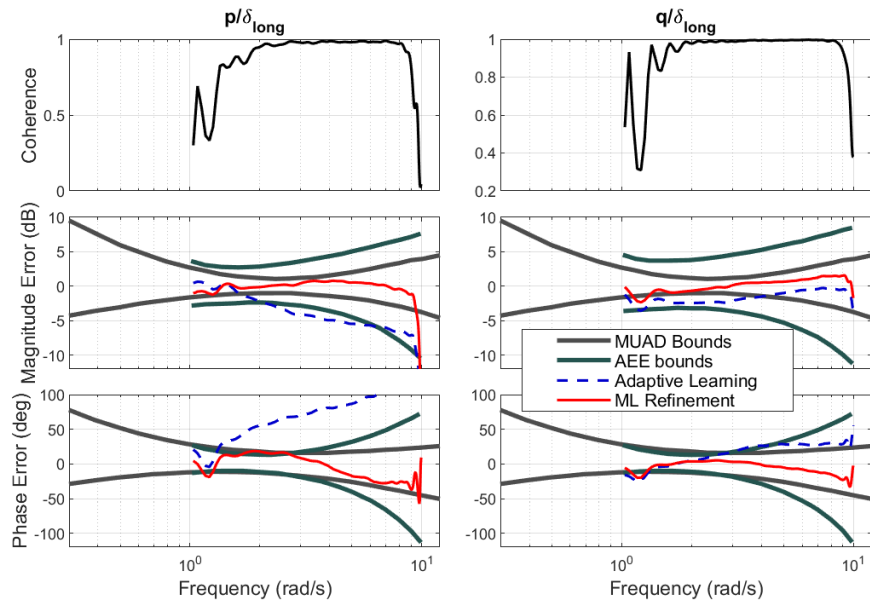


Figure 3.47: Coherence and errors of adaptive learning and maximum likelihood refinement with truth model in longitudinal cyclic maneuver in hover

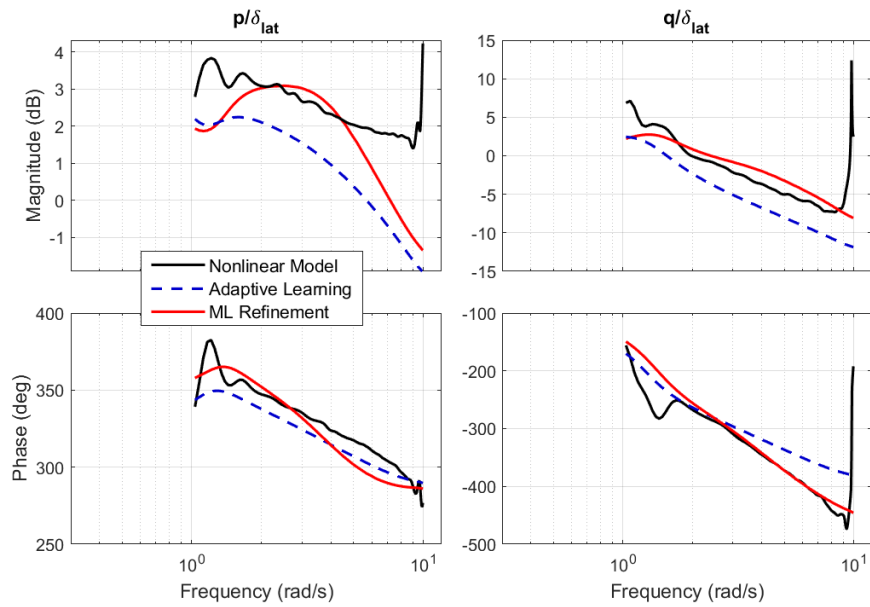


Figure 3.48: Frequency domain comparison of adaptive learning and maximum likelihood refinement with truth model in lateral cyclic maneuver in hover

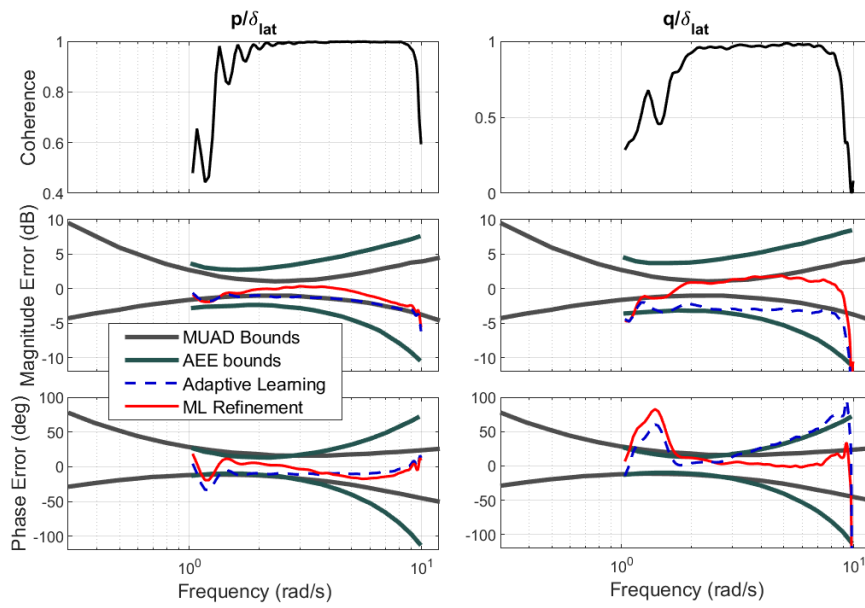


Figure 3.49: Coherence and errors of adaptive learning and maximum likelihood refinement with truth model in lateral cyclic maneuver in hover

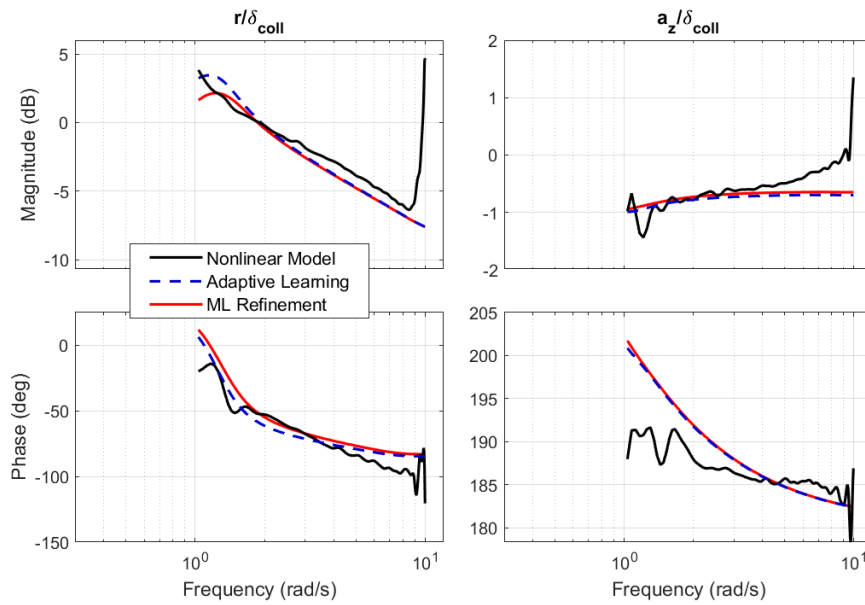


Figure 3.50: Frequency domain comparison of adaptive learning and maximum likelihood refinement with truth model in collective maneuver in hover

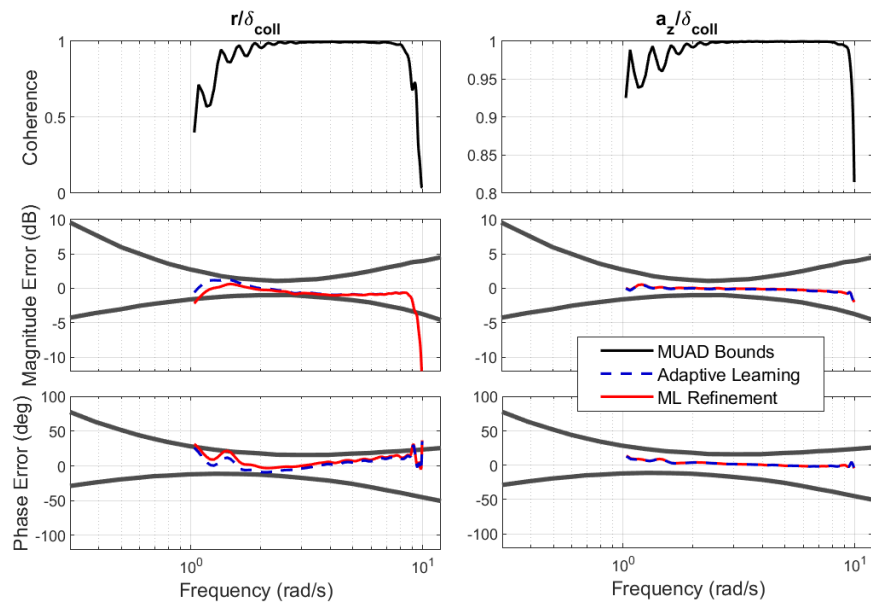


Figure 3.51: Coherence and errors of adaptive learning and maximum likelihood refinement with truth model in collective maneuver in hover

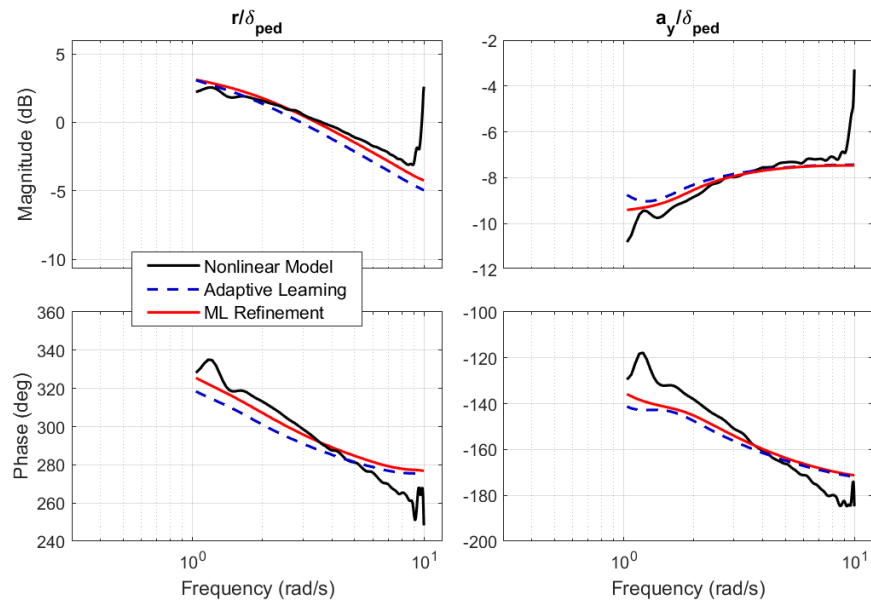


Figure 3.52: Frequency domain comparison of adaptive learning and maximum likelihood refinement with truth model in pedal maneuver in hover

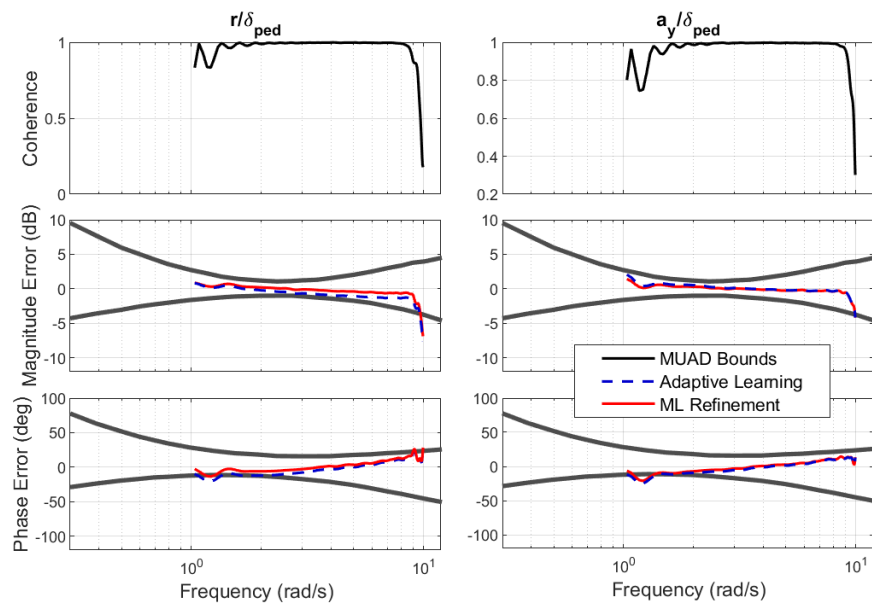


Figure 3.53: Coherence and errors of adaptive learning and maximum likelihood refinement with truth model in pedal maneuver in hover

3.2.2 Identification of Dynamics in Forward Flight

The second flight condition to be identified is forward flight with 70 knots of speed. First, the model reduction routine with adaptive learning is executed and the attained model structure and parameter values are provided to the maximum likelihood algorithm. Again, the standalone adaptive learning algorithm can capture the dynamics of the helicopter up to some extent, but maximum likelihood refinement is necessary to have smaller errors in frequency content. Like the results in hover, the pitch and roll responses in longitudinal and lateral cyclic maneuvers are improved significantly with the addition of time delays. Also, slight improvements on collective and pedal responses are observed. These improvements are not due to involvement of time delays, as they are only placed at the roll and pitch derivatives of the model. The improvement in these maneuvers is a result of maximum likelihood estimation principle.

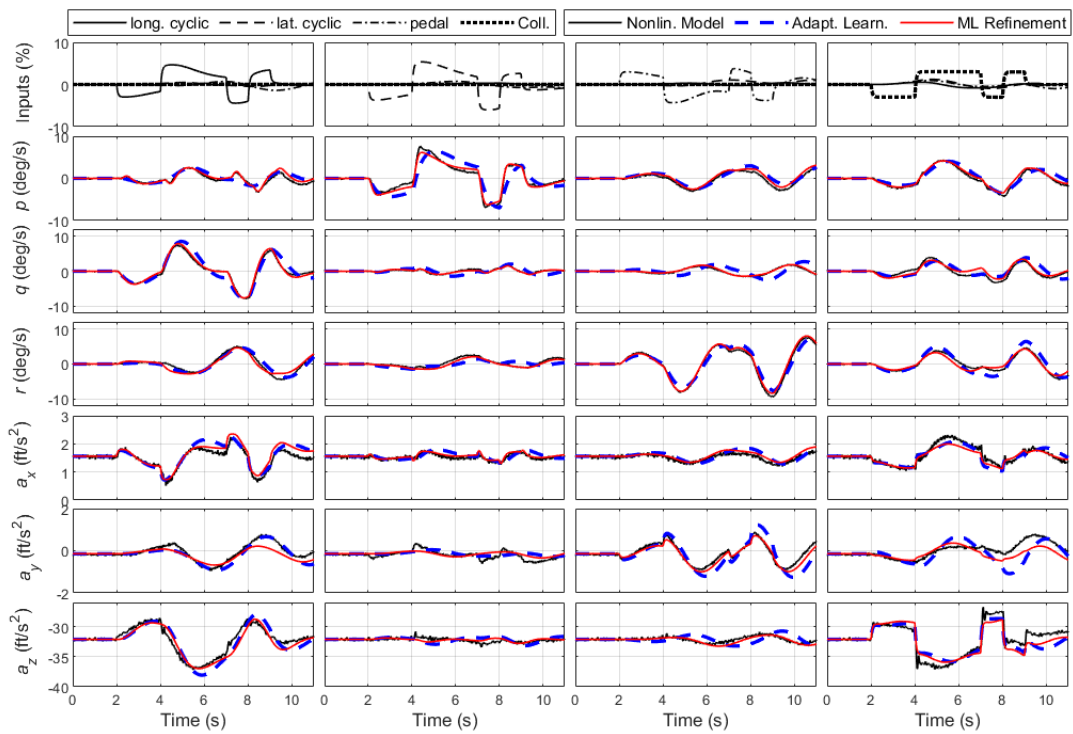


Figure 3.54: Time domain results of adaptive learning and maximum likelihood refinement in 70 knots forward flight

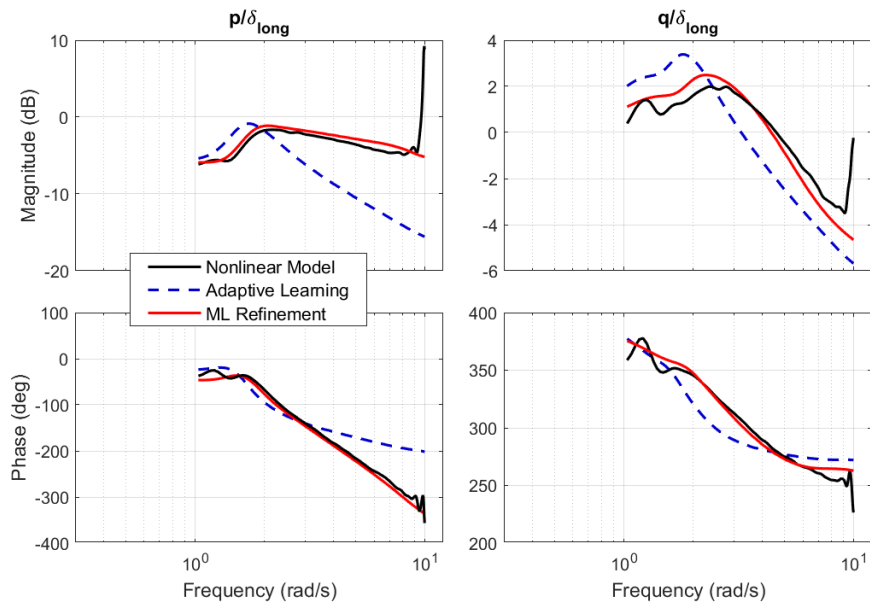


Figure 3.55: Frequency domain comparison of adaptive learning and maximum likelihood refinement with truth model in longitudinal cyclic maneuver in 70 knots forward flight

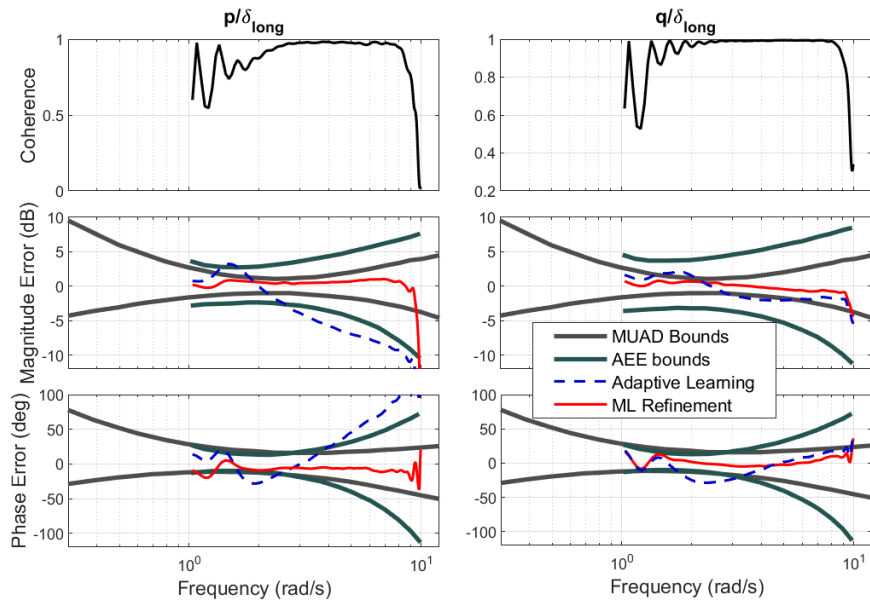


Figure 3.56: Coherence and errors of adaptive learning and maximum likelihood refinement with truth model in longitudinal cyclic maneuver in 70 knots forward flight

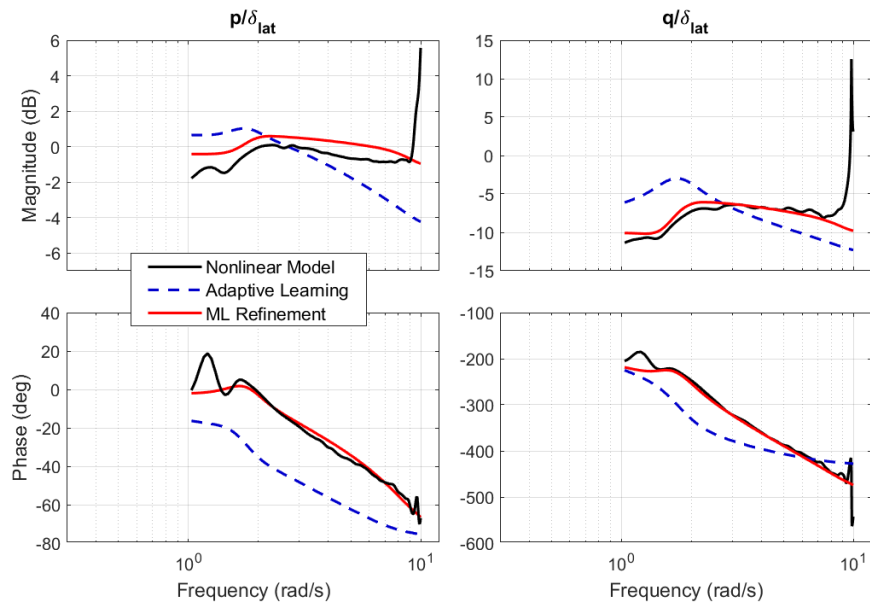


Figure 3.57: Frequency domain comparison of adaptive learning and maximum likelihood refinement with truth model in lateral cyclic maneuver in 70 knots forward flight

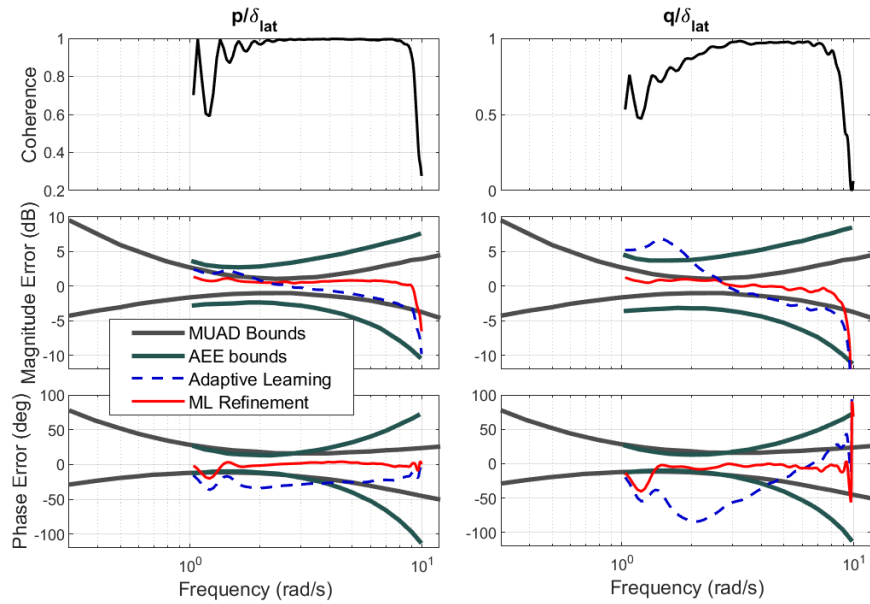


Figure 3.58: Coherence and errors of adaptive learning and maximum likelihood refinement with truth model in lateral cyclic maneuver in 70 knots forward flight

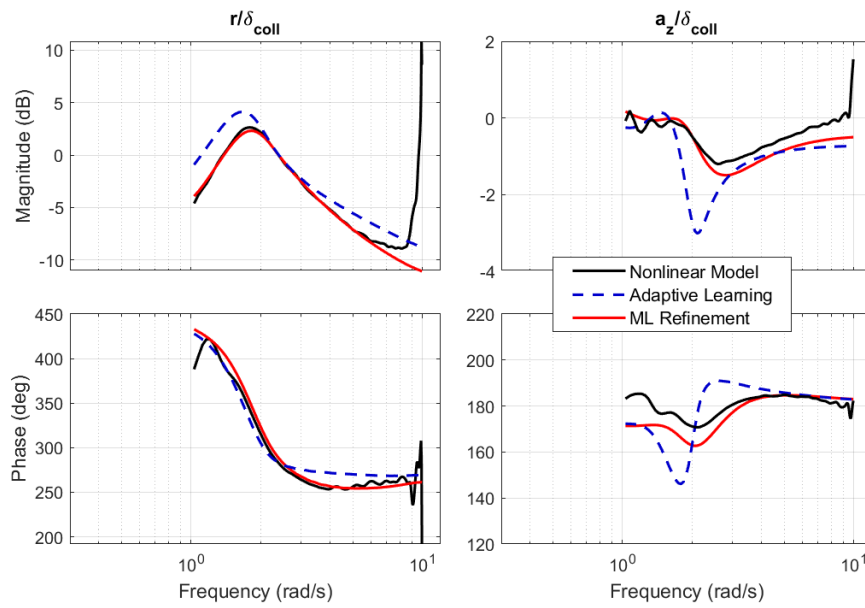


Figure 3.59: Frequency domain comparison of adaptive learning and maximum likelihood refinement with truth model in collective maneuver in 70 knots forward flight

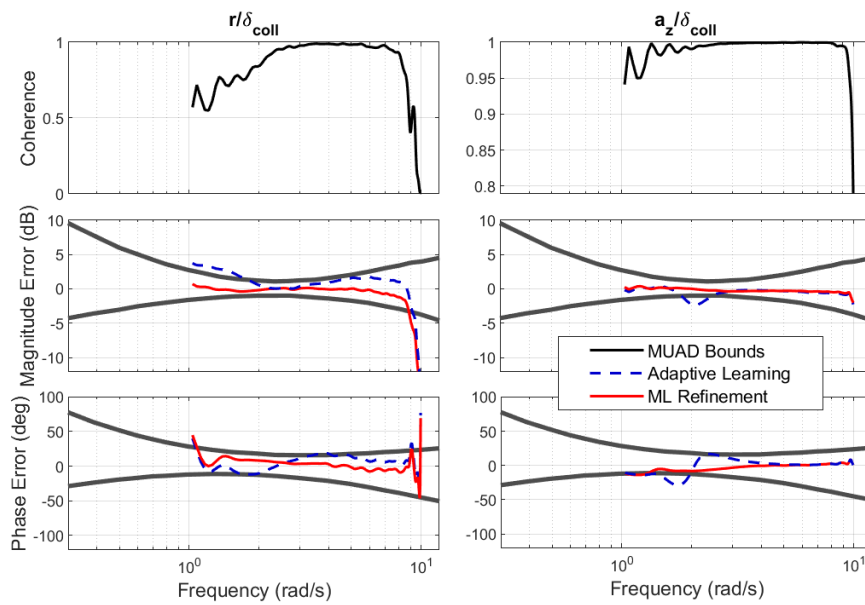


Figure 3.60: Coherence and errors of adaptive learning and maximum likelihood refinement with truth model in collective maneuver in 70 knots forward flight

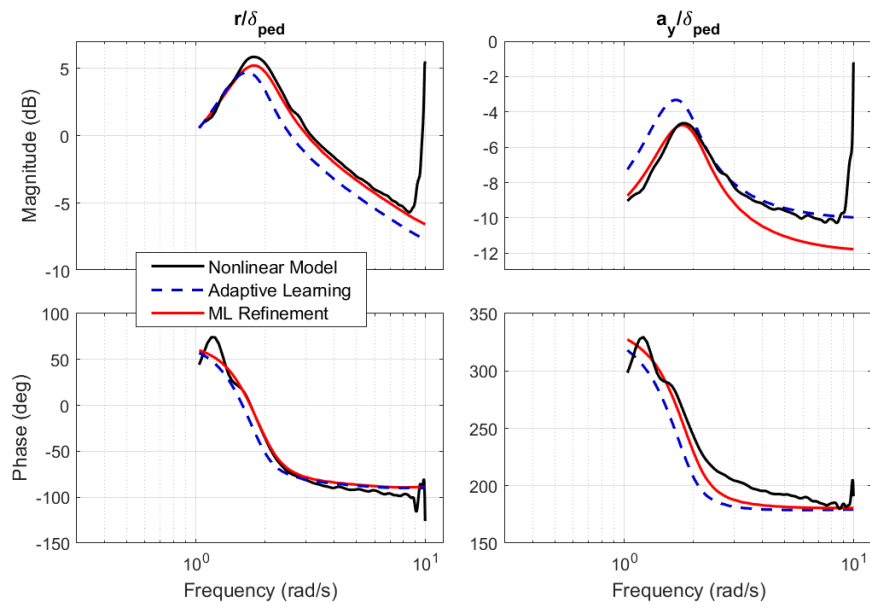


Figure 3.61: Frequency domain comparison of adaptive learning and maximum likelihood refinement with truth model in pedal maneuver in 70 knots forward flight

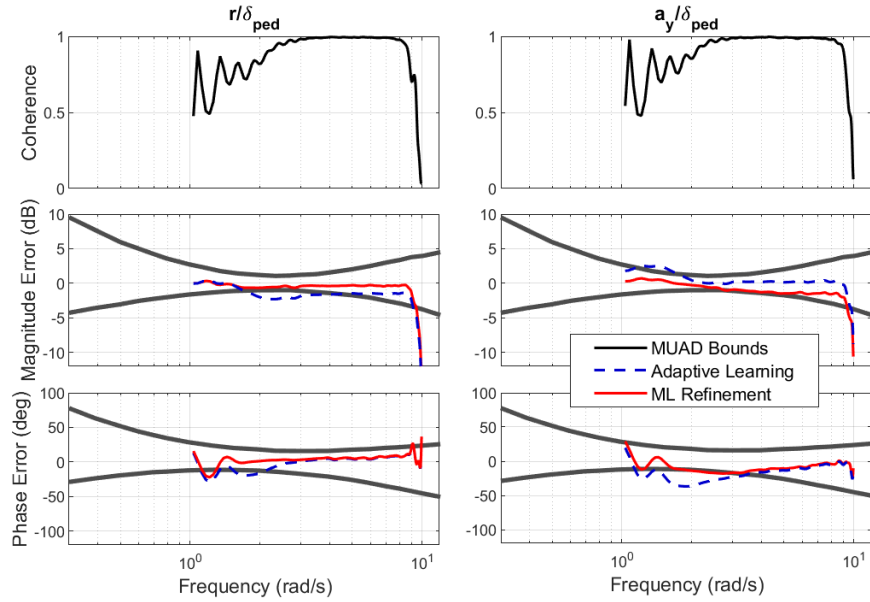


Figure 3.62: Coherence and errors of adaptive learning and maximum likelihood refinement with truth model in pedal maneuver in 70 knots forward flight

All in all, it can be said that the system identification software developed in this work is a powerful and versatile tool that can be used on its own, or in conjunction with another startup algorithm. When used alongside the adaptive learning algorithm, a more robust and faster overall procedure can be executed. The adaptive learning guarantees parameter convergence even with initial conditions away from their optimal values and provides unique optimal solutions. Since the algorithm is equation error based, the whole model reduction loop is often faster than the traditional Hessian based model reduction routine. Having a pre-determined model structure and decent initial parameter values, fast and accurate parameter convergence can be achieved with the developed software. If no prior algorithm is available, the developed software can be used on its own to execute a model reduction routine and carry out identification, as shown with the results.

CHAPTER 4

CONCLUSIONS AND FUTURE STUDIES

4.1 Conclusions

This work focuses on the development of a time domain system identification software to be used for rotorcraft identification. With the constructed software, the dynamics of H135 full scale helicopter in hover and 70 knots forward flight trim conditions are identified. To generate the adequate test data, a high fidelity nonlinear model of the helicopter is used as the truth model. The input signals are carefully constructed such that the distinct dynamics of the aircraft are excited at each flight condition. A state space mathematical model structure is adopted as the system to be identified. With the implementation of output error method with Levenberg-Marquardt algorithm, the identification loop is constructed. Using the Hessian base model reduction routine, the redundant derivatives in the initial model structure are determined, and dropped from the model structure. With the obtained minimal representation of the dynamic system, the system identification procedure is carried out. In the truth model data, additional rotor dynamics are present, such as flapping, inflow and engine dynamics. It is seen that the state space model structure is insufficient to reflect such dynamics. To account for such dynamics, state and control delays are employed. It is seen that the time domain outputs of the obtained mathematical models are adequate in terms of capturing the dynamics of the helicopter. To verify the obtained models in frequency domain, frequency sweep maneuvers are executed with the truth model and the identified models. The obtained time domain signals are converted to frequency domain via discrete Fourier transformation. To increase accuracy during this transformation, windowing of time domain signals is used. Magnitude and phase errors of the obtained frequency domain data are calculated and compared with MUAD

and AEE bounds. It is observed that the identified models also show sufficient accuracy in frequency domain, hence the identified models are acceptable. In this work, another study is carried out where initial model structure and the initial conditions for the model parameters are determined with a startup algorithm, adaptive learning. This algorithm guarantees convergence independent of the initial parameter guesses and provides unique optimal solutions. As it makes up for the shortcomings of the maximum likelihood output error method, it is the ideal startup algorithm. Similar to the first case, the time delays in the model structure are employed to account for the additional dynamics in the truth model signals. The obtained systems again show acceptable results in time and frequency domains. Therefore, the developed software for system identification can either be employed on its own to determine a minimal model structure, or used in conjunction with a startup algorithm to identify a dynamic system.

4.2 Future Studies

The system identification software developed in this work presents satisfactory results in both time and frequency domains. To further extend this study and increase its accuracy, some additions, and improvements can be made. Firstly, the time domain to frequency domain transformation requires long execution times. If the DFT algorithm is replaced with the efficient chirp-z transformation, the runtimes would be shortened. The accuracy of the frequency domain data highly depends on the transformation algorithm and the windowing method. In this work, the number of windows and window overlap is chosen via a trial and error process. However, the composite windowing approach presented in [44] proposes a systematic approach to select the optimal window size and amount. It introduces an additional computational burden, but increases the accuracy of frequency response estimates. Finally, the models obtained with system delays can be transformed to linear systems by making use of Padé approximations, if the desired final product is a linear system.

REFERENCES

- [1] Aerotim Engineering. <https://www.aerotim.com.tr>, [Accessed January 2023].
- [2] Airbus. H135. <https://www.airbus.com/en/products-services/helicopters/civil-helicopters/h135>, [Accessed January 2023].
- [3] K.-J. Åström and B. Torsten. Numerical identification of linear dynamic systems from normal operating records. *IFAC Proceedings Volumes*, 2(2):96–111, 1965.
- [4] J. S. Bendat and A. G. Piersol. *Random data: analysis and measurement procedures*. John Wiley & Sons, 2011.
- [5] R. P. Cheng, M. B. Tischler, and G. J. Schulein. R-max helicopter state-space model identification for hover and forward-flight. *Journal of the American Helicopter Society*, 51(2):202–210, 2006.
- [6] G. Chowdhary and E. Johnson. Concurrent learning for convergence in adaptive control without persistency of excitation. In *49th IEEE Conference on Decision and Control (CDC)*, pages 3674–3679. IEEE, 2010.
- [7] G. Chowdhary and E. Johnson. Concurrent learning for convergence in adaptive control without persistency of excitation. In *49th IEEE Conference on Decision and Control (CDC)*, pages 3674–3679. IEEE, 2010.
- [8] G. Chowdhary, T. Yucelen, M. Mühlegg, and E. N. Johnson. Concurrent learning adaptive control of linear systems with exponentially convergent bounds. *International Journal of Adaptive Control and Signal Processing*, 27(4):280–301, 2013.
- [9] L. S. Cicolani, A. H. McCoy, R. Sahai, P. H. Tyson, M. B. Tischler, A. Rosen, and G. E. Tucker. Flight test identification and simulation of a uh-60a helicopter and slung load. *Journal of the American Helicopter Society*, 46(2):140–160, 2001.

- [10] B. Etkin. *Dynamics of Atmospheric Flight*. Wiley, 1972.
- [11] G. Foster. The identification of aircraft stability and control parameters in turbulence. 1982.
- [12] J. Grauer, J. Conroy, J. Hubbard Jr, J. Humbert, and D. Pines. System identification of a miniature helicopter. *Journal of Aircraft*, 46(4):1260–1269, 2009.
- [13] G. Gursoy, O. H. Aslandogan, and I. Yavrucuk. Linear model identification for rotorcraft using adaptive learning. In *Proceedings of the 77th Annual Forum, Virtual*, May 2021. The Vertical Flight Society.
- [14] D. Halaas, S. Bieniawski, P. Pigg, and J. Vian. Control and management of an indoor, health enabled, heterogenous fleet. In *AIAA Infotech@ Aerospace Conference and AIAA Unmanned... Unlimited Conference*, page 2036, 2009.
- [15] P. G. Hamel and R. V. Jategaonkar. Evolution of flight vehicle system identification. *Journal of aircraft*, 33(1):9–28, 1996.
- [16] R. H. Hoh, D. G. Mitchell, I. L. Ashkenas, R. H. Klein, and R. K. Heffley. Proposed mil standard and handbook-flying qualities of air vehicles. volume 2. proposed mil handbook. Technical report, Systems Technology Inc Hawthorne CA, 1982.
- [17] K. W. Iliff and L. W. Taylor Jr. Determination of stability derivatives from flight data using a newton-raphson minimization technique. Technical report, 1972.
- [18] R. Jategaonkar. *Flight Vehicle System Identification: A Time-Domain Methodology, Second Edition*. 02 2015.
- [19] L. Kaufman and K. Peress. A review of methods for predicting helicopter longitudinal response. *Journal of the Aeronautical Sciences*, 23(3):259–271, 1956.
- [20] S. P. Khaligh, F. Fahimi, and C. Robert Koch. A system identification strategy for nonlinear model of small-scale unmanned helicopters. *Journal of the American Helicopter Society*, 61(4):1–13, 2016.
- [21] P. Li and I. Postlethwaite. Subspace and bootstrap-based techniques for helicopter model identification. *Journal of the American Helicopter Society*, 56(1):12002–12002, 2011.

- [22] R. E. Maine and K. W. Iliff. The theory and practice of estimating the accuracy of dynamic flight-determined coefficients. Technical report, 1981.
- [23] M. Marchand and F. Kh. Frequency domain parameter estimation of aeronautical systems without and with time delay. *IFAC Proceedings Volumes*, 18(5):669–674, 1985.
- [24] D. W. Marquardt. An algorithm for least-squares estimation of nonlinear parameters. *Journal of the society for Industrial and Applied Mathematics*, 11(2):431–441, 1963.
- [25] R. K. Mehra. Identification of stochastic linear dynamic systems using kalman filter representation. *AIAA Journal*, 9(1):28–31, 1971.
- [26] W. F. Milliken Jr. Progress in dynamic stability and control research. *Journal of the Aeronautical Sciences*, 14(9):493–519, 1947.
- [27] D. Mitchell, R. Hoh, C. He, and K. Strobe. Determination of maximum unnoticeable added dynamics. In *AIAA Atmospheric Flight Mechanics Conference and Exhibit*, page 6492, 2006.
- [28] E. A. Morelli and V. Klein. *Aircraft system identification: theory and practice*, volume 2. Sunflyte Enterprises Williamsburg, VA, 2016.
- [29] K. G. Murty and F.-T. Yu. *Linear complementarity, linear and nonlinear programming*, volume 3. Heldermann Berlin, 1988.
- [30] V. Myrand-Lapierre, M. B. Tischler, M. D. Pavel, M. Nadeau-Beaulieu, O. Stroosma, B. Gubbels, and M. White. Bell 412 modeling and model fidelity assessment for level-d training simulators. In *Vertical Flight Society's 76th Annual Forum and Technology Display*, 2020.
- [31] G. D. Padfield. *Helicopter flight dynamics: the theory and application of flying qualities and simulation modelling*. John Wiley & Sons, 2008.
- [32] G. D. Padfield and R. Du Val. Application areas for rotorcraft system identification: simulation model validation. *AGARD LS178*, pages 12–1, 1991.
- [33] K. M. Prabhu. *Window functions and their applications in signal processing*. Taylor & Francis, 2014.

- [34] R. Seamans Jr, B. Blasingame, and G. Clementson. The pulse method for the determination of aircraft dynamic performance. *Journal of the Aeronautical Sciences*, 17(1):22–38, 1950.
- [35] S. Seher-Weiss. Comparing different approaches for modeling the vertical motion of the ec 135. *CEAS Aeronautical Journal*, 6(3):395–406, 2015.
- [36] S. Seher-Weiss. Fitlabgui - a versatile tool for data analysis, system identification and helicopter handling qualities analysis. 09 2016.
- [37] S. Seher-Weiß. Act/fhs system identification including rotor and engine dynamics. *Journal of the American Helicopter Society*, 64(2):1–12, 2019.
- [38] S. Seher-Weiss and W. von Grünhagen. Comparing explicit and implicit modeling of rotor flapping dynamics for the ec 135. *CEAS Aeronautical Journal*, 5(3):319–332, 2014.
- [39] D. H. Shim, H. J. Kim, and S. Sastry. Control system design for rotorcraft-based unmanned aerial vehicles using time-domain system identification. In *Proceedings of the 2000. IEEE International Conference on Control Applications. Conference Proceedings (Cat. No. 00CH37162)*, pages 808–813. IEEE, 2000.
- [40] M. Shinbrot. *A least squares curve fitting method with applications to the calculation of stability coefficients from transient-response data*. Number 2341. National Advisory Committee for Aeronautics, 1951.
- [41] R. F. Stengel. *Flight dynamics*. Princeton university press, 2024.
- [42] Tech-Tool Plastics Inc. Ec135-1008-2: Clamshell window rh: Airbus helicopters. <https://www.tech-tool.com/product/clamshell-window-2>, [Accessed January 2023].
- [43] M. Tischler, J. Leung, and D. Dugan. Frequency-domain identification of xv-15 tilt-rotor aircraft dynamics. In *2nd Flight Testing Conference*, page 2695, 1983.
- [44] M. Tischler and R. Remple. *Aircraft And Rotorcraft System Identification: Engineering Methods With Flight-test Examples*. 08 2006.

- [45] M. B. Tischler. National Aeronautics and Space Administration, Ames Research Center, 1995.
- [46] M. B. Tischler, J. W. Fletcher, V. L. Diekmann, R. A. Williams, and R. W. Cason. Demonstration of frequency-sweep testing technique using a bell 214-st helicopter. Technical report, National Aeronautics and Space Administration Moffett Field CA AMES . . . , 1987.
- [47] M. B. Tischler, P. Scepanovic, A. Gubbels, et al. Bell 412 system identification and model fidelity assessment for hover and forward flight. *Journal of the American Helicopter Society*, 66(1):1–13, 2021.

Appendix A

ADDITIONAL IDENTIFICATION RESULTS

This section presents additional response plots of the identified systems. The 2311 and 3211 type input tests starting in the negative input direction are provided for rotorcraft identification with Hessian based model reduction approach.

A.1 Additional Results in Hover

A.1.1 Results for Longitudinal Cyclic Input

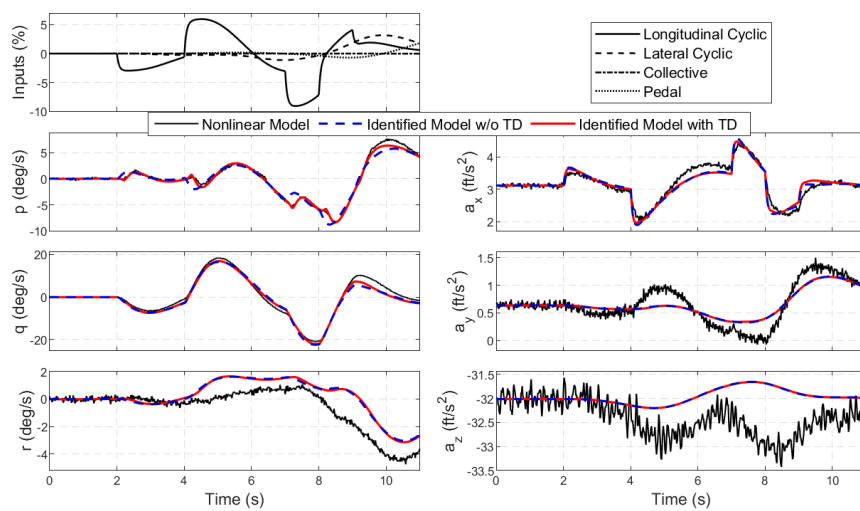


Figure A.1: Longitudinal cyclic 2311 input in negative direction during hover

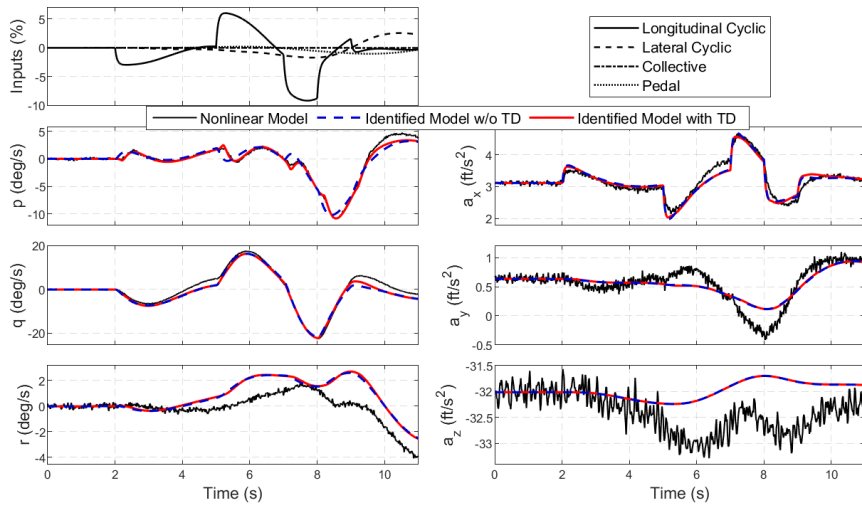


Figure A.2: Longitudinal cyclic 3211 input in negative direction during hover

A.1.2 Results for Lateral Cyclic Input

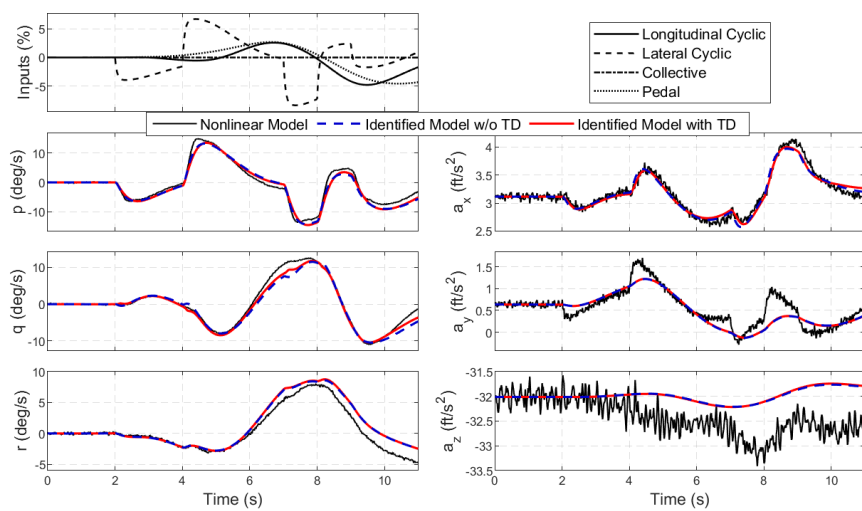


Figure A.3: Lateral cyclic 2311 input in negative direction during hover

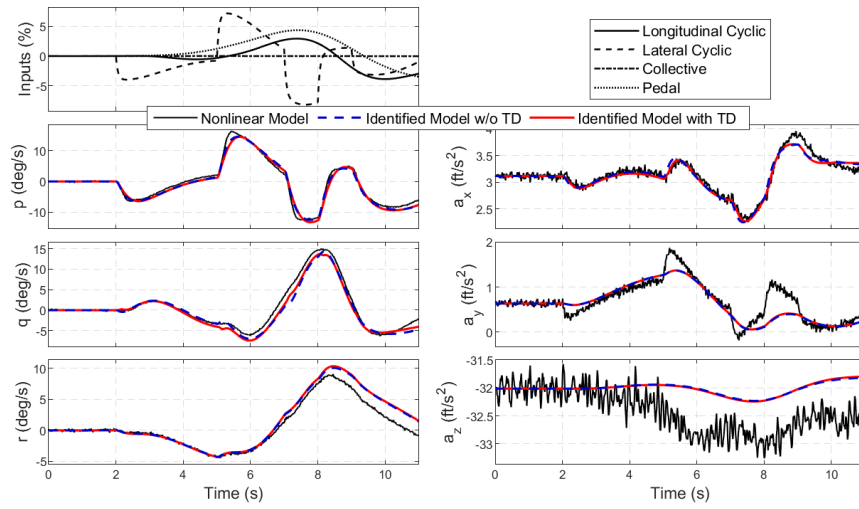


Figure A.4: Lateral cyclic 3211 input in negative direction during hover

A.1.3 Results for Collective Input

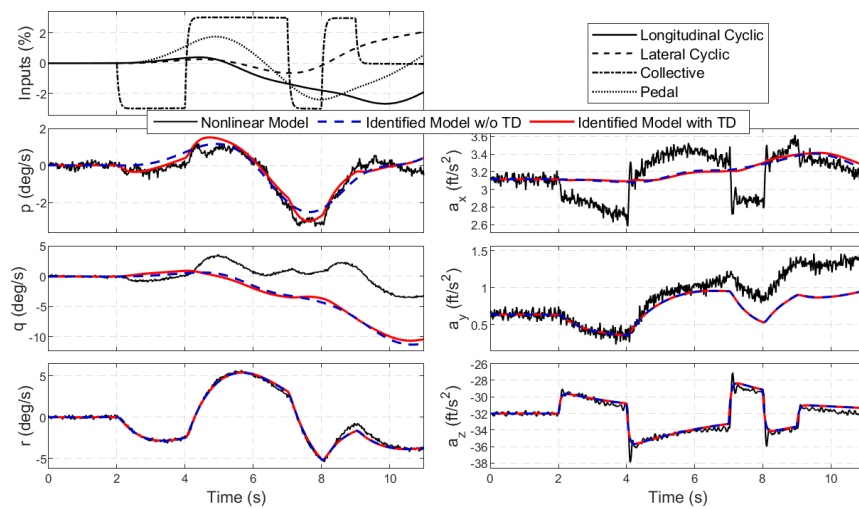


Figure A.5: Collective 2311 input in negative direction during hover

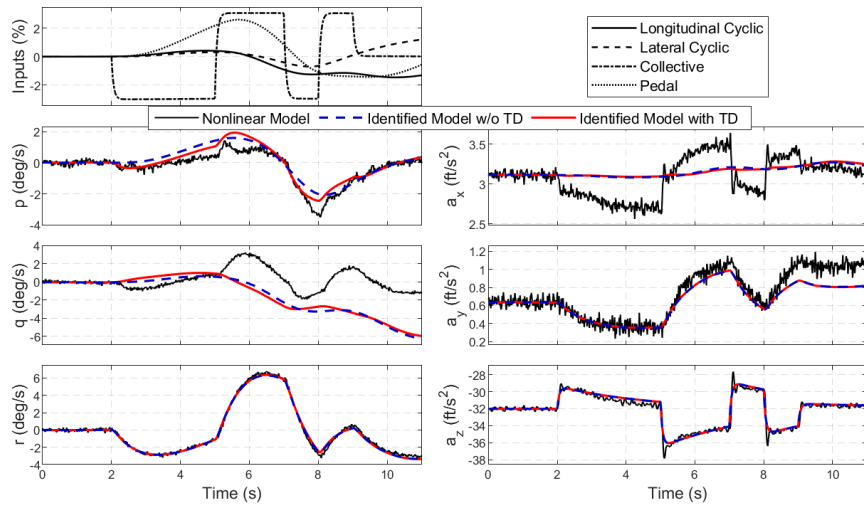


Figure A.6: Collective 3211 input in negative direction during hover

A.1.4 Results for Pedal Input

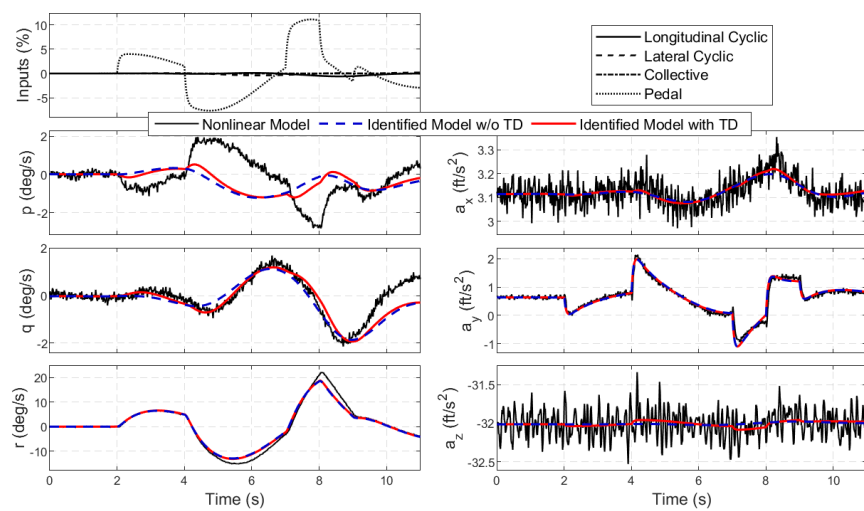


Figure A.7: Pedal 2311 input in negative direction during hover

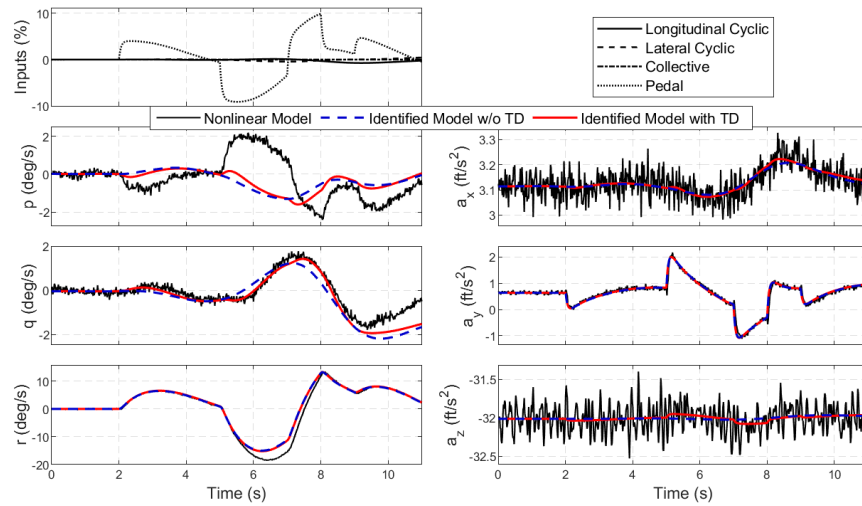


Figure A.8: Pedal 3211 input in negative direction during hover

A.2 Additional Results in Forward Flight

A.2.1 Results for Longitudinal Cyclic Input

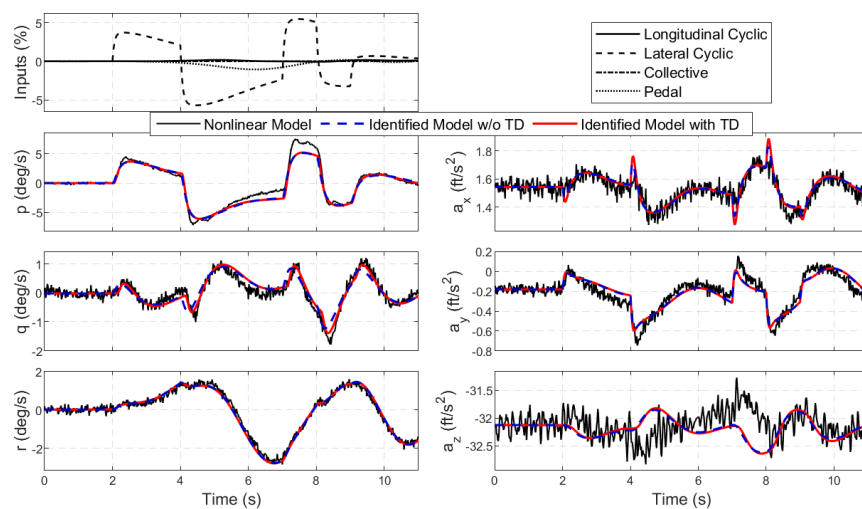


Figure A.9: Longitudinal cyclic 2311 input in negative direction during 70 knots forward flight

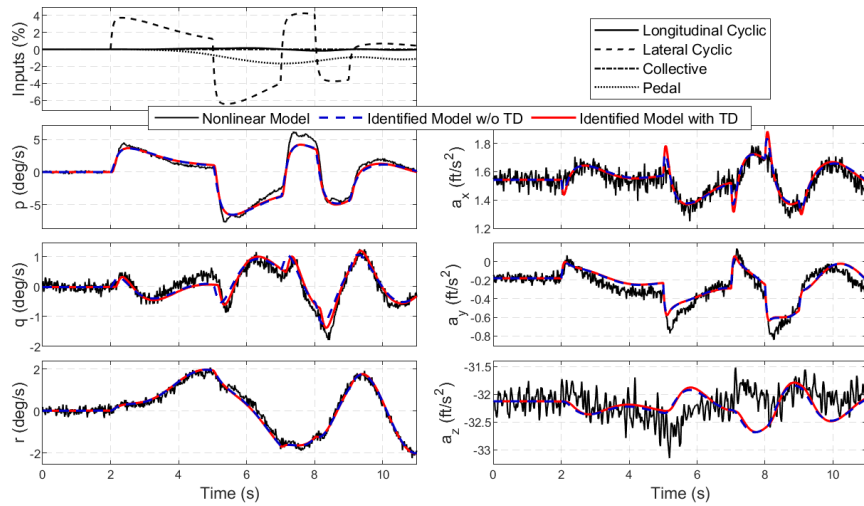


Figure A.10: Longitudinal cyclic 3211 input in negative direction during 70 knots forward flight

A.2.2 Results for Lateral Cyclic Input

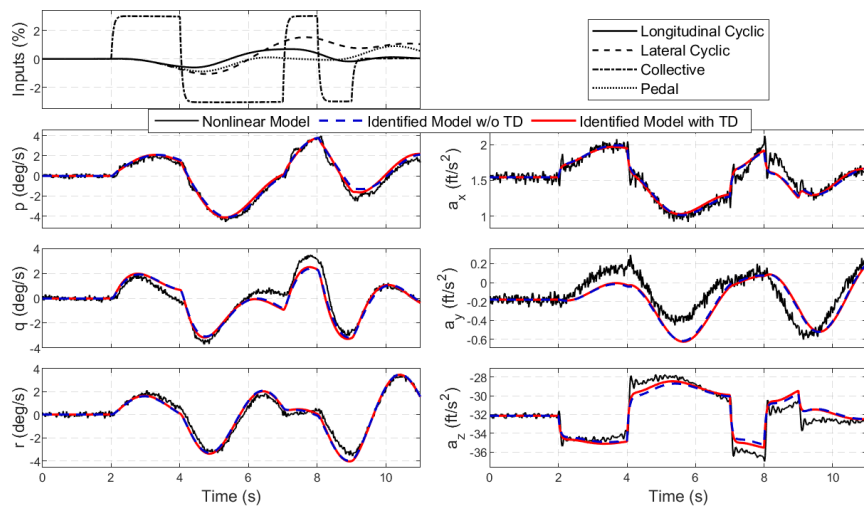


Figure A.11: Lateral cyclic 2311 input in negative direction during 70 knots forward flight

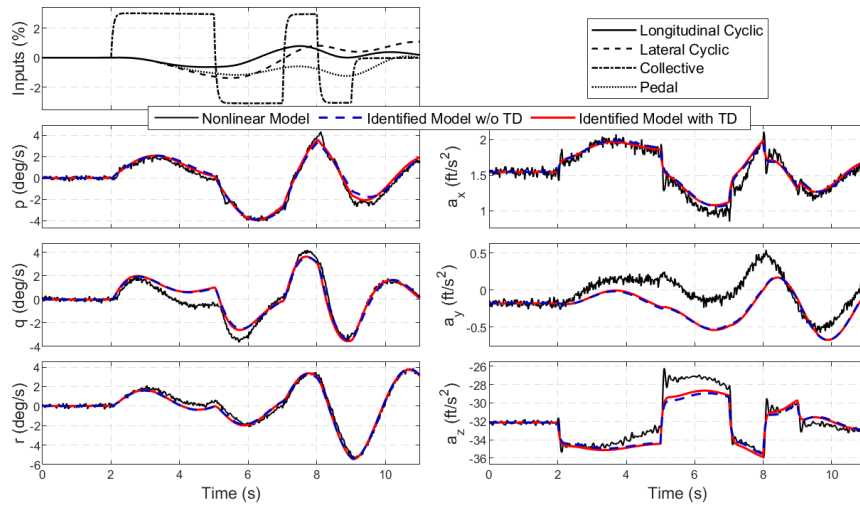


Figure A.12: Lateral cyclic 3211 input in negative direction during 70 knots forward flight

A.2.3 Results for Collective Input

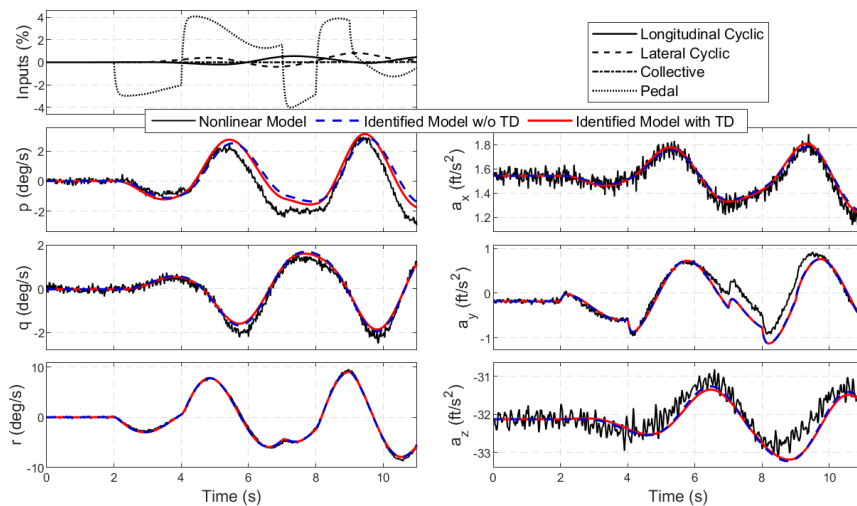


Figure A.13: Collective 2311 input in negative direction during 70 knots forward flight

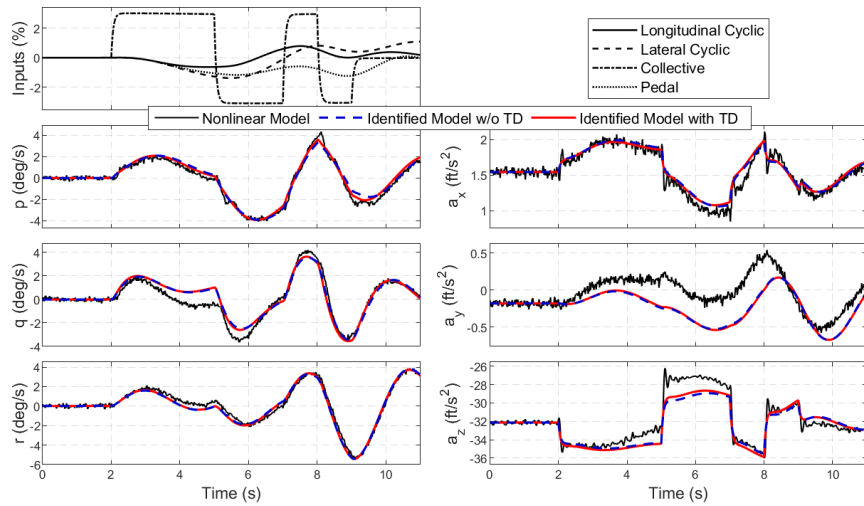


Figure A.14: Collective 3211 input in negative direction during 70 knots forward flight

A.2.4 Results for Pedal Input

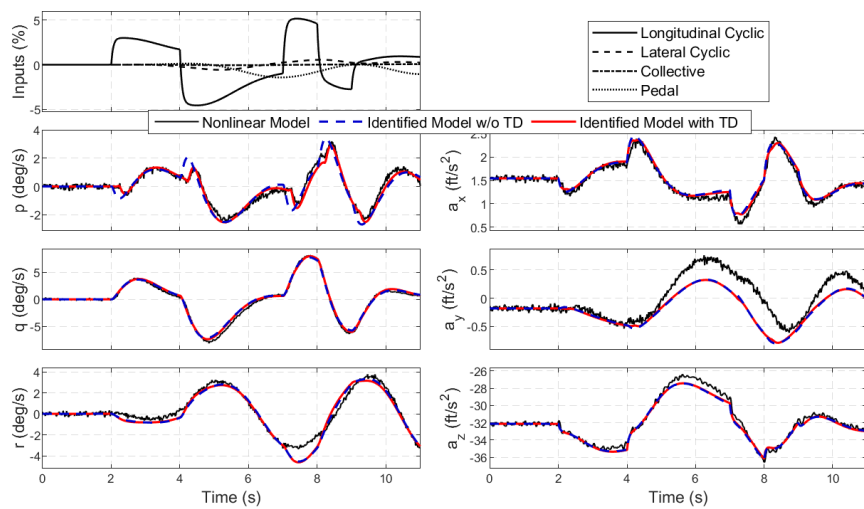


Figure A.15: Pedal 2311 input in negative direction during 70 knots forward flight

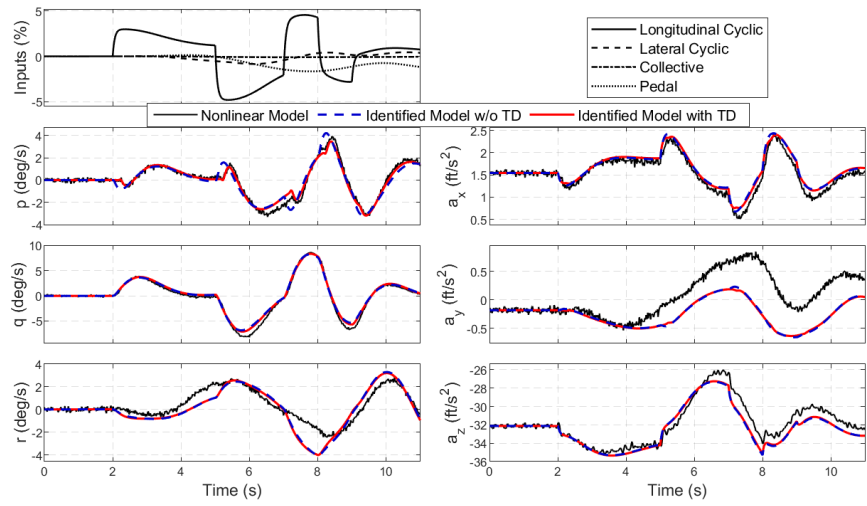


Figure A.16: Pedal 3211 input in negative direction during 70 knots forward flight

Appendix B

PARAMETERS REMOVED FROM THE MODEL STRUCTURE

The parameters removed from the model structure with Hessian based model reduction approach is presented in this section. The parameters are presented in the order that they are dropped in tables B.1 and B.2. Along with the converged values of the parameters, insensitivities and Cramer-Rao bounds are also provided.

B.1 Removed Parameters in Hover

Table B.1: List of parameters removed from the model structure in hover

Drop Order	Parameter	Value	\bar{I} (%)	\overline{CR} (%)
1	Y_{coll}	0.0028	42.5	56.8
2	Z_q	0.0055	17.8	39.7
3	Z_{lat}	0.0205	12.5	33.1
4	Z_p	-0.003	45.3	64.4
5	Z_v	-0.019	10.3	13.3
6	Z_{ped}	-0.0089	8.8	8.9
7	M_w	-0.19	9.4	30.4
8	X_v	-0.0066	4.2	9.5
9	Z_{long}	-0.0705	3.8	5.3
10	Y_u	0.0071	3.4	8.8
11	Y_w	-0.0262	3.4	6.6
12	X_{ped}	0.0073	2.6	4.5

Table B.1: List of parameters removed from the model structure in hover (Continued)

Drop Order	Parameter	Value	\bar{I} (%)	\overline{CR} (%)
13	Y_{long}	-0.0135	2.7	6.4
14	Z_u	0.0632	2.6	3.4
15	X_w	0.0270	3.7	4.7
16	Y_p	-0.0113	2.2	5.1
17	L_{coll}	0.6914	2.1	3.3
18	X_r	0.0066	1.7	2.2
19	X_{lat}	-0.0164	2.3	6.7
20	X_{coll}	0.0588	1.5	1.7
21	M_{ped}	-0.2133	1.5	3.3
22	Y_{lat}	0.0497	1.1	1.4
23	L_w	1.5964	1.0	2.4
24	M_{coll}	1.3749	2.0	2.2
25	Y_q	0.0195	0.8	1.0
26	M_v	1.0678	0.7	1.1
27	L_{ped}	-1.0731	0.9	1.3
28	N_{long}	-0.8022	0.7	2.5
29	N_u	0.1130	1.9	8.6

B.2 Removed Parameters in Forward Flight

Table B.2: List of parameters removed from the model structure in forward flight

Drop Order	Parameter	Value	\bar{I} (%)	\overline{CR} (%)
1	X_{ped}	-0.0001	35.6	51.5
2	Z_q	0.0087	26.4	51.4
3	X_r	0.0009	21.9	27.7
4	Z_{ped}	-0.0086	21.4	24.1
5	Y_{coll}	-0.0100	16.6	20.6
6	L_{ped}	0.1731	10.9	20.1
7	Y_r	0.0069	7.1	9.5
8	N_u	0.0350	16.3	88.1
9	X_v	-0.0014	11.5	26.3
10	Y_w	-0.0078	7.7	14.6
11	X_q	0.0088	4.5	8.8
12	Z_p	0.0352	3.9	16.2
13	M_{ped}	0.1083	3.4	4.3
14	Y_u	0.0295	3.1	3.9
15	Y_{long}	-0.0563	2.5	3.8
16	Z_{lat}	0.0730	2.1	2.4
17	Y_q	0.0522	1.8	1.9
18	M_v	-0.0637	2.4	9.1
19	Z_v	-0.0412	2.0	3.0
20	M_u	0.0075	2.5	3.7

Appendix C

IDENTIFIED PARAMETERS

The parameters identified with the model structure with Hessian based model reduction approach is presented in this section. The converged values of the parameters, insensitivities and Cramer-Rao bounds are provided.

C.1 Identified Parameters in Hover

Table C.1: List of parameters identified in hover

Parameter	Value	\bar{I} (%)	\overline{CR} (%)
X_u	-0.0220	1.4	3.0
X_p	0.0421	0.5	0.8
X_q	0.0495	0.4	0.9
X_{long}	-0.2114	0.3	0.5
Y_v	-0.1490	0.5	0.6
Y_r	0.0745	0.4	0.7
Y_{ped}	-0.1853	0.3	0.4
Z_w	-0.3682	1.7	1.8
Z_r	0.0101	2.1	4.8
Z_{coll}	-0.8611	0.5	0.5
L_u	0.9112	0.6	2.2
L_v	-2.4459	0.4	1.3
L_p	-3.2899	0.2	1.3

Table C.1: List of parameters identified in hover (Continued)

Parameter	Value	\bar{I} (%)	\overline{CR} (%)
L_q	2.3966	0.1	1.0
L_r	0.0793	2.5	5.0
L_{long}	-5.8977	0.1	1.0
L_{lat}	6.6955	0.2	1.1
M_u	1.0962	0.4	1.5
M_p	-2.7426	0.2	1.0
M_q	-1.8474	0.2	1.0
M_r	-0.2466	0.6	1.5
M_{long}	5.4743	0.1	0.7
M_{lat}	2.9367	0.4	1.7
N_v	1.4273	0.3	0.8
N_w	-0.0826	2.2	3.8
N_p	-0.3797	1.2	3.1
N_q	0.1123	1.7	3.6
N_r	-1.6714	0.2	0.4
N_{lat}	0.8692	0.9	2.5
N_{coll}	1.9964	0.2	0.4
N_{ped}	3.6093	0.2	0.5
$\tau_{L_{long}}$	0.1833	0.4	0.8
$\tau_{L_{lat}}$	0	-	-
$\tau_{M_{long}}$	0	-	-
$\tau_{M_{lat}}$	0.1167	1.7	2.8

C.2 Identified Parameters in Forward Flight

Table C.2: List of parameters identified in forward flight

Parameter	Value	\bar{I} (%)	$\overline{\text{CR}}$ (%)
X_u	-0.0477	1.1	1.7
X_w	0.0696	0.5	0.7
X_p	0.0614	0.5	1.2
X_{long}	-0.0817	0.7	1.2
X_{lat}	-0.0438	0.7	1.7
X_{coll}	0.0563	1.3	1.7
Y_v	-0.0958	0.5	0.6
Y_p	-0.0310	1.5	4.2
Y_{lat}	0.0636	0.7	2.0
Y_{ped}	-0.0579	1.8	2.1
Z_u	0.1002	3.2	4.8
Z_w	-0.4676	0.5	0.6
Z_r	0.0097	2.5	5.9
Z_{long}	-0.3474	1.0	1.3
Z_{coll}	-0.9002	0.7	0.8
L_u	-1.4341	1.7	7.3
L_v	-2.1558	0.3	6.9
L_w	3.0146	0.4	7.3
L_p	-8.7456	0.1	6.7
L_q	3.6001	0.3	6.6
L_r	0.3845	2.0	4.9
L_{long}	-4.2317	0.4	7.7
L_{lat}	8.1947	0.1	6.6
L_{coll}	1.8070	1.5	7.2

Table C.2: List of parameters identified in forward flight (Continued)

Parameter	Value	\bar{I} (%)	\overline{CR} (%)
M_w	-1.0157	0.3	5.2
M_p	-1.4082	0.2	7.0
M_q	-1.8389	0.2	5.1
M_r	0.0258	2.2	3.7
M_{long}	3.4339	0.2	5.3
M_{lat}	1.1811	0.2	7.3
M_{coll}	2.0220	0.4	5.6
N_v	1.2672	0.1	0.2
N_w	-0.1644	1.3	2.9
N_p	-0.4528	0.3	2.3
N_q	0.5770	0.4	1.4
N_r	-0.4201	0.2	0.6
N_{long}	-1.0436	0.4	1.2
N_{lat}	0.5044	0.2	1.9
N_{coll}	0.8713	0.5	1.0
N_{ped}	2.0433	0.1	0.2
τ_{L_p}	0.0500	1.0	9.8
τ_{L_q}	0.1108	1.3	8.1
$\tau_{L_{long}}$	0.2015	0.7	2.0
$\tau_{L_{lat}}$	0.0341	1.9	10.5
τ_{M_p}	0.1345	0.6	2.9
τ_{M_q}	0.0286	3.1	12.4
$\tau_{M_{long}}$	0	-	-
$\tau_{M_{lat}}$	0.1426	0.8	2.3